Magneto–optical investigations of EuS/Co and EuS/Ni multilayers for spintronic applications

Im Fachbereich Physik der Freien Universität Berlin
eingereichte Dissertation

von

Alexander Goschew

2017

Erstgutachter:	Prof. Dr. Paul Fumagalli
Zweitgutachter:	Prof. Dr. Wolfgang Kuch
Tag der Disputation:	02.06.2017

Contents

List of Figures

List of Acronyms

AES	Auger Electron Spectroscopy
AFM	Atomic Force Microscopy
EL	Electroluminescence
FWHM	Full Width Half Maximum
fcc	face centered cubic
hcp	hexagonally close packed
LED	Light Emitting Diode
MBE	Molecular Beam Epitaxy
MOKE	Magneto–Optical Kerr Effect
pMOKE	polar Magneto–Optical Kerr Effect
PMA	Perpendicular Magnetic Anisotropy
RT	Room Temperature
SPA–LEED	Spot Profile Analysis Low Energy Electron Diffraction
STM	Scanning Tunneling Microscopy
SQUID	Superconducting Quantum Interference Device
TEM	Transmission Electron Microscopy
HTEM	High Resolution Transmission Electron Microscopy
XAS	X–Ray Absorption
XMCD	X–Ray Magnetic Circular Dichroism
XRMS	X–Ray Magnetic Scattering
XRR	X–Ray–Reflectivity

Chapter 1

Introduction

Modern day technology highly relies on the electronic properties of semiconductors. Since the first development of computer chips and efficient switching devices like transistors, much progress has been made to make them more efficient, faster and smaller. Moore has predicted an increase of transistors per computer chip over time [1]. For many years, this prediction has held but now a time has been reached where physical limitations start to interfere with this prediction.
New ways to increase computer speed and data processing have to be developed. One field that has been emerging since the 1990's is spintronics. The name itself is made up of two parts: the 'spin' meaning the spin quantum number of charge carriers and electronincs ('tronics'). An overview on the topic is given by Wolf et al. [2], Zutic et al. [3] and Felser et al. [4].
It is believed that spintronics can offer new ways for further technological advancement. A spintronic device would not only use the electronic charge but also the spin, i.e. for data processing in computers. For a working spintronic device spin–polarised currents will need to be injected, detected and processed efficiently. An overview on the concepts behind spin–injection into semiconductors is given by Schmidt [5, 6], Oestreich [7] and Awschalom [8].
Furthermore, modern day computers rely on the magnetic properties of random access memories. Through spintronics one hopes to combine the properties of semiconductors with those of magnetic materials, i.e. ferromagnets for data storage.

Different materials have been proposed as future spintronics materials, among them diluted magnetic semiconductors, half-metallic ferromagnets and ferromagnetic semiconductors. However, until now none of these materials have succesfully fulfilled all of the necessary requirements for an operation of such devices such as generating spin–polarised currents at Room Temperature (RT).
Diluted magnetic semiconductors are doped with ferromagnetic impurities, e.g. Co or Mn,

which leads to a magnetisation of the material. However, measurements show that most of these materials only exhibit paramagnetic behaviour at RT so far which rules them out.

Half metallic ferromagnets were defined as a material class by de Groot et al. [9]. The density of states for minority and majority spin–configurations in such materials is different at the Fermi level. One spin direction (i.e. spin–down) has a high density of states while for the other it is zero. The material can be treated as having a band gap for the second spin direction, hence the term half-metallic. In such a material, all of the electrons which contribute to charge are completely spin–polarised. However, when connected to metals the spin injection efficiency of half–metallic ferromagnets is low and further attempts to increase the efficiency need to be undertaken.

Another interesting set of materials are the ferromagnetic semiconductors which have an inherent ferromagnetism below their Curie temperature. These materials seem like perfect devices for spintronics. Being semiconductors and showing ferromagnetism would lead to intrinsic exchange–splitting in the conduction band and would allow for the creation of spin–polarised currents within the semiconductors themselves. Using ferromagnetic semiconductors as spin–injectors in spintronic devices could largely eliminate the problem of impedance mismatch, which limits the spin injection efficiency in devices with a direct ferromagnet–semiconductor interface, e.g. Fe/GaAs or Fe/Si.

Europium oxide (EuO) and europium sulfide (EuS), part of the EuX chalcogenides (X = O, S, Te, Se), are two examples of ferromagnetic semiconductors. Ferromagnetism was first discovered in EuO and EuS in the early 1960's [10, 11, 12]. Their ferromagnetism is due to their highly localized, half–filled *4f* shells. The high localization of their spins makes the two compounds examples of ideal Heisenberg ferromagnets. The parallel alignment of the electron spins in the *4f* shell gives the materials a high theoretical value of 7 μ_B, while experimentally, 6.9 μ_B have been observed. In their ferromagnetic state, both materials have a large exchange–splitting in the conduction band (0.34 eV for EuS and 0.6 eV for EuO), which makes them very good materials for spin–filtering in spintronic devices. The tunnelling probability would be different for spins having a parallel or antiparallel alignment regarding the direction of magnetisation in EuS or EuO, lowering the tunnelling barrier for parallel alignment and increasing it for antiparallel alignment. Because the energy barrier enters exponentially in the tunnelling probability, electron spin polarisations of over 80% have been observed experimentally [13, 14]. Even at RT, these large exchange splittings are larger by one order of magnitude than the thermal energy ($E = k_B T = 26\ meV$).

The drawback of both materials is found in their very small Curie temperature of only a

16.5 K (EuS) and 69 K (EuO) [15]. The EuX chalcogenides were investigated thoroughly in theoretical and experimental approaches from the 1960's. Overviews on the findings are given by Wachter [15, 16, 17], Schoenes [18, 19] as well as Mauger and Godart [20]. For real–life applications, the ordering temperature of both materials is too low, so it has to be increased significantly in order to make these materials feasible.

Experiments have shown an increase of the EuS Curie temperature in EuS/Fe layers [21] and EuS/Co multilayers [22, 23, 24, 25]. The increase of T_C has been found to be larger in EuS/Co multilayers.
For possible future applications of EuS in spintronic devices, the growth characteristics of EuS are also of interest. Different substrates, such as Si(111), Si(001), MgO, BaF_2 or PbS, have been used over the years in the attempt to grow EuS epitaxially, with varying results.

The main focus of this thesis will be EuS. The material will be investigated in EuS/Co and EuS/Ni multilayers and its growth studied on the two new, previously unused, substrates InP(001) and InAs(001). The thesis is structured in the following manner:

Chapter 2 will introduce and discuss the main materials used and the theoretical background of the experimental methods necessary for this thesis. The material EuS and its magnetic and magneto–optical properties will be discussed in detail.

Chapter 3 will describe the two growth chambers that were used to produce all samples and discuss the polar Magneto–Optical Kerr Effect (pMOKE) setup.

Chapter 4 will discuss the results of EuS/Co and EuS/Ni multilayers. Their growth will be discussed and compared to each other. Element specific X–Ray Magnetic Circular Dichroism (XMCD) measurements of Eu^{2+} at 5 K and RT will be presented. Polar MOKE measurements of EuS/Co multilayers at RT will show that it is possible to disentangle the EuS and Co contributions.

Chapter 5 will deal with the integration of EuS/Co layers on a spin–Light Emitting Diode (LED). The working principle of a spin–LED, the experimental setup for Electroluminescence (EL) measurements and the results of EuS/Ni and EuS/Co layers on spin–LEDs with and without a AlO_x tunnel barrier will be shown and discussed.

The growth of EuS on the two substrates InP(001) and InAs(001) will be discussed in Chapter 6. The growth quality is investigated by Auger Electron Spectroscopy (AES), Spot Profile Analysis Low Energy Electron Diffraction (SPA–LEED), Atomic Force Mi-

croscopy (AFM) and Transmission Electron Microscopy (TEM).

Chapter 7 will summarize the results of the thesis and give an outlook of possible future measurements.

Chapter 2

Materials and Methods

This chapter will focus on the important materials for this thesis and give a theoretical overview of the experimental methods. First the material, with a large focus on EuS, will be discussed, followed by the experimental methods.

2.1 Materials

2.1.1 Europium Sulfide

Physical properties

A lot of interest and research has been devoted to the rare earth chalcogenides ever since EuO was found to be a ferromagnetic semiconductor in 1961 [10]. In view of applications and storage or processing devices, the discovery of ferromagnetic semiconductors motivated researchers to perform further investigations. Of the compounds in the chalcogenide series EuO and EuS are ferromagnetic below their Curie temperature, EuTe is antiferromagnetic and EuSe is metamagnetic, exhibiting both phases [18].
The atomic number of Eu is 63 and it is part of the lanthanides. Its groundstate corresponds to [Xe]$4f^7 6s^2$. When Eu enters the bonding with S, the two Eu $6s$ electrons take part in the bonding and Eu is left with a half–filled $4f$ shell with a total spin of $7/2$. EuS has a T_C of 16.5 K [16]. The remaining $4f$ electrons are highly localized and bound close to the core and effectively screened by the $5s$ and $5p$. This is exemplary shown for the Gd orbitals in figure 2.1. The Gd electron configuration is [Xe]$4f^7 5d^1 6s^2$, and thus only differs by one $5d$ electron compared to EuS, i.e. Gd^+ and EuS are isoelectronic.
It is due to this localization and screening of the $4f$ electrons that they do not take part in the bonding and thus their magnetic moment is unchanged. The spectroscopic groundstate of the rare earth chalcogenides is ${}^8S_{7/2}$ and they crystallize in the simple NaCl–like face centered cubic (fcc) structure (figure 2.2) with increasing lattice constants from EuO to EuTe. EuS has a lattice constant of $a = 5.968$ $\mathring{A}$.

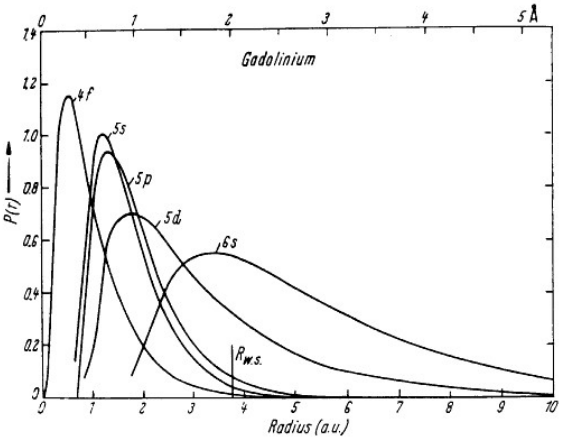

Figure 2.1: Radial distribution of the atomic orbitals shown for neutral Gd ($[Xe]4f^7 5d^1 6s^2$). From[15].

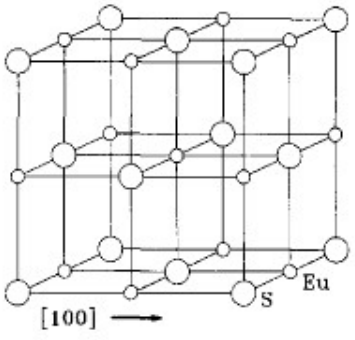

Figure 2.2: EuS lattice structure. From [21].

Band structure

In order to understand the mechanisms behind the magnetic behaviour of the rare earth chalcogenides in general and EuS in particular, one has to look at their bandstructure. The band structures known today are deducted from the theoretical computations and the spectroscopic experimental results from absorption measurements or Faraday rotations [26]. A direct measurement of the bandstructure can only be obtained on single crystals or epitaxially grown thin films by photoemission spectroscopy. Nevertheless, the work that has been done so far in this field gives a good idea of what the bandstructure of EuS might look like.

Photoemission studies of Eastman et al. [27] from 1969 performed on polycrystalline films of EuS, EuO, EuSe and GdS showed evidence that the *4f* localized band is located between the valence p band and conduction d bands. However, modern day techniques have much improved and a clearer picture of the bandstructure could be obtained by photoemission spectroscopy today.

Based on the work of Eastman et al., Güntherodt et al. [26] derived an energy level scheme for EuS which is shown in figure 2.3.

From this energy scheme the following facts can be gathered: the $4f$ electrons are situated between the $3p$ valence band, coming from the S^{2-} and the $5d$ conduction band from Eu^{2+}. The conduction band is further split into a $5d_{t_{2g}}$ bonding and a $5d_{e_g}$ anti–bonding level by the crystal field [15]. The crystal field splitting amounts to 2.1 eV [16].

The energies shown for those transitions are assumed to be between the maxima of the densities of state between initial and final level. For instance, the first assigned transition $4f$ to $5d_{t_{2g}}$ at 2.33 eV is observed at 300 K as a maximum in the absorption spectrum (figure 2.4), whereas the bandgap of EuS is $E_g = 1.65\ eV$.

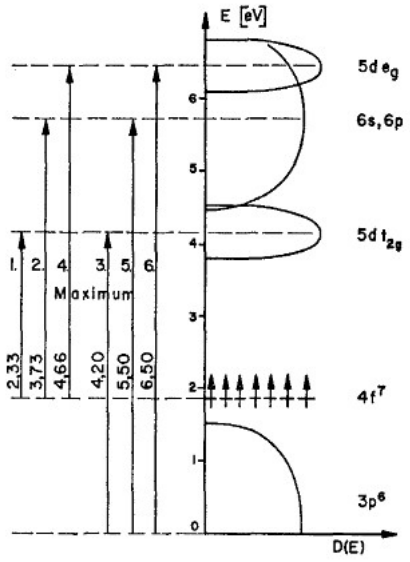

Figure 2.3: Energy level scheme of EuS at 300 K. The $4f$ electron band is shown as highly localized. The density of states is shown extending to the right. Transition energies assigned to the given optical transitions are shown to the left. The arbitrarily placed 0 on the energy scale is in the middle of the p valence band. From [26].

The $5d$ band is exchange–split (not shown in this figure) due to spin–spin–interactions. The exchange split energy is $\Delta = 0.34\ eV$. For a more detailed structure of the $5d$ energy–splittings see Wachter [15]. Wachter additionally includes the following energy distortions:

1. spin–orbit coupling in the ^7F_J configuration of Eu^{2+}–ions,
2. spin–orbit coupling in the $5d$–states,
3. exchange splittings of the $5d$–states,
4. magnetisation of the crystal.

As seen from figure 2.3 at RT a maximum transition between $4f$ and $5d_{t_{2g}}$ is observed at 2.33 eV. However, a red–shift of the absorption maxima is observed for lower temperatures, first observed by Busch and Wachter [28]. A red–shift of the absorption edge is also observed. Figure 2.4 shows the red–shift of the absorption maximum for different temperatures.

Schoenes [18], using a coupling scheme proposed by Kasuya [29] and data obtained from Faraday rotation measurements, assigns the maxima observed for different temperatures to different transition that are allowed. For the excitation of one $4f$ electron the spin–up band (parallel spin, $S_T = 7/2$) of $5d_{t_{2g}}$ is lower than the antiparallel spin–band ($S_T = 5/2$). He argues that in the paramagnetic phase, spin–orbit coupling can lead to a mixing of higher J–values of the parallel spin–band and the lower J–values of the antiparallel spin–band so spin–flip transitions are not strictly forbidden (see figure 2.5).

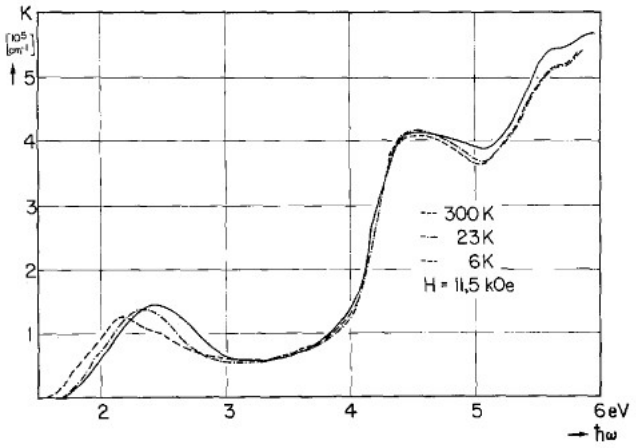

Figure 2.4: Absorption spectra of EuS at different temperatures. From [18].

For lower temperatures the spin–orientation of the $4f$ electrons becomes more and more aligned and hence, non–spin–flip transitions are favoured. Schoenes assigns the maximum absorption peak of 2.33 eV at RT to the spin–flip–transition.

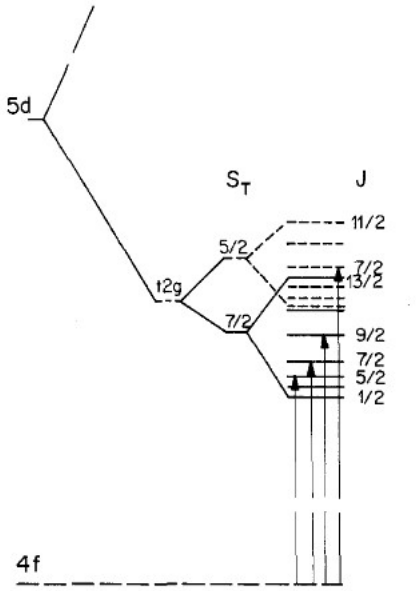

Figure 2.5: Coupling scheme of the ${}^7F_J(4f^6)5d$ configuration proposed by Kasuya. Indicated are allowed transitions into the spin–flip final state ($\Delta J = 0$) and the non–spin–flip final state ($\Delta J = 0, \pm 1$). From [18].

Magnetic exchange

Though the EuX chalcogenides have been studied since the 1960's, it has been difficult to explain exactly the mechanisms that lead to the ferromagnetic behaviour of EuO and EuS on the one hand and the antiferromagnetic and metamagnetic behaviour of EuTe and EuSe on the other hand. Different explanations for the exchange effects have been given by a range of scientists. A brief outline of the governing exchange mechanisms will be given here.

Due to the localization of the $4f$ electrons and their screening, a direct interaction between the electrons in form of overlapping $4f$ wavefunctions between neighbouring Eu^{2+}–ions that could lead to ferromagnetic behaviour can be excluded [16, 18]. Hence, an indirect exchange mechanism is thought to be present. As the Eu chalcogenides are considered ideal Heisenberg ferromagnets, the isotropic exchange Hamiltonian H can be written as [16]:

$$H = -\sum_{i,j} J_{ij} S_i S_j = -\sum_{nn} \bar{J}_1 S_0 S_{nn} - \sum_{nnn} \bar{J}_2 S_0 S_{nnn} \tag{2.1}$$

where (nn) and (nnn) denote the nearest neighbour and next nearest neighbour of the spins respectively. $\bar{J}_1$ and $\bar{J}_2$ are the effective ferro– and antiferromagnetic exchange integrals, made up of summing over all the individual contributions in the (nn) and (nnn) directions.
Goodenough, Wachter and Schoenes assign the ferromagnetic exchange $\bar{J}_1$ to a Eu–Eu (or cation–cation) superexchange that is mediated through a virtually excited $4f$ electron of one Eu^{2+}–ion to the $5d_{t_{2g}}$ subband of a neighbouring cation [16, 30]. The $5d$ electron can then be polarised by the $4f$ electrons and can then couple ferromagnetically to other $4f$ electrons on neighbouring sites via an indirect Ruderman–Kittel–Kasuya–Yosida (RKKY) interaction, known in metals.
On the other hand, Kasuya explains the ferromagnetism in EuS by the magnetic exciton [29]. Here, a $4f$ electron is excited to the energetically higher $5d_{e_g}$ band of the same ion and couples to the neighbouring $4f$ electrons from there.
Another model is given by Lee and Liu, who assign the ferromagnetic exchange to a virtual p–d transition of a valence band electron originating from the anion in the compound [31, 32]. Conversely, Wachter and Goodenough claim that the anion plays no part in the ferromagnetic exchange.

All views are, however, in agreement as to the indirect RKKY interaction being responsible for the exchange. The nature of the RKKY interaction strongly depends on the

distance between the coupled magnetic moments and sign reversals (ferromagnetic $->$ antiferromagnetic) occur.
For the ferromagnetic exchange $\bar{J}_1$ the model proposed by Wachter will be used. Third order perturbation calculations render for the energy [16]:

$$\bar{J}_1 = \frac{t^2 J_{fd}}{2S^2 U^2_{f-d_{t_{2g}}}} \tag{2.2}$$

where $J_{fd} \approx 0.1\ eV$ is the intra–atomic exchange constant $t \approx 0.15\ eV$ the transfer integral, S the total spin and $U_{f-d^2_{t_{2g}}} \approx 2.2\ eV$ (center of the t_{2g} band) the energy difference.

For the antiferromagnetic exchange $\bar{J}_2$ different mechanisms apply. Here, the p valence band electrons play an important role. Kasuya estimates that the usual Kramers–Anderson superexchange (antiferromagnetic) is too small to account for the values of $\bar{J}_2$, however, it is still present. Kasuya, Lee and Liu explain the antiferromagnetic exchange with a virtual transition to the $5d$ band and subsequent antiferromagnetic coupling to the (nnn) Eu sites [32]. Wachter gives the following formula for $\bar{J}_2$:

$$\bar{J}_2 = -\frac{1}{2}\frac{|\beta|^4 \, |J_{fd}|^2}{U_{p-d_{e_g}}} \tag{2.3}$$

where $|\beta|^2 \approx 0.1eV$ is a parameter and $U_{p-d_{e_g}}$ the energy separation between p and $5d_{e_g}$ band. Wachter calculates the following values for $\bar{J}_1$ and $\bar{J}_2$ for EuS [16]:

$$\bar{J}_1 = 0.228\ K \tag{2.4}$$

$$\bar{J}_2 = -0.102\ K \tag{2.5}$$

$$\bar{J}_1 + \bar{J}_2 = 0.126\ K \tag{2.6}$$

The given formulae for $\bar{J}_1$ and $\bar{J}_2$ can be used to explain the transition from ferromagnetic behaviour for EuO and EuS to antiferromagnetic behaviour in EuTe with increasing lattice constants. Figure 2.6 illustrates this.

With increasing lattice constant, the bandgap energy E_g increases, so $\bar{J}_1$ becomes smaller. Simultaneously, $\bar{J}_2$ increases as the p–d energy separation becomes smaller. Table 2.1 gives an overview of the different lattice constants and coupling strengths for the EuX chalcogenide series from EuO to EuTe, calculated by Zinn [33]. $\bar{J}_1$ decreases with increasing lattice constant, while the antiferromagnetic coupling strength $\bar{J}_2$ increases slightly in magnitude. Note that for EuO one observes two positive coupling strengths for (nn) and (nnn) coupling.

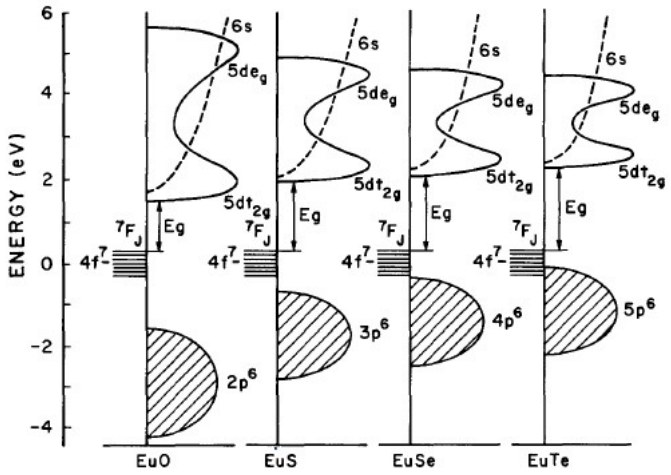

Figure 2.6: Energetic positions of the valence and conduction bands and magnitudes of the bandgap energies E_g for increasing lattice constants from EuO to EuTe. From [20].

/	EuO	EuS	EuSe	EuTe
a_0 (Å)	5.141	5.968	6.195	6.598
$\bar{J}_1$ (K)	0.55	0.21	0.11	0.06
$\bar{J}_2$ (K)	0.15	-0.11	-0.09	-0.20

Table 2.1: Lattice constants and exchange contributions of $\bar{J}_1$ and $\bar{J}_2$ for EuO, EuS, EuSe and EuTe. From [33].

Antiferromagnetic exchange coupling

Antiferromagnetic coupling between rare earth elements and transition metal ferromagnets has been observed experimentally [34] and explained theoretically [35]. The magnetic ordering present in rare earth elements stems from their spin–polarised *4f* states which polarise their *5d* states. The *5d* states in turn hybridise with the transition metal *3d* states, giving rise to indirect exchange interaction with the rare–earth *4f* states. This is also the case with EuS. Antiferromagnetic coupling has been observed below T_C of EuS for the case of EuS/Fe [36] and EuS/Co [24, 37, 38] layers.

Enhancement of T_C

In order to be able to apply EuS in spintronic applications it is necessary to increase its Curie temperature. A short overview of the different approaches so far will be given here.

A first enhancement of T_C to about 60 K was reported in 1994 by Gambino and Fumagalli [22] for the macroscopic ferrimagnet $Co_{1-x}EuS_x$. A few years later, they observed an even stronger increase of T_C to about 160 K (in the same type of macroscopic ferrimagnet), which was a factor of ten compared to the bulk value of 16.5 K.

EuS/Fe layers showed only a slight increase in EuS T_C to about 20 K by Demokritov et al. [21]. In 2006, Müller et al. presented evidence for exchange induced spin–polarisation even at 300K for EuS/Co multilayers [25], attributed to the so–called magnetic proximity effect (MPE). Müller et al. also predicted antiferromagnetic coupling between Ni and EuS and speculated that Ni could also raise the T_C of EuS.

Since the magnetic exchange constants for ferromagnetic (antiferromagnetic) exchange, $\bar{J}_1$ ($\bar{J}_2$) depend on the energetic distance between the $4f$ ($2p$) and $5d$ levels, a decrease of the lattice constant will increase $\bar{J}_1$ and thus T_C. This effect was shown by experiments carried out on Eu chalcogenides at high pressures [39, 40, 41]. However, these have to be seen from a pure scientific point of view, as pressures in the range of 90 GPa would be necessary to raise T_C to RT. As hydrostatic strain is not an option, epitaxial strain would be another option. Thus, the use of substrates with purposely high misfits could lead to the desired decrease of the EuS lattice constant.

Magnetic Proximity Effect

The magnetic proximity effect was given as an explanation for the T_C enhancement in EuS/Co compound by Fumagalli and Müller [25, 42].

As discussed earlier, the ferromagnetic exchange between the Eu^{2+} cations in EuS is thought to originate from virtual $5d$ electrons. In EuS/$3d$ transition metals, the Eu $5d$ bands are thought to hybridize with the $3d$ conduction band so that the virtual electrons are replaced by real ones, which in turn strengthen the exchange interaction between the Eu cations.
The magnetic coupling between EuS and the $3d$ metals is antiferromagnetic. This means, that in principle, the majority spin orientation is antiparallel in both materials. Fe is a majority spin ferromagnetic, meaning that at the Fermi level, the majority spins have a higher density of states than the minority spins, which in turn gives only a few electron spins that are aligned parallel to the Eu $4f$ spins. Thus the T_C enhancement is small in such multilayers.
For Co however, the density of states for minority spins is larger at the Fermi level compared to the majority spins. The larger density of states of minority spins supplies a larger number of electrons having the 'right' spin with regard to the Eu^{2+} $4f$ spin orientation. This is thought to explain, why the T_c enhancements found in EuS/Co layers are higher.
Since Ni also has a higher density of states for minority spins at the Fermi level, like Co, it is also thought to enhance the EuS T_C.

Epitaxial growth of EuS

Epitaxial growth of EuS has been investigated for a long time and a wide range of substrates has been used. In an early attempt in 1964, Chen and Zeitman claimed to have achieved epitaxial growth of EuS on NaCl, NaBr, MgO and CaF_2 while apparently the use of Cu, Ge, Si or mica as substrates led to the formation of polycrystalline films [43]. A few years later, Reichelt and Viehweg reported on the epitaxial growth of EuS on mica [44] and in the early 80's Zinn et al. reported epitaxial growth of EuS on Si [45, 46, 47]. Though some of these results are different and appear contradictory or unplausible, especially regarding the rather large misfits for MgO (42%) and Si (10%), the growth temperature is mentioned as an important parameter in all works.
Zinn used a growth temperature of 900 $°C$ and claims that lower temperatures would lead to polycrystalline growth on Si.
More recent works by Smits et al. [48] and Senba et al. [49] have focused on the growth of EuS on PbS and BaF_2 respectively. Smits found that the growth temperature of EuS influences the ratio of divalent and trivalent Eu found in the layers. Growth at RT led to a high trivalent/divalent ratio while increasing the growth temperature reduced this ratio. On the other hand, increased substrate temperature led to increased roughness in the EuS layers. He concluded, that the best films on PbS could be grown at temperatures between 200 $°C$ and 400 $°C$.

The two substrates InAs and InP, which are used in this thesis, were not used for EuS growth before. Both crystallize in the zinc–blende structure and their lattice constants are 6.058 $\mathring{A}$ and 5.869 $\mathring{A}$ respectively. Compared to the lattice constant of bulk EuS of 5.968 $\mathring{A}$ this gives an absolute misfit of merely 1.5% and 1.7% for InAs and InP, respectively, qualifying both as good candidates for epitaxial growth.

2.1.2 Cobalt

Cobalt is a metal, which is widely used, e.g. in alloys, batteries or as a catalyst. It also plays a role in researching magnetic exchange mechanisms in thin–layer systems. Cobalt is found in compounds in nature. Cobalt belongs to the 3d transitions metals. It's atomic number is 27 with an electronic configuration of $[Ar]4s^2, 3d^7$. Co orders ferromagnetically below its Curie temperature of 1388 K and carries a magnetic moment of $1,7\ \frac{\mu_B}{Atom}$. This makes Co one of only four elements that order magnetically at or around RT. The other three are Iron, Nickel and Gadolinium.
Bulk Co crystallises either in the hexagonally close packed (hcp) or fcc structure. The transition from hcp to fcc occurs at a temperature of 722 K. The energy difference between both phases however, is so small that random intergrowth of both is common.

The lattice parameters for *hcp* are $a = 2.51$ $\mathring{A}$ and $c = 4.07$ $\mathring{A}$. The fcc lattice constant is $a = 3.55$ $\mathring{A}$.

2.1.3 Nickel

Ni has an atomic number of 28 and belongs also to the transition metals. Its electronic configuration is $[Ar]4s^1, 3d^9$. Its Curie temperature is 727 K and it carries a magnetic moment of 0.6 $\frac{\mu_B}{Atom}$. Ni crystallises in the fcc structure with a lattice constant of $a = 3.52$ $\mathring{A}$.

Effective magnetic moment

The magnetisation is defined as the magnetic moment μ per volume V, or

$$M = \frac{d\mu}{dV} \tag{2.7}$$

The effective magnetic moment of a material, e.g. for a single monolayer, can then be calculated by the following formula:

$$\mu_{Vol} = \frac{\mu[\frac{\mu_B}{Atom}] \cdot N[Atoms] \cdot V_{layer}[cm^3]}{V_{unitcell}[cm^3]} \tag{2.8}$$

where N is the number of atoms per unit cell and V the volume.
Ni and EuS crystallize in the fcc structure, so each has four atoms per unit cell. The volume of a unit cell is given by $V_{fcc} = a^3$. In the case of a *hcp* structure one has six atoms per unit cell and the volume of the unit cell is given by $V_{hcp} = \sqrt{3} \cdot \frac{3}{2} \cdot a^2 \cdot c$.

2.2 Methods

This section will give an overview over some of the methods that are useful to characterize the growth and magnetic behaviour of samples. A brief introduction to each measurement technique will be given.

2.2.1 Molecular beam epitaxy and film growth

Molecular Beam Epitaxy (MBE) is a method to create single–crystals or crystalline layers. Epitaxy is known as the ordered growth of crystalline layers on a substrate. The substrate and the grown layers can either be of the same material (homoepitaxy) or a different one (heteroepitaxy) [50]. The process takes place either in high vacuum (HV, $p = 10^{-3} - 10^{-7} mbar$) or in ultra high vacuum (UHV, $p < 10^{-7} mbar$). An electron beam (e–beam) is usually used for the evaporation process of the targets (material to be evaporated).

The targets are e–beam heated in their crucibles (e.g. made of tungsten). As parts of the target start to go into the gas–phase, it is evaporated onto a substrate. The deposited amount of material is monitored *in situ* by a quartz balance. As the whole process takes place in HV or UHV, the contaminations by other atoms or gases (e.g. oxygen or nitrogen) and therefore the concentration of defects during growth is reduced. Also, the molecules of the evaporated material have a longer mean free path due to less collisions with atoms or molecules which would occur more often at higher pressures.
Four main processes can occur when the atoms or molecules are evaporated onto the substrate, which are shown in figure 2.7. These are:

1. Adsorption on the surface,
2. nucleation of islands,
3. diffusion across the surface,
4. thermal desorption depending on the substrate's temperature.

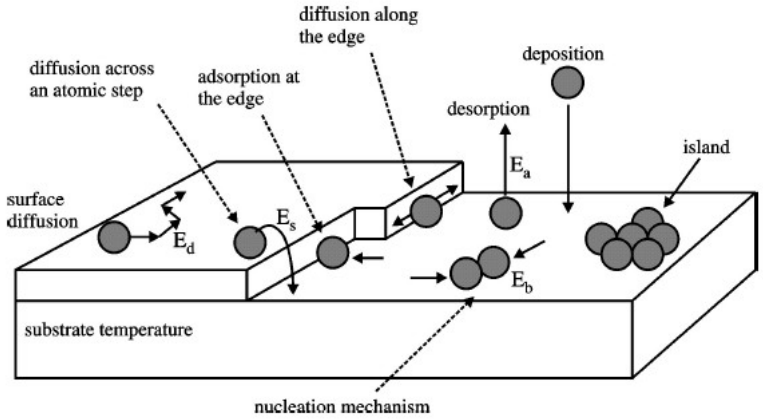

Figure 2.7: Different interaction processes between evaporated atoms and substrate. From [51].

When atoms/molecules are deposited on the surface the most important factor for crystalline growth is the surface diffusion. Through diffusion the adsorbed molecules can move around and form clusters for further growth. The diffusion is hindered by the roughness of the substrate. The value R_{RMS} is a measure of the roughness of the surface. The abbreviation RMS stands for root mean square.
In principle, one can discern three different types of layer growth, which are shown in figure 2.8. These are:

1. layer–by–layer growth (Frank–van–der–Merwe–growth)
2. layer plus island growth (Stransky–Krastanov–growth)
3. island–growth (Vollmer–Weber–growth)

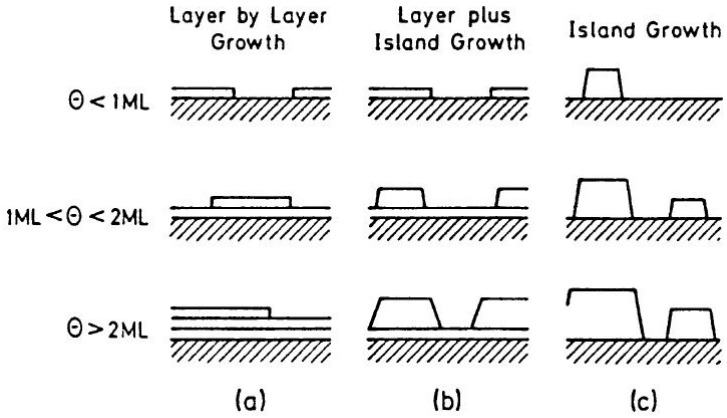

Figure 2.8: Different types of layer–growth. Θ is a measure for the completeness of one monolayer (ML). From [50].

Which type of growth will be present, also depends on the net surface energy given by:

$$\Delta\gamma = \gamma_f + \gamma_i - \gamma_s \tag{2.9}$$

where γ_f, γ_i and γ_s are the film, interface and substrate energies respectively. One observes layer–by–layer growth for $\Delta\gamma < 0$, which is possible if there is no mismatch (or misfit) of the lattice constants of the evaporated film and the substrate (i.e. homoepitaxy, $\gamma_f + \gamma_i < \gamma_s$). Whenever γ_f and γ_s differ from each other one expects either Vollmer–Weber or Stransky–Krastanov growth, depending on the number of layers.

Misfit

The mismatch or misfit of the two lattice constants of the adsorbate and the substrate plays an important role. It is defined as [52]:

$$f = \frac{b - a}{a} \tag{2.10}$$

where b is the lattice constant of the adsorbate and a is the lattice constant of the substrate. If the misfit is small, the evaporated film will grow in the same crystalline structure as the substrate without much tension or distortions due to mismatching lattice constants. Experiments show that one can generally expect layer–by–layer growth up to a mismatch of 10%, though epitaxial growth has been reported for higher misfit values.

2.2.2 Low–energy–electron-diffraction (LEED)

Low energy electron diffraction (LEED) is a method of investigating the periodicity of surface structures. Electron energies usually range from 20 eV and 500 eV. For those energies the de Broglie wavelength λ_{el} is in the lower Angström regime. λ_{el} is given by:

$$\lambda_{el} = \frac{h}{p} = \frac{h}{\sqrt{2m_e E_{el}}} \tag{2.11}$$

where h is Planck's constant, p the momentum, m_e the electron mass and E_{el} the electron energy. Due to the small penetration depth of the low energy electrons, one can simplify the case by treating only two dimensions. If an incoming electron beam hits the surface perpendicularly or at an angle close to 90°, interference is possible when Bragg's law is fulfilled, that is, when the parallel component $K_\parallel$ of the electron wavevector equals a two–dimensional reciprocal lattice vector $G_\parallel$ [50]:

$$\vec{K_\parallel} = \vec{k'_\parallel} - \vec{k_\parallel} = \vec{G_\parallel} \tag{2.12}$$

where $k_\parallel$ and $k'_\parallel$ are the in–plane components of the initial and final electron wavevectors. If the diffracted electron beam originate only from one layer, the third dimension (3rd Laue condition in z–direction) can be ignored and $\vec{K_\perp}$ does not influence the observation of LEED spots. Figure 2.9a illustrates this. Because of the missing third dimension, perpendicular rods appear at the reciprocal lattice points. The Ewald (figure 2.10) sphere with radius k, corresponding to the length of the wavevector, will cut these rods whenever the condition from equation 2.12 is fulfilled. For a two–dimensional surface the LEED intensities from different spots will appear equally sharp.
If more than one surface layer contributes to the diffraction pattern, the third dimension and thus the 3rd Laue condition need to be included. Figures 2.9b–d give an overview how the reciprocal lattice rods change for different surface types. Because of the periodicity along the z–direction, the rods no longer appear equal.
In this case, the scattering phase S needs to be considered. S is the phase difference for electrons scattered from different surface layers, separated by one atomic step. S is given by:

$$S = \frac{k_\perp d}{2\pi} \tag{2.13}$$

where $k_\perp$ is the perpendicular component of the electron wavevector and d the step height between two atomic layers. For integer values of S (in–phase condition), the electrons interfere constructively and sharp LEED spots are observed (see figure 2.9b). For half

integer values of S (out–of–phase condition), the electrons interfere destructively and and broad spots are observed.
For the (00) spot, $k_{\|} = 0$ and S is given by:

$$S = 2d\frac{cos(\theta)}{\lambda_{el}} = 2dcos(\theta)\sqrt{\frac{E(eV)}{150.4}} \tag{2.14}$$

where θ is the angle of incidence with respect to the surface and E(eV) the electron energy. Because of the close–to–normal incidence of the electron beam, $cos(\theta) \approx 1$.

The LEED diffraction pattern can either be visualized using a fluorescent detection screen or a commercially available SPA–LEED setup. In the latter case, a channeltron is used where the electrons are detected. Electrical fields are used to discriminate the incoming electrons and filter the inelastically scattered ones.

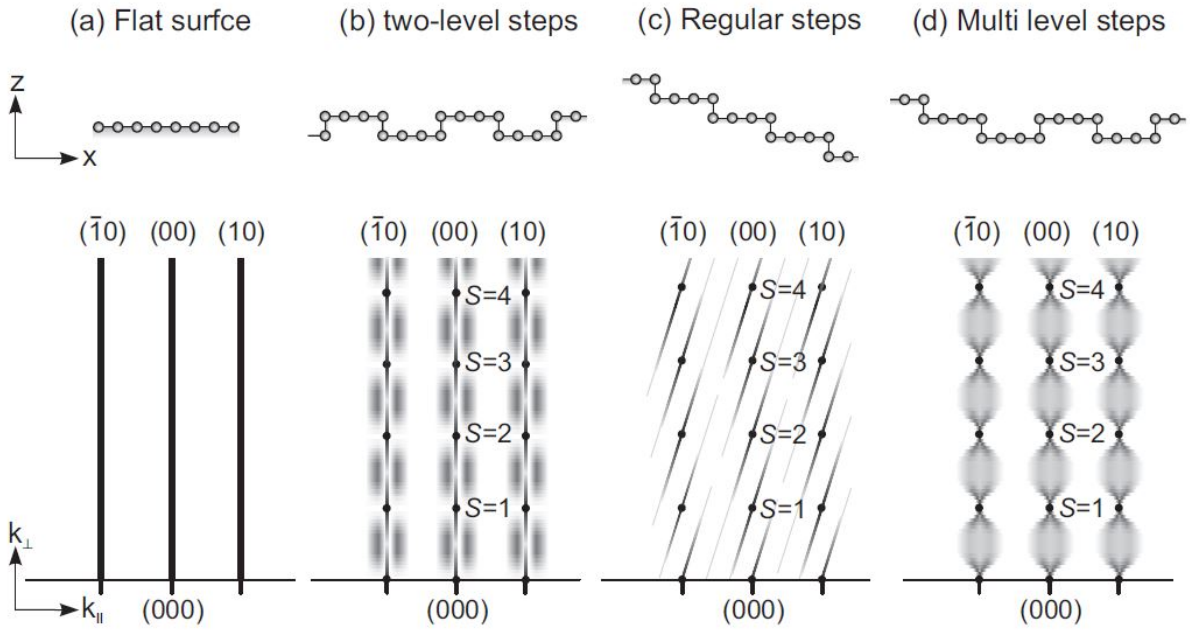

Figure 2.9: LEED diffraction rods for different surface types. From [53].

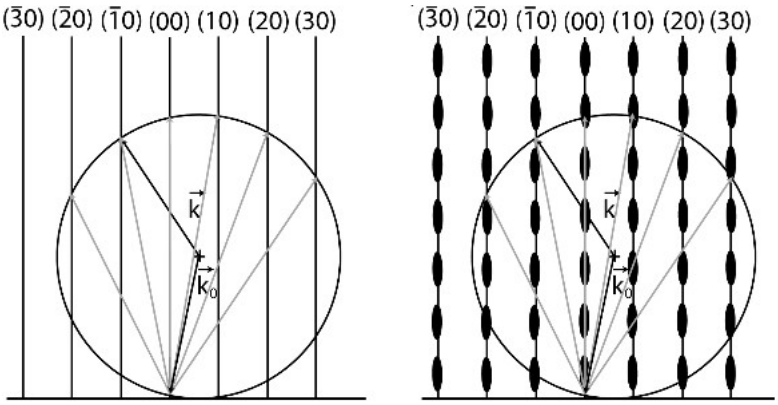

Figure 2.10: Ewald's spheres without (left) and with (right) the effect of considering the third dimension for the diffraction. For the second case, different maxima intensities are observed. From [54].

2.2.3 Auger electron spectroscopy (AES)

The Auger effect, named after Pierre Auger, was discovered in 1925 and is used as a standard method to investigate the elemental compositions of thin films and solids because of its typical probing depths of $10 - 30$ $\mathring{A}$. When an inner shell electron is kicked out, e.g. through incident high energy electrons (≈ 5 KeV), it leaves behind a vacancy in the atom. This vacancy can be filled by the transition of an electron from a higher shell, replacing the initial vacancy. This recombination can be followed by irradiation (x–rays) or it can occur radiationless (Auger transitions or Coster–Kronig transitions). In case of the Auger transitions, the released energy is transfered to another electron, which is then ejected from the atom. The nomenclature in Auger transitions is of an XYZ style, X being the shell of the initial vacancy, Y the shell of the electron replacing the vacancy and Z the shell of the ejected electron. Figure 2.11 shows the ionisation of the inner K–shell (a) and the two subsequent competing processes of x–ray fluorescence (b) and Auger transitions (c). Coster-Kronig transitions do not occur for vacancies in the K–shell [55].
The Auger transition depicted is a KL_IL_{III} transition. The energy of the ejected electron is given by:

$$E_{Kin} = E_K - E_{L_I} - E_{L_{III}} \tag{2.15}$$

The ejected electrons can be detected with a cylindrical mirror analyser (CMA). Due to bad signal–to–noise ratios, a lock–in–amplifier is used so that the final observed spectra are indeed the first derivatives $\frac{dN(E)}{dE}$. The spectra can then be interpreted with the help of reference spectra [56].
A third transition is also possible, the Coster–Kronig transition. They have the same

nomenclature as Auger transitions but occur for vacancies in higher shells. An example is a $L_I L_{II} M_I$ transition. Here, the vacancy in the L_I shell is replaced by an electron of the same shell but different subshell L_{II} and an electron of the M_I shell is ejected.

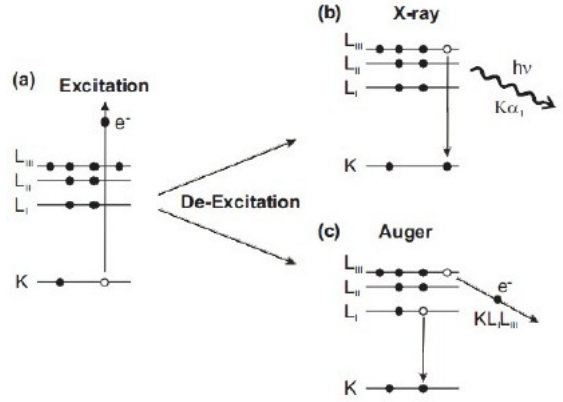

Figure 2.11: Excitation of an inner shell electron by incident high energy electrons (a) and the two de–excitation processes of x–ray fluorescence (b) and Auger transitions (c). No Coster–Kronig transitions are possible for K–shell vacancies. From [50].

2.2.4 Magneto–optical Kerr Effect (MOKE)

MOKE is a standard technique for the investigation of the magnetic properties of thin films [57]. It describes the rotation of the reflected light's electrical field vector by an angle θ_K with respect to the linearly polarised incident light's electrical field vector on a magnetic surface. The effect can be described by the Kerr-rotation θ_K and the Kerr ellipticity η_K. Three different types of MOKEs can be distinguished (shown in figure 2.12): the polar, longitudinal and transversal.

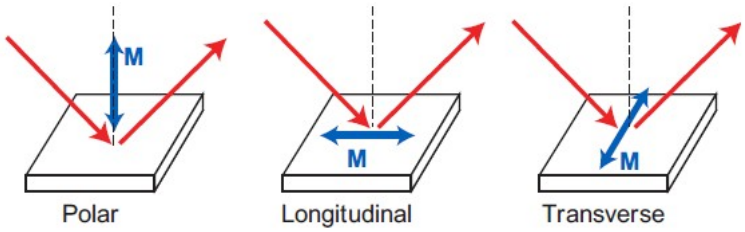

Figure 2.12: Different types of MOKE. From [57].

When the magnetisation of the sample is out of plane, polar MOKE is observed. If the light incidence is perpendicular to the surface, a linear relationship between θ_K and the magnetisation $\vec{M}$ is observed. [58]
When the magnetisation is parallel to the sample and in plane with the incident light,

longitudinal MOKE is observed. In this case, for an incidence angle of 90° a linear $\theta_K - \vec{M}$–relationship applies. In the transversal MOKE the magnetisation is parallel to the sample surface but also perpendicular to the plane of incidence of the light. In the transversal MOKE however, no Kerr rotation is observable. In this case, the intensity of the reflected light can be used as a measure of the sample's magnetisation.
The rotational effects between polar and longitudinal MOKE differ about one order of magnitude, being smaller for longitudinal MOKE. For the sake of a better understanding of the following effects, it is useful to split the linearly polarised light into two components: left circular polarised light (LCP) and right circular polarised light (RCP). If the light propagation is along the z–axis, one gets the following expression for RCP and LCP light:

$$E^{\pm}(t,z) = \frac{E_0}{\sqrt{2}} \cdot (\vec{e}_x \pm i\vec{e}_y) \cdot e^{i(\omega t - kz)} \tag{2.16}$$

where $E^{\pm}$ indicates RCP and LCP respectively, E_0 is the amplitude and $\vec{e}_x$ and $\vec{e}_y$ the unitvectors along x– and y–axis.
Due to magnetically induced anisotropy within the sample, one can expect different values for $n_{\pm}$ and $k_{\pm}$, the refractive and absorption coefficients of the material for RCP and LCP respectively. Both can be combined in a complex refractive index $\tilde{n}$:

$$\tilde{n}_{\pm} = n_{\pm} - ik_{\pm} \tag{2.17}$$

The complex Kerr rotation is defined as:

$$\tilde{\theta}_K = \theta_K - i\eta_K \tag{2.18}$$

$\tilde{\theta}_K$ is connected to the off–diagonal elements $\tilde{\sigma}_{xy}$, which is related to the complex conductivity tensor $\tilde{\sigma}_{\pm}$ by:

$$\tilde{\sigma}_{\pm} = \tilde{\sigma}_{xx} \pm i\tilde{\sigma}_{xy} \tag{2.19}$$

The Fresnel formulas for normal incidence can be used to derive an expression for $\tilde{\theta}_K$. The complex reflection $\tilde{\rho}_{\pm}$ coefficient is given by:

$$\tilde{\rho}_{\pm} = \frac{\tilde{n}_{\pm} - 1}{\tilde{n}_{\pm} + 1}, \tag{2.20}$$

which can also be expressed in polar coordinates:

$$\tilde{\rho}_{\pm} = \rho_{\pm} \cdot e^{i\phi_{\pm}} \tag{2.21}$$

where $\phi_{\pm}$ is the phase. θ_K and η_K are then given by:

$$\theta_K = -\frac{\phi_+ - \phi_-}{2} \tag{2.22}$$

$$\tan \eta_K = -\frac{\rho_+ - \rho_-}{\rho_+ + \rho_-} \tag{2.23}$$

Both equations can be combined to get:

$$\tilde{\theta}_K = \theta_K - i\eta_K \cong i\frac{\tilde{\rho}_+ - \tilde{\rho}_-}{\tilde{\rho}_+ + \tilde{\rho}_-} \tag{2.24}$$

Using the approximations $\tilde{n}_+ + \tilde{n}_- \cong 2\tilde{n}$ and $\tilde{n}_+ \cdot \tilde{n}_- \cong \tilde{n}^2$, where $\tilde{n}$ is the complex index of refraction without magnetic field, one gets:

$$\tilde{\theta}_K = i\frac{\tilde{n}_+^2 - \tilde{n}_-^2}{2\tilde{n}(\tilde{n}^2 - 1)} = \frac{i}{\omega\epsilon_0}\frac{\tilde{\sigma}_{xy}}{\tilde{n}(\tilde{n}^2 - 1)} \tag{2.25}$$

In the last step, the equation was further simplified.

Magneto–optic enhancement effects

Different enhancement effects are known in magneto–optics. The effects need to be considered when recording Kerr spectra and the knowledge about these effects can help interpreting the data. As seen above, the Kerr rotation is dependent on the complex index of refraction. However, this is only true when the magneto–optic material faces the vacuum. Otherwise, the Kerr rotation is connected to the relative complex index of refraction at the layer interface, $\tilde{n}_{rel}$. Equation 2.25 can then be rewritten to:

$$\tilde{\theta}_K = \frac{i}{\omega\epsilon_0}\frac{\tilde{\sigma}_{xy}}{\tilde{n}_{rel}(\tilde{n}_{rel}^2 - 1)} \tag{2.26}$$

One can see, that by changing the interface $\tilde{n}_{rel}$ is changed and thus $\tilde{\theta}_K$, without changing the magnetic properties of the material. If $\tilde{n}_{rel}^2 = 1$, $\tilde{\theta}_K$ is increased infinitely. Among the types of different magneto–optical enhancements are:

1. substrate effect,
2. interference effect,
3. plasma–edge effect.

For the macroscopic ferrimagnet system $Co_{1-x}EuS_x$ another enhancement effect, combining parts of the three already mentioned was found [59]. Here, the optical constants of EuS and Co have similar values in the UV range and $\tilde{n}_{rel} \approx 1$, so that the observed Kerr rotation is enhanced in the higher energy range.

2.2.5 X–ray magnetic circular dichroism (XMCD)

The XMCD spectroscopy measures the difference in X–Ray Absorption (XAS), due to different helicities of the incident x–rays, on a magnetic material. It can be seen as the x–ray equivalent to the MOKE and Faraday rotations which occur in the visible range.
In 1987, G. Schütz and colleagues observed a difference in the absorption for right and left circular polarised light on iron [60]. Nowadays, XMCD is a commonly used technique, thanks to high-energy sources like synchrotron radiation. XMCD is element specific, making it possible to measure their contributions in magnetic samples instead of relying on averaged data [57].
XMCD relies on XAS. For different photon energies it is possible to excite a core–level electron to a higher state. Figure 2.13 gives an energy scheme including the nomenclature of the transition edges, coming from the levels of the excited electrons.

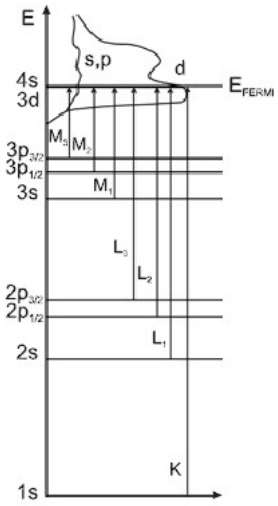

Figure 2.13: Energy level scheme for x–ray absorption. The arrows indicate the necessary threshold energy for the excitations. From [61].

The physical principles of XMCD can be understood from a two–step–system proposed by Stöhr and Wu [62]. In the first step, the angular momentum $\hbar$ and $-\hbar$ from RCP and LCP light respectively are transferred to the excited photoelectron. If no spin–orbit coupling degenerates the core levels, the total momentum is solely transferred to the orbital momentum. If spin–orbit–coupling is present, the angular momentum can be transferred in part to the spin–moment as well. The magnetic properties of the material enter in the second step. Now the spin–split valence band acts as a "detector" for the photoelectron spin, i.e. if the material is ferromagnetic, there will be a difference in occupied spin–up and spin–down states, limiting the transitions into those states. As the transitions are governed by the dipole selection rules ($\Delta J = \pm 1$), the XMCD signal shapes of L_2 and L_3 edges are not the same. Figure 2.14 illustrates the different possible transitions for such a case. A typical XMCD spectrum is shown in Figure 2.15.

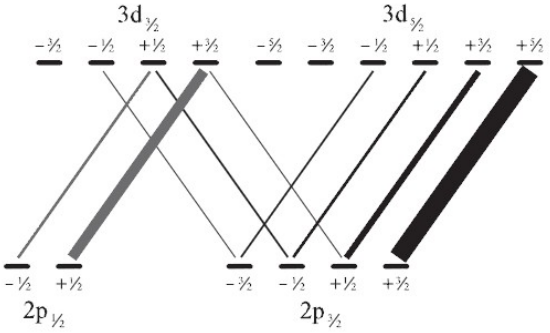

Figure 2.14: Transition probabilities from the L_2 and L_3 edges for RCP light indicated by the thickness of the arrows. Transitions into the $4s$ level are omitted for clarity. From [61].

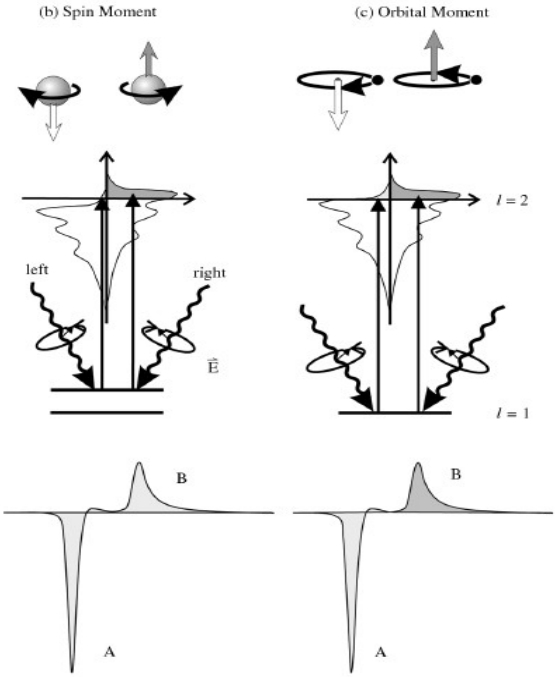

Figure 2.15: XMCD demonstrated by a one–electron–model. The transitions occur from the spin–orbit–split $2p$ band. From [63].

As seen in figure 2.15, the two differences in absorption are denoted A (L_3 edge) and B (L_2 edge). They have opposite signs, coming from the opposite spin–orbit–coupling of their initial states $p_{3/2}$ and $p_{1/2}$ respectively. With the help of sum–rules derived by Thole et al. [64, 65] one can use A and B to calculate the spin and orbital moments. The orbital and spin momentums are proportional to [63]:

$$m_o \propto A + B \tag{2.27}$$

$$m_s \propto A - 2B \tag{2.28}$$

Chapter 3

Experimental Setup

All experiments described in this report require vacuum of a very high quality in order not to pollute the samples with external particles. Two UHV evaporation chambers were used to produce samples for this thesis and will be described in the following sections.

3.1 Balzers UMS 630

The Balzers UMS 630 is an industrially used UHV chamber for e–beam evaporation. It consists of two chambers: a load chamber (LC) for inserting and removing substrates and samples and a main chamber (MC) for evaporation. Both chambers are separated by a plate valve and can be evacuated separately. For this purpose both are equipped with a turbo molecular pump and a rotary disc valve as well as a titanium sublimation pump (TSP).
TSPs are used to reduce the partial pressure of water and hydrogen. Cold–Cathode–Gauges are installed in each chamber to measure the pressure, which is usually in the 10^{-8} $mbar$ regime.
Sample transfers from the LL to the MC are realised with gripping tongs operated on a magnetic rail. Due to the much smaller volume of the load chamber compared to the main chamber, the pressure in the latter does not increase significantly during a transfer.
Inside the main chamber there are four holders for crucibles and three water–cooled electron guns. The acceleration potential for e–beam evaporation can be chosen to be 7 keV or 11 keV.
Due to the kinetic energy of the incoming electrons, the samples are heated. Part of the samples will then change into the gas phase and form a cone–shaped molecular beam with the opening pointing to the chamber ceiling. The evaporation rate can be adjusted by controlling the electron emission via the filament current of the electron gun.
The sample is located above the crucible positions in the centre of the molecular cone. The crucible positions and the substrate are protected by shutters to avoid the deposition

of undesired material and limit the deposition amount on the substrate.
The deposited amount is measured by a quartz balance positioned slightly off the centre of the cone. For an accurate measurement of the layer thickness specific material information like density and acoustic impedance are needed.
A Niob heater is used for heating and annealing the substrate and/or sample. The heater is positioned about 1.5 cm above the sample holder. Temperature control is achieved with a thermocouple in the heater.

3.2 MBE chamber

The CreaTec MSE-F SY06 setup, or MBE chamber in short, is a commercial setup for growing and analysing thin films in UHV environment. A schematic of the chamber is shown in figure 3.1. It contains four main parts: the load chamber (LC), load–lock (LL), growth chamber (GC) and analysis chamber (AC). Each chamber can be separated from the others with plate valves.
Samples are mounted on a holder which has clamps holding the sample piece in position. The usual sample size is 1 cm x 1 cm. The first holder is then inserted into a 2 inch holder that can be inserted into holder positions having bayonet sockets. The second holders are moved around in the chamber by transfer guides. For locking and unlocking the 2 inch holder from the bayonet sockets, the holders have to be rotated by a certain degree to unlock them. This is achieved by an external magnetic piece on the transfer guides which allows rotation of the holder.
The samples are loaded into the MBE chamber from the LC, which contains four positions. The load chamber has a turbomolecular pump attached to it and usually reaches pressure values in the 10^{-8} $mbar$ regime. Transfer from the LC to the LL are usually very fast, so that there is a minimum contamination of the LL.
The LL contains four holder positions, one of which is equipped with a heating wire for heating the substrates or samples to temperatures up to 1400 $°C$. A thermocouple is located behind the sample holder to measure the temperature. Additionally, the LL contains a sputter gun using Argon gas, which is used to sputter the surfaces of the substrates in order to clean them. Afterwards, or during sputtering, the substrate surfaces can be heated. Next to a turbomolecular pump, an additional ion getter gauge is also installed in the LL.
Growth of the thin films takes place in the GC. Materials are evaporated from an electron beam evaporation source with one material position (filled with EuS grains) and a high temperature effusion cell reaching up to 2000 $°C$. Like the LL, the GC contains a turbomolecular pump and ion getter. The evaporators are facing upwards, so the sample holder has to be rotated by 90° in oder to face downwards. A quartz microbalance is

installed in the GC for measuring the film thickness. It is installed in the vicinity of the sample holder. The sample holder in the GC is also equipped with a heating wire which can reach the same temperature as the one in the LL.
Analysis of the substrates and samples is done in the AC, which contains a Auger spectrometer, a SPA–LEED and a combined STM/AFM setup. The AC contains one ion getter pump. The holder in the AC is also equipped with a heating wire and can reach the same temperature values as the two other holder found in the GC and LL.
To further improve the vacuum, TSPs are installed in every chamber and periodically switched on for a couple of minutes. The achieved base pressure in the MBE setup is around $3 \cdot 10^{-10}$ $mbar$.
An additional polar Kerr spectrometer is indicated in the schematic setup. Currently, the spectrometer is not operated and is undergoing repair. Also, a cryostat will be added to the setup to enable temperature dependant measurements.

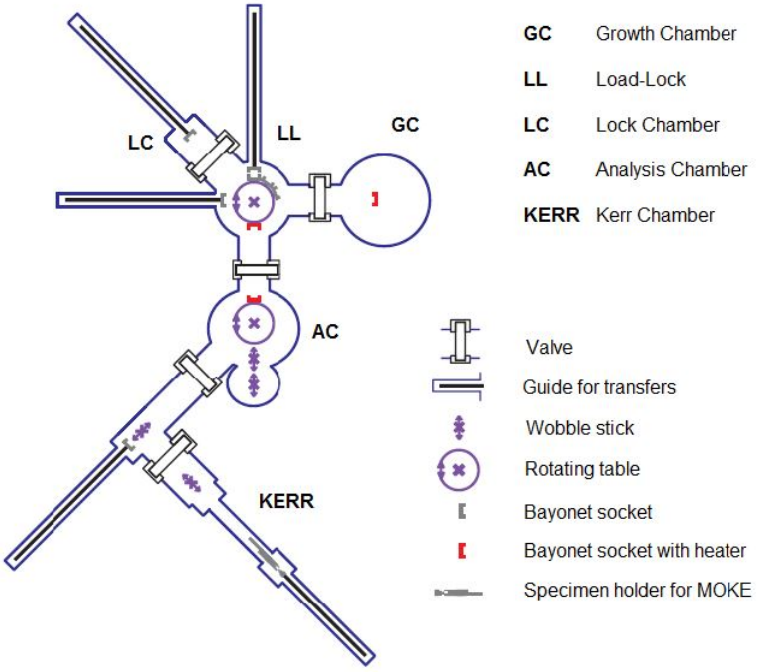

Figure 3.1: Schematic setup of the Createc MBE chamber. The load (LC), lock (LL), growth (GC) and analysis (AC) chamber have been indicated. From [66].

3.3 MOKE setup

A polar Kerr spectrometer was used for the magneto–optical Kerr effect measurements. The spectrometer is designed for recording polar Kerr spectra from an energy range between 0.7 eV to 5 eV and magnetisation curves at a given energy for varying magnetic fields. The resolution of the Kerr rotation is about $2° \cdot 10^{-3}$. All measurements are

computer–operated. The setup is shown in figure 3.2. The magnetic field is supplied by a water–cooled double coiled magnet with two different polar caps. Depending on the polar caps and their distance one can have maximum field strengths between 1.6 T and 2.4 T. The whole setup is placed on an optical table and covered by a wooden box to prevent any straylight interfering with the measurement. The following part will give a quick overview of the different components in the setup.

As lightsources there are a Halogen lamp (150 W), covering the infrared (IR) and visible (VIS) light range and a Xe–lamp (300 W) used for the ultraviolet (UV) range. The generated light enters the monochromator, which consists of a double grating with different gratings for IR, VIS and UV. Additionally, optical filters can be placed in front of the outgoing beam to suppress the second harmonics of the light. The light is then reflected by a set of planar and spherical mirrors (focal length of 30 cm), passing a polariser and another mirror which directs the light onto the sample. Glan–polarisers are used for the analyser and polariser which show a small beam displacement. However, their acceptance angles for incoming light are not symmetric for all energies. For the visible energy range the polarisers show an almost symmetric behaviour. However, for UV light there is an asymmetry of about 4° which needs to be accounted for by slightly tilting the polarisers. The samples are mounted on a pole and positioned in the center between the two polar caps where the field is maximal. The polar caps have small openings where the light can pass through. The incidence angle of the light with respect to the surface normal is about 2.5°. The light is then reflected by another mirror into the Faraday modulator, where the polarisation of the light is periodically modulated using the Faraday effect. The modulator itself consists of a water–cooled coil and a set of different glas–rods, used for different energy ranges. Behind the Faraday modulator the light passes the analyser, a set of remaining mirrors and is then detected, using a lock–in–technique. Detection in the far IR is realised using an InGaAs diode, for the near IR a Si diode can be used. A photomultiplier tube is used for the VIS and UV ranges.

Measurement principle

The analyser starting position is rotated by 90° with respect to the polariser. Aluminum is used as a reference for measuring the MOKE of samples, because it has a negligible Kerr rotation. When measuring Al, the analyser displaced from its initial position of minimal intensity by a certain angle, i.e. 3° and the lock–in–signal is measured for each angle position. For the intensity one gets the following relationship:

$$I_\alpha \propto |sin[2(\theta_K - \phi)]| \tag{3.1}$$

where I_α is the measured intensity at a certain angle, θ_K the position of minimal intensity and ϕ the analyser position. For small angles α near the angle of minimal intensity the relation $sin(x) \approx x$ holds. One measures so–called V–curves which are displaced with respect to each other depending on the time constant on the lock–in–amplifier. Fitting of the V–curves gives the Kerr rotation (with respect to Al) and the reflectivity for each sample.

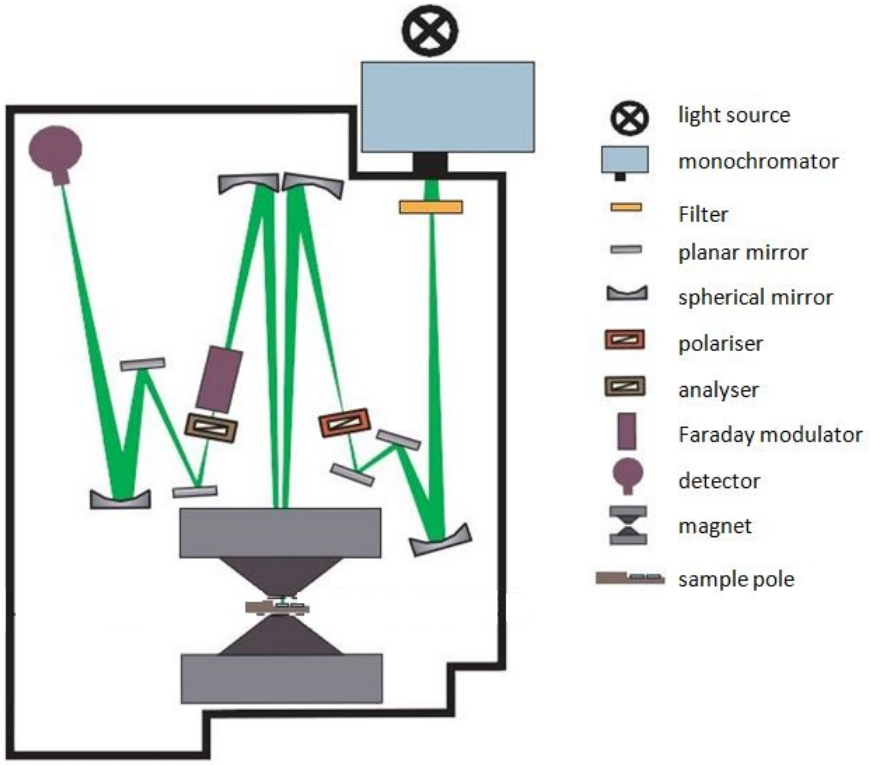

Figure 3.2: Polar MOKE setup showing the different components. From [66].

Chapter 4

EuS multilayers

This chapter will deal with multilayers of EuS and *3d* transition metals, namely Co and Ni. Polar MOKE measurements and XMCD measurements will be shown and discussed. Part of the data shown in 4.2.2 and 4.2.3 has been obtained during the course of two master theses written by Michael Scott [67] and Arne Grotenrath [68]. Both students were personally guided through their experimental and theoretical work.

4.1 Sample preparation

All samples discussed within this chapter were prepared by e–beam evaporation in UHV in the Balzers chamber.
Electron–beam evaporation is the technique best suited for EuS evaporation because of the high sublimation temperature ($\approx 2400\ ^{\circ}C$) of EuS. Powder was chosen for EuS as target material. For the samples containing Co, Ni and Pd, pellets were used. All materials were evaporated at RT from tungsten crucibles at rates between $0.3 - 1.0\ ^{\mathring{A}}/_{s}$. Thicknesses deposited were checked *in situ* by a quartz microbalance. Si(111) with native oxide was used as a substrate for all samples. Samples with perpendicular magnetic anisotropy (see sections 4.2.2 and 4.2.3) started with a Pd buffer layer of 7 nm, followed by the Co/Pd multilayer. Co/EuS and Ni/EuS multilayers were evaporated on top of the Co/Pd multilayer at the end. All samples terminated with EuS, as it is stable against oxidation.

4.2 Analysis of EuS/Co multilayers

In the follwing section, EuS/Co multilayers will be discussed. Analysis of the growth of the multilayers will be shown. Their magnetic behaviour has been analysed by XMCD and polar MOKE and the results will be shown.

The layering quality and bilayer thickness were evaluated by X-Ray Reflectivity (XRR) on a Bruker Discover D8 reflectometer, equipped with a Göbel mirror, using CuK_α radiation. Real-space images were taken with a JEOL 2011 high-resolution transmission electron microscope (HRTEM) operating at 200 kV, with a point resolution of 0.23 nm. TEM specimens were prepared by mechanical polishing, followed by ion milling in mild conditions.
XMCD experiments were performed at the ID12 beamline of the European Synchrotron Radiation Facility (E.S.R.F.) in Grenoble (France) at the $L_{3,2}$ edges of Eu using a highly efficient fluorescence yield detection mode in a backscattering geometry. The measurements were carried out at RT with the help of an electromagnet working up to 6.5 kOe. The experiments were performed at grazing incidence. To exclude any experimental artefacts, the XMCD spectra were recorded either by changing the helicity of the incoming light or by inverting the direction of the external magnetic field.

4.2.1 XMCD of EuS/Co multilayers

During earlier work on EuS/Co multilayers, many different samples were produced and analysed regarding their growth characteristics and magnetic properties [24, 25, 69, 70]. Two new multilayers, S25, consisting of a multilayer of $[EuS(4\ nm)/Co(7\ nm)]_9$, and S26 [1], consisting of a multilayer of $[EuS(2\ nm)/Co(7\ nm)]_{15}$ were measured with XMCD at the E.S.R.F. The results of these samples were published [71] and shall be briefly described here.

The quality of the multilayers was measured by means of X–Ray–Reflectivity (XRR). The results are shown in figure 4.1. For clarity, an offset was added to the data of S25. S25 shows three Bragg peaks while S26 only shows one. The multilayer structure is confirmed by the presence of the Bragg peaks, however, no additional Kiessig fringes [72] are found. Their absence as well as the relatively low number of Bragg peaks, especially for S26, points to some roughness within the layers which was observed for similar EuS/Co [66] multilayers by TEM as shown in figure 4.2.

The magnetic response of Co and EuS was for both samples by XMCD. Measurements were performed at 2.5 K and RT with and without external magnetic field. The Co K–edge and Eu L_2– and L_3–edges were probed.
The x–ray–absorption (XAS) spectra shown in figure 4.3 were recorded at 2.5 K and show the presence of divalent and trivalent Eu. The peaks originate from transitions from the divalent (first peak) and trivalent (second peak) Eu $2p$ to $5d$ band.

[1] The author of this thesis has produced both during the course of his master thesis

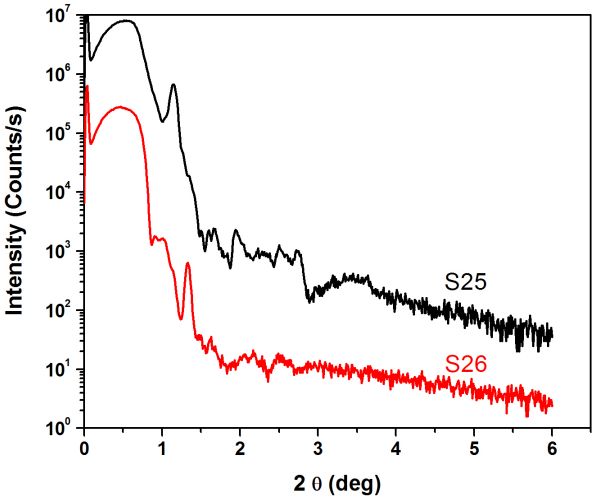

Figure 4.1: X–ray–reflectivity measurement of S25 and S26.

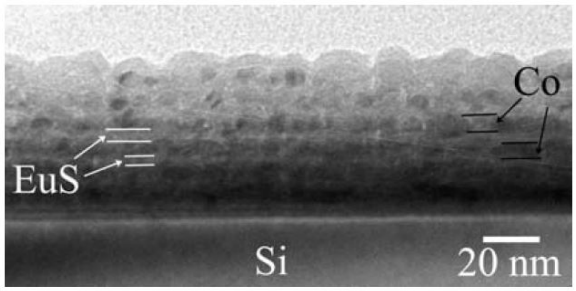

Figure 4.2: TEM of a EuS(4nm)/Co/4nm)x6 multilayer showing the increasing interface roughness with increasing number of layers. From [70].

Trivalent Eu is unwanted because of its $J = 0$ and it will not posses a magnetic moment. Trivalent Eu has been found to exhibit Van–Vleck–paramagnetism in EuN [73] and Eu_3S_4 [74]. The trivalent Eu will however, not contribute to the XMCD signal.
The different valency in EuS compounds is already known [75]. Trivalent Eu may originate from defects, pressure or the application of high magnetic fields. During the measurement, no pressure was applied to the samples, however, some interfacial strain on the EuS layers from Co cannot entirely be excluded. It is known, that growing EuS at a temperature below 400 $°C$ produces defects [76], so they seem to be the main reason for the presence of Eu^{3+}. Only the divalent Eu atoms will carry a magnetic moment of 7 μ_B because of their $J = 7/2$.
The percentage of divalent and trivalent Eu in samples S25 and S26 was estimated (details in [71]) and it was found that S25 posseses about 63% and S26 about 45% divalent Eu which in turn will give a magnetic moment of 4.40 μ_B and 3.15 μ_B respectively.
XAS and XMCD measurements of the Co K–edge have shown that Co was in a hcp structure and followed the external magnetic field at all temperatures.
A direct application of the sum rules for the Eu $L_{2/3}$ edges is not possible due to a mixing of dipole ($2p \rightarrow 5d$) and quadrupole ($2p \rightarrow 4f$) transitions which complicates the calculation. In principle, the L_2 edge is proportional to the magnetic moment found in EuS. As a proof–of–principle for the spin–polarisation found in such EuS/Co layers, the presence of the L_2 XMCD signal is sufficient. Applying the sum rules to Co is possible, but unnecessary, as the absolute value of its magnetic moment is not of interest here.

Figure 4.4 shows the measured XMCD signals for S25 and S26 at 2.5 K and RT measured at different magnetic fields. At 2.5 K the remanence signal is larger for S25 than for S26

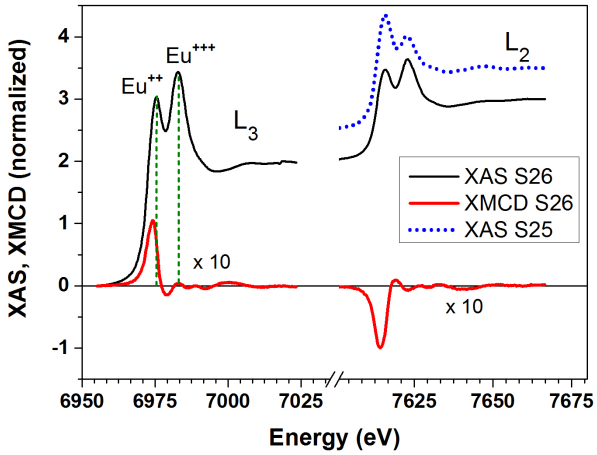

Figure 4.3: X–ray–absorption spectra of samples S25 and S26 at the Eu L_2 and L_3 edges.

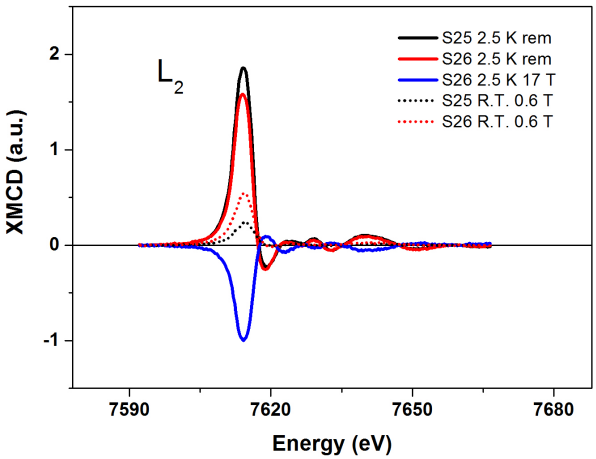

Figure 4.4: XMCD measurements of samples S25 and S26 at the Eu L_2 edge. For clarity the signals at 2.5 K and RT have been multiplied by a factor of 10 and 50 respectively.

which is due to the larger number of divalent Eu atoms found in S25. The signal at 17 T is not as large as in remanence which is explained with the antiferromagnetic coupling found between Co and EuS.

To clarify this further, element–specific hysteresis curves recorded at 2.5 K are shown in figure 4.5. Co is always oriented parallel to the external magnetic field while Eu is oriented antiparallel at zero magnetic field. Increasing the magnetic field will rotate the Eu magnetic moments parallel to the field leading to a minimization of the Zeeman energy. For S25, the Eu magnetic moment is aligned parallel to Co at 2.5 K and 5 T. However, as seen in figure 4.4 at 2.5 K 17 T are not enough to rotate the magnetic moments of S26 fully parallel to the field. As seen in figure 4.5, the Eu magnetisations of S26 at remanence and under applied field are still considerably different. So the strength of the antiferromagnetic coupling between Co and EuS seems to be inversely proportional to the EuS thickness (S26 has half the thickness of EuS layer compared with S25).

At RT the XMCD signals of S25 and S26 are reduced compared to low temperatures but still show antiferromagnetic coupling between Co and EuS, as seen from the element–specific hysteresis loops at RT shown in figure 4.6. The antiferromagnetic coupling is intact up to a magnetic field of at least 0.6 T (higher fields could not be applied during this measurement) which points to ferromagnetic ordering in the EuS layers. An increase of the ordering temperature this high has been observed for the first time in these multilayers. Comparing the magnitude of the XMCD signals at both temperatures can give an estimate of the magnetic moment Eu at RT [71]:

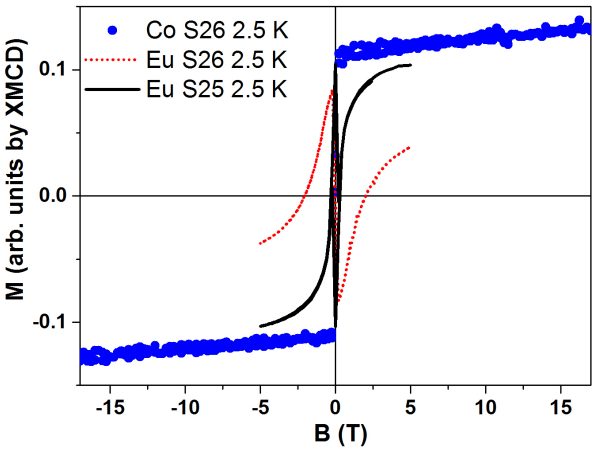

Figure 4.5: Element specific magnetisation curves of samples S25 and S26 at 2.5 K.

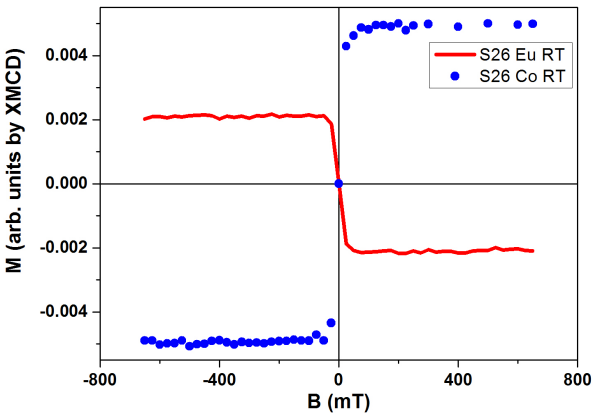

Figure 4.6: Element specific magnetisation curve of sample S26 at RT.

$$\mu_{Eu,RT} = \frac{XMCD_{RT}}{XMCD_{2.5K}} \cdot \mu_{Eu,2.5K} \tag{4.1}$$

Applying equation 4.1 to the XMCD results of S25 and S26 gives values of 0.1 μ_B and 0.5 μ_B respectively. The value found for S26 is comparable to the magnetic moment of Ni at RT (0.6 μ_B).

4.2.2 Perpendicular Magnetic Anisotropy in Co/Pd multilayers

Similar EuS/Co multilayers were also investigated by means of pMOKE, a common measurement tool for magneto–optical systems. In contrast to XMCD, pMOKE is not element specific but makes up for this disadvantage by being highly sensitive down to only a few nanometers, in contrast to XMCD, which needs thicker layers or more repetitions to increase absorbance. Under some circumstances, it is possible to discern the influences of different materials in pMOKE (e.g. in multilayers). As the name suggests, pMOKE is sensitive to the polar component of the magnetic moment of the measured sample. For samples with in–plane magnetic anisotropy, no or only a very small signal will be measurable in remanence measurements (depending on the surface anisotropy). Either one has to rotate the magnetic moment of the sample out of plane by an external magnetic field (and saturate it, if the magnetic field is large enough) or introduce Perpendicular Magnetic Anisotropy (PMA) in the sample, which will rotate the magnetisation of the samples out of plane.

It is known that Co/Pd multilayers have PMA for a range of Co thicknesses smaller than 10 $\AA$. The effect is present for a wider range of Pd thickness, ranging from 10–40 $\AA$. The reason for this PMA is the volume and interface anisotropy energies of Co when sandwiched between Pd layers.

For layers with the thicknesses mentioned above, it is possible to introduce a high degree of PMA in such multilayers. The PMA would then be retained even if additional, thicker layers of EuS and Co were added on top and thus make measurements in remanence possible.
As seen from the XMCD measurements, at 5 K it was impossible to break the antiferromagnetic coupling between EuS and Co (see figure 4.4. At RT, a decrease of spin–polarisation was found in EuS but the antiferromagnetic coupling was still present. However, it is likely that the coupling is less strong at RT and it could be possible to break this coupling apart by applying a sufficiently large external magnetic field. In such a case, the signal measured by pMOKE in remanence would correspond to a combined signal of the magnetic moments of EuS and Co which are antiferromagnetically coupled. In contrast, a measurement with maximum applied magnetic field would give a (maybe only partly) parallel signal of the two magnetic moments.
As a start, a number of magnetic substrates (MS) were fabricated and their degree of PMA checked by pMOKE. To characterize the quality of the MS one can introduce the squareness S, defined as

$$S = \frac{\theta_{K,rem}}{\theta_{K,sat}} \tag{4.2}$$

where $\theta_{K,rem}$ and $\Theta_{K,sat}$ are the Kerr rotations measured in remanence and saturation with applied magnetic field respectively. A good magnetic substrate has its magnetisation perpendicular to the surface without magnetic field and is characterized by a value of S close or equal to 1.

The MS were fabricated in the Balzers chamber by evaporation of Co and Pd on silicon wafers with native oxide. No prior treatment of the wafers was performed before evaporation. All MS start with a thicker Pd buffer layer of about 70 $\mathring{A}$, followed by four repetitions of $[Co(t)/Pd(20\mathring{A})]_4$, where t is the Co thickness. The choice of Pd thickness and layer repetitions was motivated by previous work on Co/Pt multilayers that show PMA and values found in literature [77, 78, 79]. A MS with a Co thickness of 4 $\mathring{A}$ showed a very high degree of squareness with almost rectangular shaped hysteresis curve. In an attempt to enhance the propagation of perpendicular magnetic anisotropy introduced by the MS in the additional Co/EuS layers added on top of the MS, the Co thickness could be increased to 6 $\mathring{A}$ while retaining the high degree of squareness.

Figure 4.7 shows a hysteresis loop of such a magnetic substrate measured at 2.5 eV at RT. The measured Kerr rotation is negative for positive magnetic fields, reaching a maximum value of just above $-0.06°$. While reducing the magnetic field to zero, the measured Kerr rotation stays almost constant at this value and the entire magnetic moment abruptly flips at an coercive field between -50 and -100 mT, in accordance with values of around

50 mT as found in literature [77].
The Kerr rotation is now positive at just above 0.06° until -2.1 T. Upon increasing the magnetic field to complete the loop, the measured Kerr rotation symmetrically switches from its positive value at negative fields to its original negative value between 50 and 100 mT.

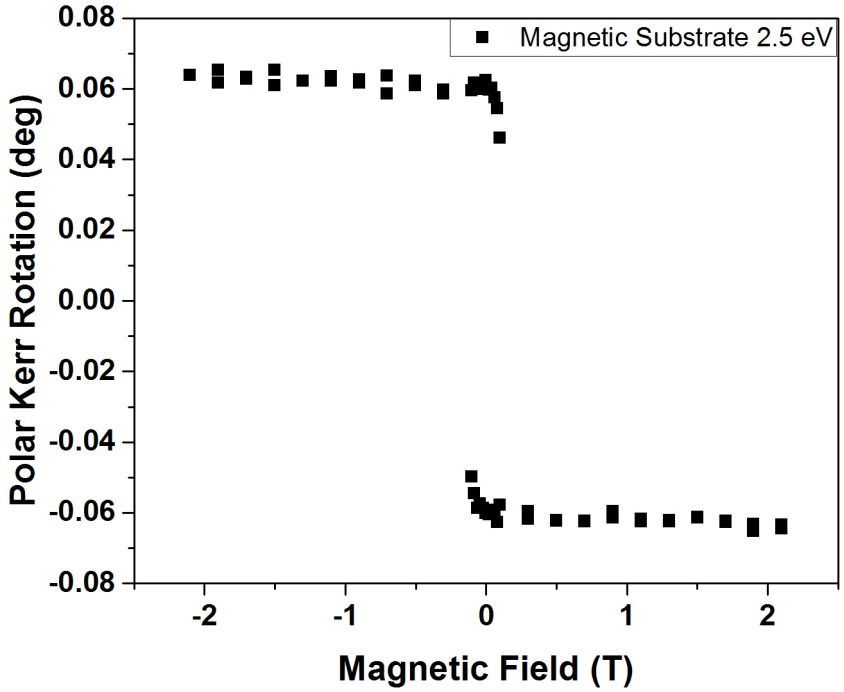

Figure 4.7: Hysteresis loop of a magnetic substrate with Co thickness of 6 $\AA$ recorded at 2.5 eV and 300 K.

Kerr spectra recorded with applied magnetic field of 2.2 T and in remanence for both Magnetic substrates with 4 and 6 $\AA$ referred to as MS(4) and MS(6) hereafter, are shown in figure 4.8. As seen by the difference of remanence and applied field measurements the difference of the spectra for both samples is small. An estimate of the squareness gives $S = 0.95$, showing that both magnetic substrates used are of good quality.
The spectral characteristics of both magnetic substrates however, show some differences. The Kerr rotation of MS(4) with applied magnetic field is almost constant over the entire energy range starting at around $-0.01°$ at 1.9 eV and ending at $-0.01°$ at 4.7 eV. The spectrum is slightly 'bend', peaking at around $-0.02°$ around 3 eV. The same behaviour holds for the remanence spectrum, though the values are only about 95 % of those given for the maximum field measurement.
In contrast, the absolute values recorded for MS(6) are higher. The spectrum starts at around $-0.06°$ at 1.9 eV, again being slightly 'bend' between 1.9 eV and 3.3 eV ($-0.06°$), peaking at 2.6 eV at $-0.069°$. After 3.3 eV the absolute value of the Kerr rotation increases to a value of $-0.115°$. Additional kinks can be found in the spectrum

at 3.6 and 4.3 eV. The change of spectral behaviour can be attributed mainly to the presence of more Co in MS(6) and might also be due to polarisation of the Pd layers by Co. Similar spectral behaviour and an increase of Kerr rotation with Co thickness has been investigated in Co/Pd multilayers by C. D. England[80].

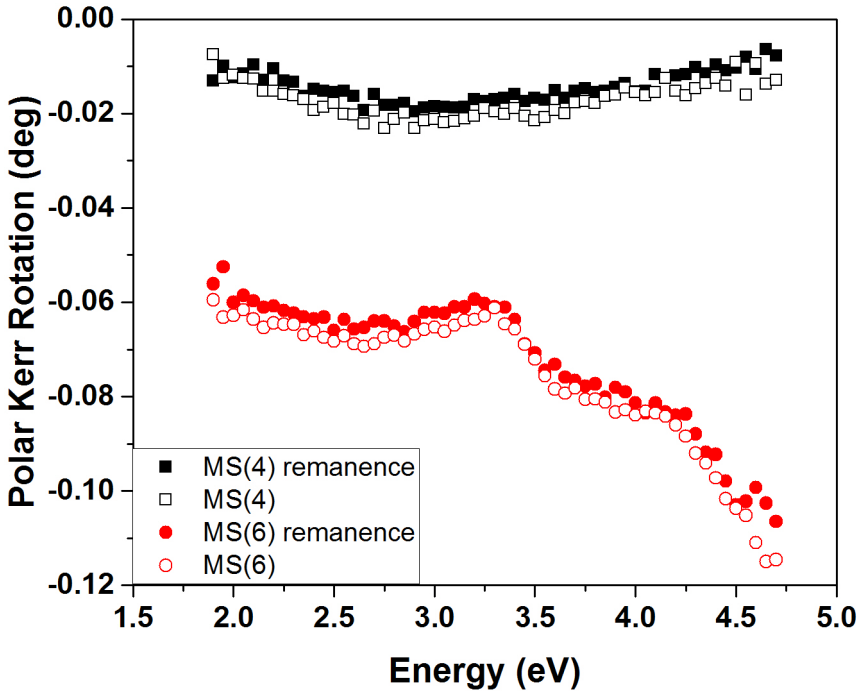

Figure 4.8: Polar Kerr spectra of MS(4) and MS(6) recorded in remanence and with applied magnetic field of 2.2 T at 300 K.

To check if the magnetic substrates will introduce a degree of PMA in thicker EuS/Co layers added on top, an additional $Co(20\ \mathring{A})/Pd(20\ \mathring{A})$ layer was added on top of MS(6). The hysteresis loop and spectra of the sample are shown in figures 4.9 and 4.10 respectively. The squareness of this sample is about 0.58. The two spectra do not show significant features, both absolute values of the Kerr rotation increase with energy and both spectra only differ by the inverse factor of the squareness, as illustrated. The absolute values of θ_K have increased again in comparison to MS(4) and MS(6) as expected due to the larger amount of Co and the spectral shape is similar to MS(6) but without the 'kinks' that have disappeared.
The fact that both spectra only differ by a factor could be due to three reasons:

a) there is no paramagnetic Pd contribution in the Kerr spectra,
b) the paramagnetic Pd contribution is very small and undetectable,
c) the paramagnetic Pd contribution is always present due to polarisation from the Co layers.

In conclusion, the MS(6) provided a good starting point for investigating EuS/Co multilayers with perpendicular magnetic anisotropy.

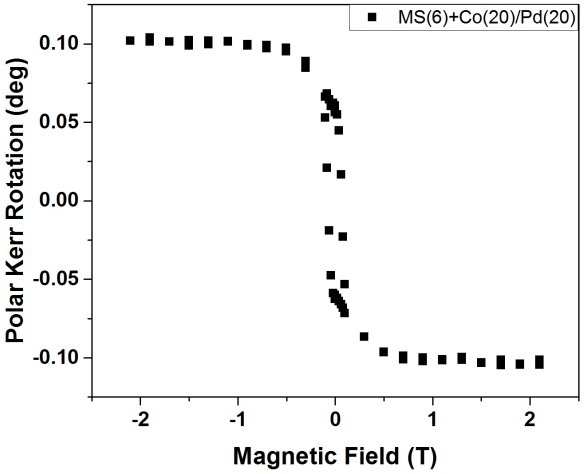

Figure 4.9: Hysteresis loop of a bilayer of Co/Pd with 20 $\AA$ thickness each on top of MS(6).

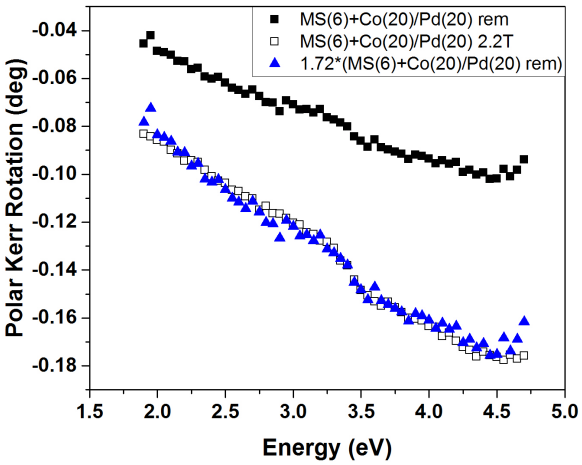

Figure 4.10: Energy spectra of polar Kerr rotation of a bilayer of Co/Pd with 20 $\AA$ thickness each on top of MS(6) measured at remanence and 2.2 T.

4.2.3 Polar MOKE measurements of EuS/Co multilayers

Samples A–C

After finding the proper thickness values to produce magnetic substrates with good quality, a series of EuS/Co multilayers was prepared. An overview of the first three samples, named A, B and C is given in table 4.1.

sample name	Substrate	Structure (Å)
A	MS(6)	$[Co(10)/EuS(20)]_3$
B	MS(6)	$[Co(15)/EuS(40)]_2$
C	MS(6)	$[Co(20)/EuS(40)]_2$

Table 4.1: EuS/Co multilayers prepared on MS(6) with different number of repetitions and varying Co and EuS thickness. Thickness is given in Å.

As seen in figure 4.9, increasing the amount of Co deposited on the MS, decreases the squareness. Surface roughness will also decrease the amount of perpendicular anisotropy. As evident from the XRR measurements presented earlier, there is a considerable amount of surface roughness in EuS/Co multilayers with increasing number of repetitions (see figure 4.1 for S25 and S26). That is why a 2–3 repetitions of EuS/Co layers was chosen for these samples. Hysteresis loops of the samples were taken at two different energies: 2.5 and 4.1 eV.
The first value was chosen because it lies in the middle of the visible energy range (approximately $2-3$ eV) and close to the EuS absorption maximum at RT (2.3 eV). The second value was motivated by the maximum rotation found when measuring the spectra of all samples between 1.9 and 4.7 eV. The Hysteresis loops measured at 2.5 eV are shown in figure 4.11a to 4.11c.
All samples show a substantial degree of squareness that decreases from sample A (0.85) to B (0.65) to C (0.45) with increasing individual Co layer thickness in the Co/EuS multilayers. The coercive fields are in the range of 100 mT, comparable to the magnetic substrates. Sample A appears to be saturated over the whole scanning range, sample B saturates between 500 and 700 mT and sample C at around 1 T. However, no sign of antiferromagnetic coupling (i.e. by rotation of part or all of the Eu magnetic moment at some field strength) by unusual behaviour of the hysteresis loop is observed at 2.5 eV. This might be due to the small amount of absorption in thin EuS layers for this energy [81] range and the small to negligible contribution of EuS at RT.

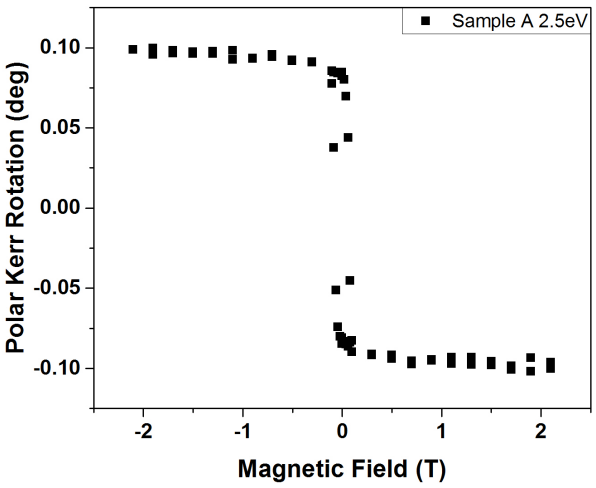

(a) Polar Kerr Hysteresis loop of Sample A at 2.5 eV

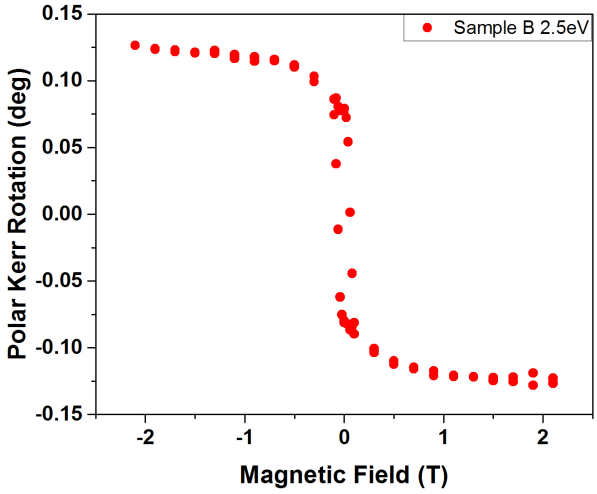

(b) Polar Kerr Hysteresis loop of Sample B at 2.5 eV

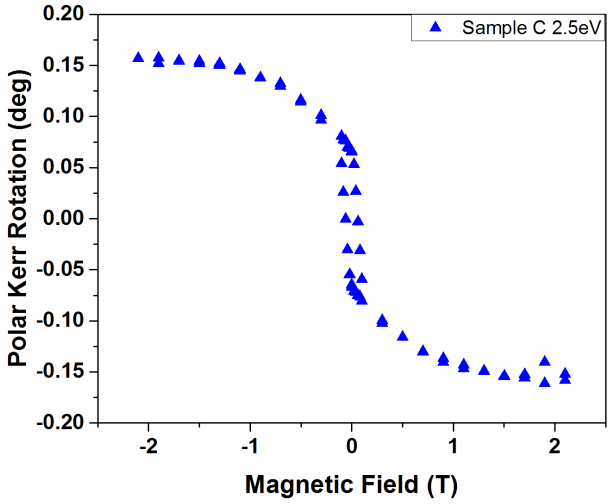

(c) Polar Kerr Hysteresis loop of Sample C at 2.5 eV

Figure 4.11: Hysteresis loops of samples A–C at 2.5 eV

Hysteresis loops recorded at 4.1 eV are shown in figures 4.12a to 4.12c. In contrast to the measurements at lower energy, the samples now saturate at higher magnetic fields and do not show the same degree of squareness as before. Sample A saturates at around 1.5 T and has around 60% squareness. Sample B and C saturate at 1.3 and 1.5 T with about 46% and 23% squareness, respectively. For a direct comparison of the two hysteresis curves of each sample, they have been plotted together in figure 4.12d.

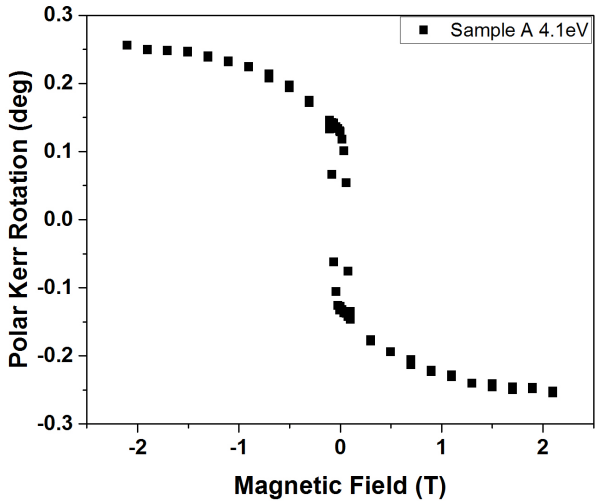

(a) Polar Kerr Hysteresis loop of Sample A at 4.1 eV

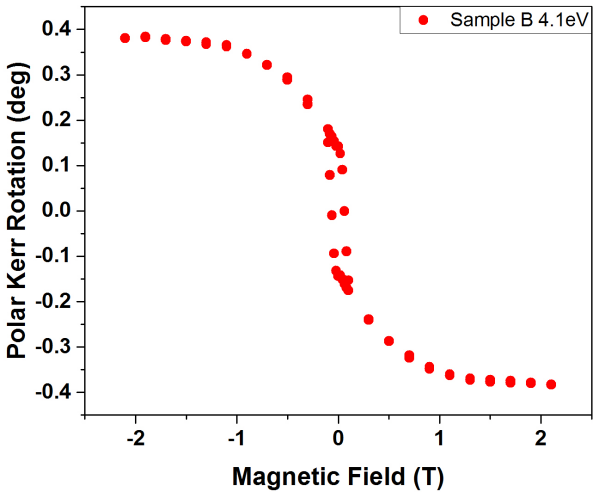

(b) Polar Kerr Hysteresis loop of Sample B at 4.1 eV

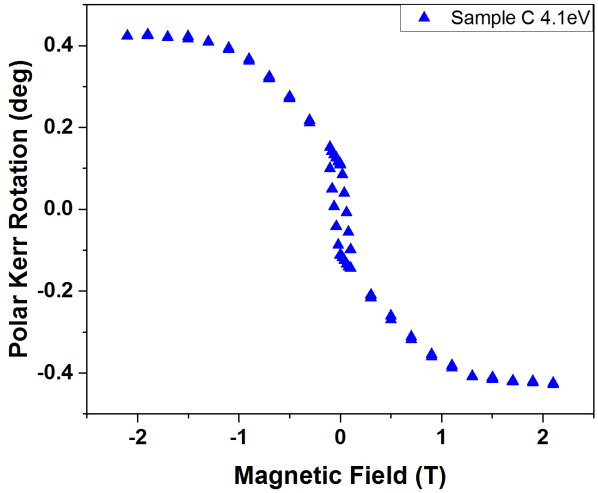

(c) Polar Kerr Hysteresis loop of Sample C at 4.1 eV

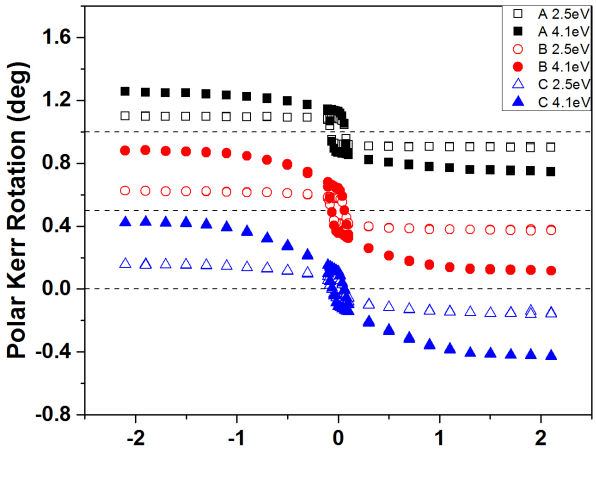

(d) All Hysteresis loops of samples A, B and C. The loops have been shifted along the y–axis for clarity.

Figure 4.12: Hysteresis loops of samples A–C at 4.1 eV

The curves are consecutively offset by 0.5 ° each along the y–axis for clarity. For all samples, the absolute Kerr rotation is larger at 4.1 eV compared to 2.5 eV which is partly due to a larger Kerr rotation of Co at this energy. However, this alone would not lead to a different saturation behaviour of the whole sample.

An explanation of this can be given by the following: The (polar) Kerr rotation is proportional to the magnetisation and the joint density of states of initial and final states involved in the transitions induced by the incoming photon [82]. Therefore, the different shape of the hysteresis loops at higher energies can be attributed to different electronic contributions. In this case, the additional contribution comes from EuS. The reason why the contribution is observed at higher energies is found in the enhancement effect present in EuS/Co systems [59]. In fact, the change of saturation behaviour and shape of the hysteresis loop can be explained by the presence (and visibility) of an additional EuS Kerr signal at higher energies.
In order to disentangle the two contributions of EuS and Co to the observed Kerr rotation, the following model is proposed.
The measured Kerr rotations θ_K are given by the following relations:

$$\theta_{K,2.5eV} = \theta_{K,Co,2.5eV} + \theta_{K,EuS,2.5eV} \approx \theta_{K,Co,2.5eV} \tag{4.3}$$

$$\theta_{K,4.1eV} = \theta_{K,Co,4.1eV} + \theta_{K,EuS,4.1eV} \tag{4.4}$$

$$\theta_{K,Co,4.1eV} = \alpha \cdot \theta_{K,Co,2.5eV} \tag{4.5}$$

Where $\theta_{K,2.5eV}$ and $\theta_{K,4.1eV}$ are the measured Kerr rotations at 2.5 and 4.1 eV respectively. The subscripts Co and EuS denote the individual contributions of both to the rotation and α is the quotient of $\frac{\theta_{K,Co,4.1eV}}{\theta_{K,Co,2.5eV}}$. Rearranging equation 4.4 gives:

$$\theta_{K,EuS,4.1eV} = \theta_{K,4.1eV} - \alpha \cdot \theta_{K,Co,2.5eV} \tag{4.6}$$

A suitable value for α can be extracted from the Kerr spectra of the three samples shown in figure 4.13.

The Kerr rotation measured with applied magnetic field is largest (absolute value) for sample C (largest Co thickness) and decreases to B and A (smallest Co thickness). The Kerr rotation for sample C is always larger than B and B is larger than A up to an energy of 4.5 eV, where the values are very close to each other. The largest contribution to the Kerr rotation in these spectra comes from Co. Some additional contribution of the Co/Pd magnetic substrate can not be entirely excluded. However, as shown in figure 4.10 it is possible to find a factor for Co/Pd layers that will align the spectra measured in remanence and with magnetic field and thus shows that there is no additional Pd or Co contribution at higher energies.
The spectra recorded at zero magnetic field show the opposite trend. Now sample C shows the smallest signal which can be explained by the thickness of the Co layer in the sample and the low amount of squareness (45%). Samples A and B show similar values in the en-

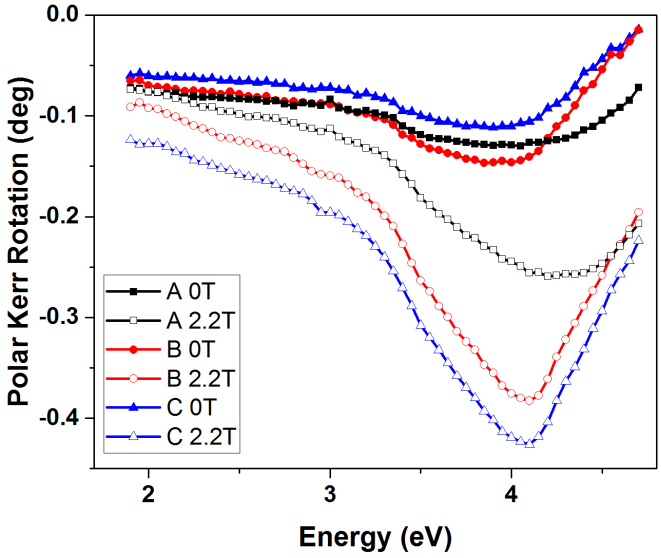

Figure 4.13: Polar Kerr spectra of samples A–C recorded in remanence and with applied magnetic field of 2.2 T at 300 K.

ergy range between 1.9 and 3.2 eV and differ afterwards. The remanence Kerr rotation for B is larger than that of A between 3.2 and 4.2 eV and smaller for higher energies. For sample A, the spectra at remanence and at 2.2 T do not differ significantly in the low–energy range (1.9 - 2.1 eV). This is due to the very high degree of PMA found in this sample. At energies larger than 2.1 eV, the two spectra start to differ though the difference at 2.5 eV is still small, in accordance with equation 4.3. At higher energies between 4.1 and 4.3 eV, there is a pronounced negative peak in the spectra for all samples recorded at 2.2 T that can be attributed to the magneto–optical enhancement effect. In remanence, the peak is less pronounced. The peak positions for samples B and C are located at the same energy but differ from sample A where the peak is also less distinct and shows a blue shift.

The reason why the peak of sample A is shifted is not entirely clear but might be explained by one or all of the following. The magneto–optic enhancement effect at the Co/EuS interface is very sensitive to the local properties of the interface. It is not only influenced by the single Co/EuS interface but also by the number and thickness of the multilayer constituents. In previous work about EuS/Co multilayers on magnetic substrates with perpendicular magnetic anisotropy, a peak position of 3.5 eV was found for samples with a similar Co thickness of 3 nm and a EuS thickness of 8 nm [24]. Generally, a thicker EuS layer produces a red shift of the observed peak.
Furthermore, the width of the peak will depend on the quality of the multilayers and interfaces. As has been reported for similar multilayers, the quality of growth decreases with the number of layer repetitions. It cannot be excluded that sample A, which has the highest number of repetitions, has a slightly worse interface quality as compared to

samples B and C (same number of repetitions), resulting in a less pronounced peak. In the case of samples B and C, the two spectra do not coincide at low energies. This is because both samples show less than 100% PMA which means that part of the magnetic moment in these samples will lie in plane when the external magnetic field is switched off, which in turn leads to a smaller Kerr signal at remanence.
With the help of two assumptions, it is possible to extract a value for α:

a) At remanence Co and EuS are antiferromagnetically exchange coupled and their magnetic moments are opposite.
b) A magnetic field of 2.2 T is enough to break the exchange coupling between Co and EuS, which will lead to a parallel alignment of their magnetic moments.

With these two assumptions the following equations can be written:

$$\theta_{K,rem} = \theta_{K,Co} - \theta_{K,EuS} \tag{4.7}$$

$$\theta_{K,2.2T} = \theta_{K,Co} + \theta_{K,EuS} \tag{4.8}$$

As evident from the two spectra of sample A, below an energy of 1.9 eV there is no difference between remanence and field spectra. This suggests, that the EuS Kerr signal is too small to be detectable in the low–energy–range and only the Co (and Co/Pd) contribution remains for lower energies.
Because samples B and C have a smaller amount of squareness because of their thicker Co layers, there is always a difference between the two spectra. However, even for those samples, there will be a point from which on there will be no detectable EuS contribution. Theoretically, this will happen below the bandgap of EuS (1.65 eV). As a first approximation, the recorded values at lowest energy are taken to show no EuS contribution and can thus be aligned by a suitable factor for samples B and C. This factor F will be given by:

$$F_{B/C} = \frac{\theta_{K,B/C,1.9eV,2.2T}}{\theta_{K,B/C,1.9eV,rem}}. \tag{4.9}$$

For sample A, F is equal to 1. Combining $F_{B/C}$ and equations 4.7 and 4.8 one can calculate the 'pure' Co (Co/Pd) and EuS contributions to the spectra by:

$$\theta_{K,Co} = \frac{1}{2} \cdot (F_{A/B/C} \cdot \theta_{K,A/B/C,rem} + \theta_{K,A/B/C,2.2T}) \tag{4.10}$$

$$\theta_{K,EuS} = \frac{1}{2} \cdot (F_{A/B/C} \cdot \theta_{K,A/B/C,rem} - \theta_{K,A/B/C,2.2T}) \tag{4.11}$$

The calculated spectra of each contribution are shown in figure 4.14.

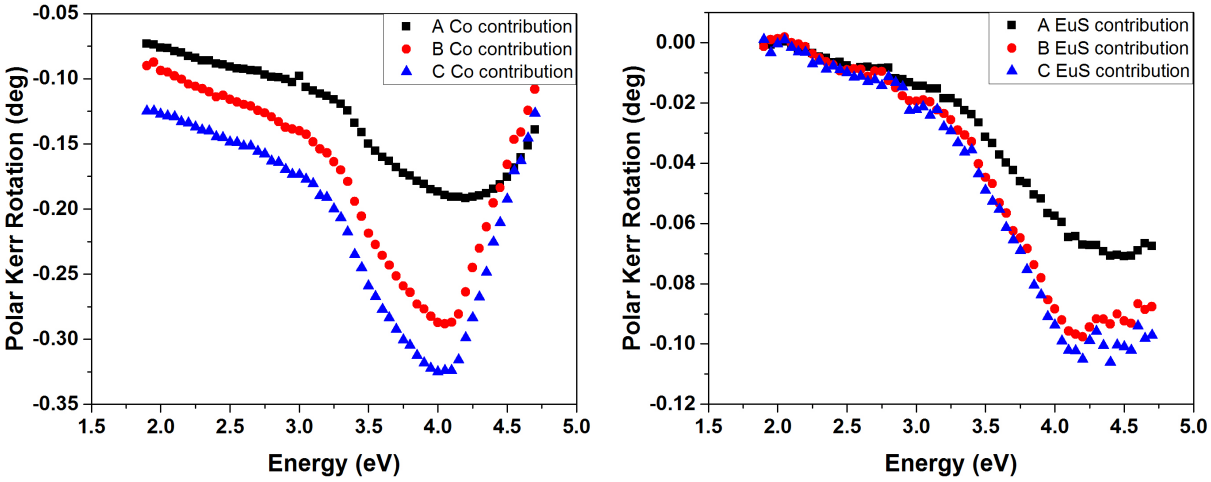

(a) Calculated Co contribution. (b) Calculated EuS contribution.

Figure 4.14: Calculated Co and EuS contributions to the polar Kerr rotation of samples D–F. (a) Co contribution, (b) EuS contribution.

From the 'pure' Co (Co/Pd) spectrum α (see equation 4.6) can now be calculated for each sample by

$$\alpha = \frac{\theta_{K,Co,4.1eV}}{\theta_{K,Co,2.5eV}}. \tag{4.12}$$

The EuS hysteresis loops at 4.1 eV were now calculated in accordance with equation 4.6 for all samples. The results are shown in figure 4.15. For better clarity, samples A and B have been shifted along the y-axis by 0.4° and 0.2° respectively.

Arrows indicate the direction of magneto–optic signal reversal for each hysteresis loop. In the case of sample A, the polar Kerr signal is saturated above 1.3 T reaching a value between $-0.04°$ and $-0.05°$. Decreasing the magnetic field to zero increases (decreases the absolute value) the EuS signal (zero crossing at around 0.5 T) to 0.05° at remanence. The signal stays constant until approximately -100 mT where it flips abruptly to $-0.05°$ in agreement with the observed flipping of the entire Co/EuS signal, after which it increases with increasing magnetic field (zero crossing at -0.5 T) until it saturates between 0.04° and 0.05°.

The hysteresis loop is symmetric and shows clear evidence of antiferromagnetic coupling. Because the PMA of sample A is very high, the absolute EuS signal at remanence and at maximum field is nearly the same. The opposite sign of the polar Kerr rotation at high magnetic field and at remanence points to a rotation of the EuS magnetic moment from antiparallel alignment at remanence to (fully) parallel alignment with the Co magnetic moment at a magnetic field of 1.3 T and beyond. For samples B and C, the hysteresis loops have a similar shape. The sign of the Kerr rotation at remanence (positive) and

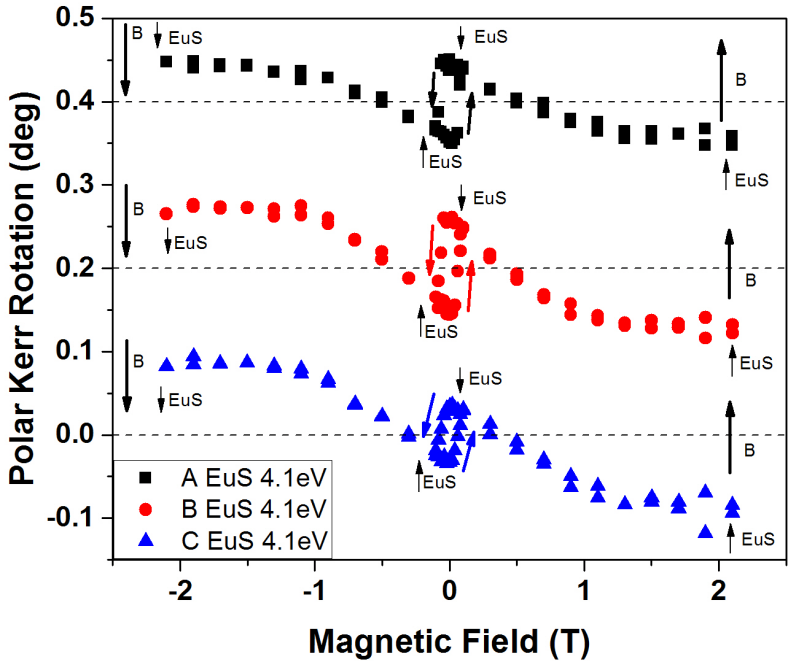

Figure 4.15: Calculated EuS hysteresis loops at 4.1 eV for samples A–C. Arrows indicate the orientation of EuS magnetic moments relative to the external magnetic field. Additional arrows show the direction of external magnetic field during the hysteresis cycle.

under maximum applied field (negative) also gives evidence of an antiferromagnetic alignment between Co and EuS magnetic moments.
The absolute values of the polar Kerr rotation at remanence and in maximum applied field are not the same for samples B and C because for these samples the degree of PMA is less than 100%, meaning that at remanence part of the EuS magnetic moment is no longer oriented out of plane and does not contribute to the polar Kerr rotation. In maximum magnetic field however, all the magnetic moments have been rotated out of plane and contribute to an overall larger signal compared to remanence. The absolute maximum value of the polar Kerr rotation of EuS at 4.1 eV is increasing from sample A (0.05°) to sample C (0.08°) which could be due to either a stronger coupling due to increasing Co thickness in the Co/EuS bilayers (in case of an interface coupling effect) or increasing the EuS thickness in the bilayers in the samples (double for samples B and C compared to A) if the Co–induced polarisation of the EuS layers extends significantly into the interior.

In the following, the procedure to extract the EuS contribution to the Kerr rotation and the assumptions will be discussed again in view of possible errors or misinterpretations. As shown before, there is no clear evidence of any antiferromagnetic coupling in the hysteresis loops recorded at 2.5 eV, it was assumed that the EuS signal is negligible and that the recorded hysteresis loops at 2.5 eV show predominantly the Co Kerr rotation. However, a closer look at the recorded spectra in remanence and under applied field

reveals that, although the difference between the two spectra is negligible for energies from 1.9 - 2.1 eV, there is a small difference at 2.5 eV. The deviation of the 'pure' Co signal at 2.5 eV (calculated as shown above) from the one in the Kerr hysteresis loop at 2.5 eV amounts from about 7% (sample C) to about 15% (sample A). For this reason, the calculated factors from the 'pure' Co spectrum linking 2.5 and 4.1 eV, which were used to calculate the EuS signal at 4.1 eV, were altered in order to check how reliable the calculated signal was.

The calculated α values were 2.1 (1.8 - 2.4) for sample A, 2.5 (2.0 - 4.0) for sample B and 2.2 (1.8 - 3.5) for sample C (values given in brackets are the tested range for which similar hysteresis loops to the ones shown in figure 4.15 were obtained). The factors tested exceed the uncertainty range of up to 15% error in the Co 2.5 eV hysteresis loops and make the calculated EuS Kerr rotation at 4.1 eV and the conclusion of the presence of antiferromagnetic exchange coupling robust. Another source of error could be the misinterpretation of the additional signal in the hysteresis loops recorded at 4.1 eV as ferromagnetic instead of paramagnetic EuS signal. A paramagnetic signal would also be optically enhanced by the enhancement effect mentioned earlier. One can assume only paramagnetic response from EuS in the 4.1 eV hysteresis loops and chose a different factor β linking the hysteresis loops at 2.5 and 4.1 eV so that the Kerr rotation goes to zero for zero magnetic field when both hysteresis loops are subtracted from each other. The factors for which this happens are 1.5 (A), 1.77 (B) and 1.66 (C). The so calculated hysteresis loops showing 'paramagnetic' EuS contribution at 4.1 eV were averaged (decreasing and increasing magnetic field summed).

Paramagnets can be described by the Brillouin function [83]:

$$B_J(x) = \frac{2J+1}{2J} coth(\frac{(2J+1)x}{2J}) - \frac{1}{2J} coth(\frac{x}{2J}), \tag{4.13}$$

where $x = \frac{g\mu_B JB}{k_B T}$ is a variable comprising the Landé factor g, the magnetic moment μ_B, the magnetic field B, the temperature T, Boltzmann constant k_B and the total angular momentum J.

Fitting the calculated 'paramagnetic' EuS signal at 4.1 eV with the Brillouin function gave J values between 530 and 760 (figure 4.16). Values this high can only occur when one treats nanoparticles as magnetic entities in superparamagnetism, which is not the case here, as confirmed by the quality of the growth of such multilayers in section 4.2.1. In fact, paramagnetic EuS with 7 μ_B and $T_C = 16.5\ K$ would give a straight line and not saturate for the magnetic field range applied in this experiment. In contrast, the hysteresis loops obtained for the supposed paramagnetic EuS signal show saturation above 1.5 T (figure 4.16). In light of the very high values for J found from the Brillouin–fits a paramagnetic EuS signal at 4.1 eV is doutbful. It is at least due to EuS with considerably higher T_C than the bulk value of 16.5 K.

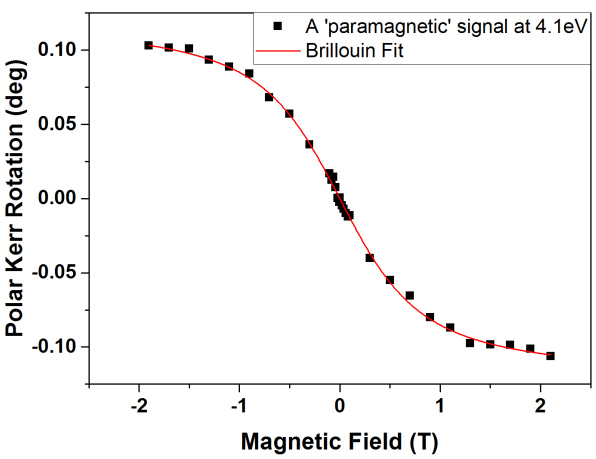

(a) Brillouin Fit of Sample A

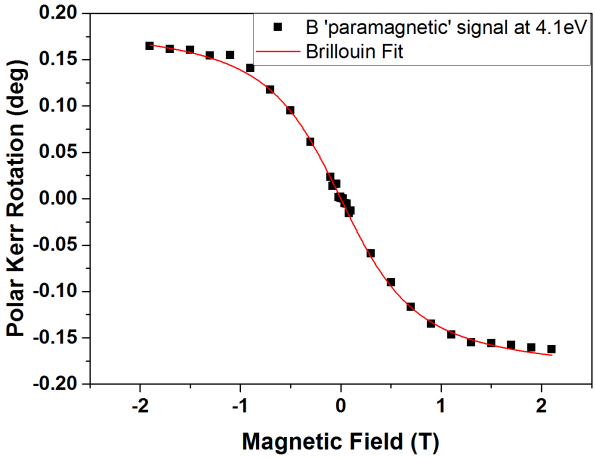

(b) Brillouin Fit of Sample B

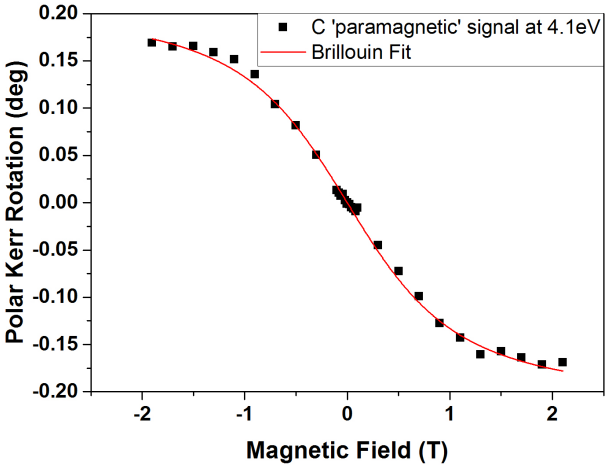

(c) Brillouin Fit of Sample C

Figure 4.16: Brillouin Fits of samples A–C

Samples D–F

After the initial samples A–C and the detection of antiferromagnetically coupled EuS signal at RT, a second series of samples, D–F, was prepared. This time, the number of layer repetitions on top of the magnetic substrate was fixed to 3 and the individual EuS thickness fixed to 10 $\mathring{A}$. The Co thickness in the multilayer was kept at the same values as in samples A–C, i.e. between 10 and 20 $\mathring{A}$. The results of samples D–F will be shown and discussed in the same manner as samples A–C. Table 4.2 shows the structure of the second samples.
New magnetic substrates were produced for samples D–F, which seem to have an increased Co thickness and therefore show less squareness as the original MS(6). The new magnetic substrates will be indicated by MS(6)*.

sample name	Substrate	Structure (Å)
D	MS(6)*	$[Co(10)/EuS(10)]_3$
E	MS(6)*	$[Co(15)/EuS(10)]_3$
F	MS(6)*	$[Co(20)/EuS(10)]_3$

Table 4.2: EuS/Co multilayers prepared on MS(6)* with varying Co and constant EuS thickness. Thickness is given in Å.

The energy spectra were recorded with magnetic field and in remanence between energies of 0.8 eV and 5.4 eV and are shown in figure 4.17. Below the band gap of EuS, it is magneto–optically transparent and should contribute minimally to the Kerr rotation measured at in this energy range. This way, it is possible to measure only the Co contribution to the sample Kerr rotations. The additional influence of EuS was minimal at energies around 2.5 eV for samples A–C, however, measurements below the bandgap would help to exclude the EuS signal entirely. Therefore, the spectra were also recorded in the energy range between 0.8 eV and 1.2 eV.
The spectra at maximum magnetic field show that sample F, which has the largest amount of Co, has the largest absolute Kerr rotation. Sample D, with the lowest amount of Co shows the smallest Kerr rotation, while the spectrum of sample E is found between D and F. The remanence measurements reveal, that none of the samples show 100% PMA. The squareness, defined in equation 4.2, of each sample was calculated from hysteresis loops recorded at 0.85 eV (see figure 4.18). D has a squareness of 50%, E one of 67% and F one of 27%. The value of sample E is comparable to the one of sample B (65%), although E has one more repetition. The value of F is lower compared to sample C (45%) because of the additional layer of thicker Co (3 compared to only 2 in sample C). The low value of D is quite surprising, given that it has the same number of repetitions and Co thickness as sample A, which showed a very high degree of squareness of 85%. The most likely reason for this is due to a higher amount of Co in D.

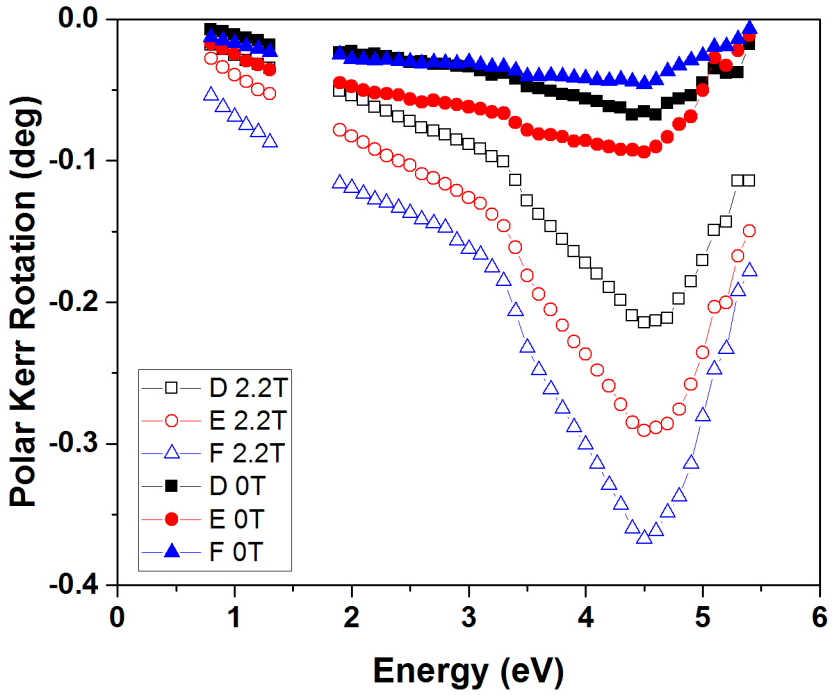

Figure 4.17: Polar MOKE spectra of Samples D–F

Sample E shows the largest signal in remanence. Samples D and F show largely the same signal between 0.8 eV and 3.0 eV and start to differ above 3.0 eV, where D has a larger Kerr rotation. The spectral response below 3 eV can be explained like this: D has half the amount of Co compared to F but contributes with 50% of its magnetic moment to the Kerr rotation, whereas F only contributes with 27%, which essentially makes both signals equal. The contribution of EuS is minimal in this energy range (at RT, as was the case for samples A–C) and hence, the the difference between D and F at remanence starts to arise when the EuS contribution is enhanced above 3 eV.

The spectra in figure 4.17 show a maximum Kerr rotation at 4.5 eV, where a 'dip' is seen. This dip corresponds to the maximum of the enhancement and is blue shifted by 0.4 eV compared with samples A–C. The reason for this shift is the smaller EuS thickness found in samples D–F. The absolut values of the Kerr rotation measured at maximum field and in remanence are smaller than the ones found for samples A–C, despite the fact that samples D–F contain more Co, which has the largest contribution to the spectra, than A–C. Again, the influence of the underlying magnetic substrate on the spectra cannot be excluded from the shape of the spectra (see section 4.2.3).

Hysteresis loops were recorded for energies of 0.85 eV, 2.5 eV and 4.4 eV for each sample and are shown in figure 4.18.

The EuS Kerr rotation, which is more prominent around 4.5 eV is extracted by the same procedure as discussed in section 4.2.3. The extracted Co and EuS contributions to the spectra are shown in figure 4.19.

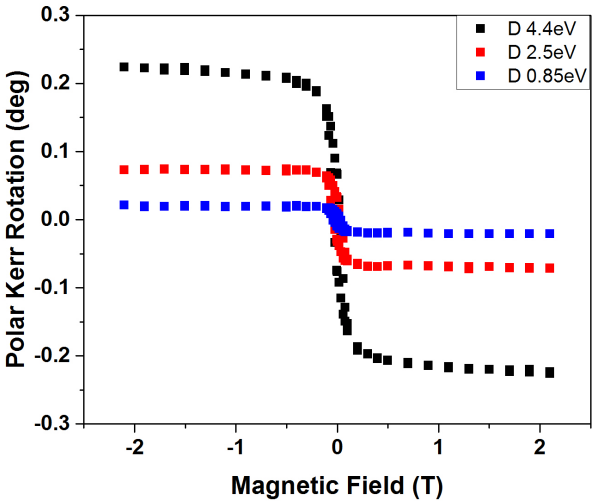

(a) Polar Kerr Hysteresis Loop of sample D

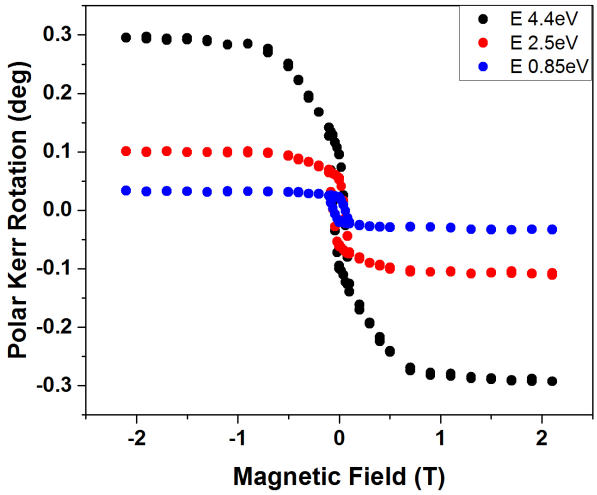

(b) Polar Kerr Hysteresis Loop of sample E

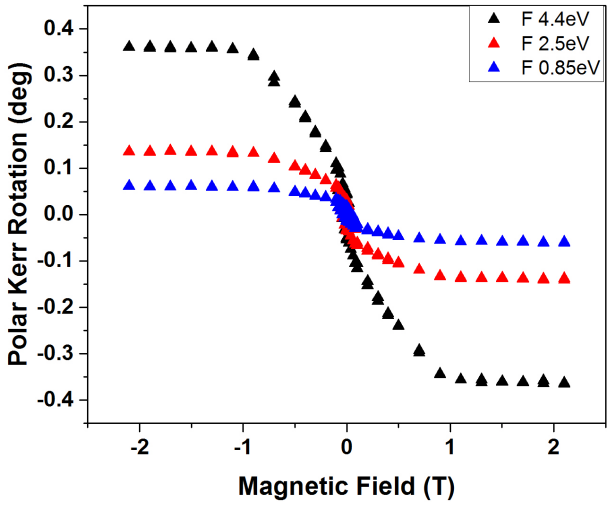

(c) Polar Kerr Hysteresis Loop of sample F

Figure 4.18: Polar Kerr Hysteresis Loop of samples D–F

The calculated contributions show a similar spectral shape and have similar values to the ones found in samples A–C. The estimated Co contribution is smaller in samples D–F, which is interesting, since in one sample (D), the overall amount of Co is the same and for two samples the amount is larger than the Co amounts in samples A–C (see tables 4.1 and 4.2).

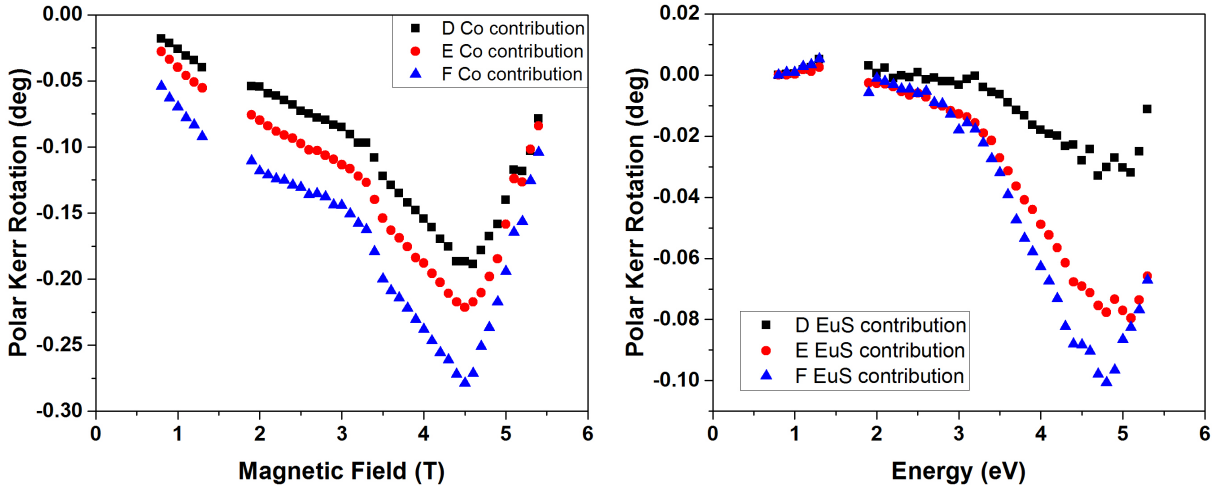

(a) Calculated Co contribution.

(b) Calculated EuS contribution.

Figure 4.19: Calculated Co and EuS contributions to the polar Kerr rotation of samples D–F. (a) Co contribution, (b) EuS contribution.

The EuS hysteresis loops at 4.4 eV were calculated in the same manner as shown for samples A–C and show similar results (figure 4.20). For clarity, the results of samples D and E have been offset along the y–axis by 0.4 and 0.2° respectively. The calculated hysteresis loops show the antiparallel alignment of EuS and Co magnetic moments in the system. The EuS Kerr rotation at positive remanence is positive at first and then rotated to negative values with increasing magnetic field. This is found in all samples. Over the course of the hysteresis the shape is symmetric and at the coercive field (around 50 mT), the entire signal flips. Negative fields lead to positive Kerr rotations.
Sample D shows a small residual gradient for the entire measurement range and does not seem to saturate. Sample E however, shows about the same absolut values in remanence as under maximum magnetic field (the small kink between 1.3 and 1.7 T is due to a measurement effect and does not appear between -1.3 and -1.7 T). Sample F shows similarities to the calculated EuS hysteresis of sample C as both show the smallest amount of squareness. F shows a smaller Kerr rotation at remanence and the highest one for applied magnetic fields above 1 T, where the Kerr rotation is saturated. As most of the magnetisation of this sample lies in plane and has to be rotated out by the external field, this observation makes sense.

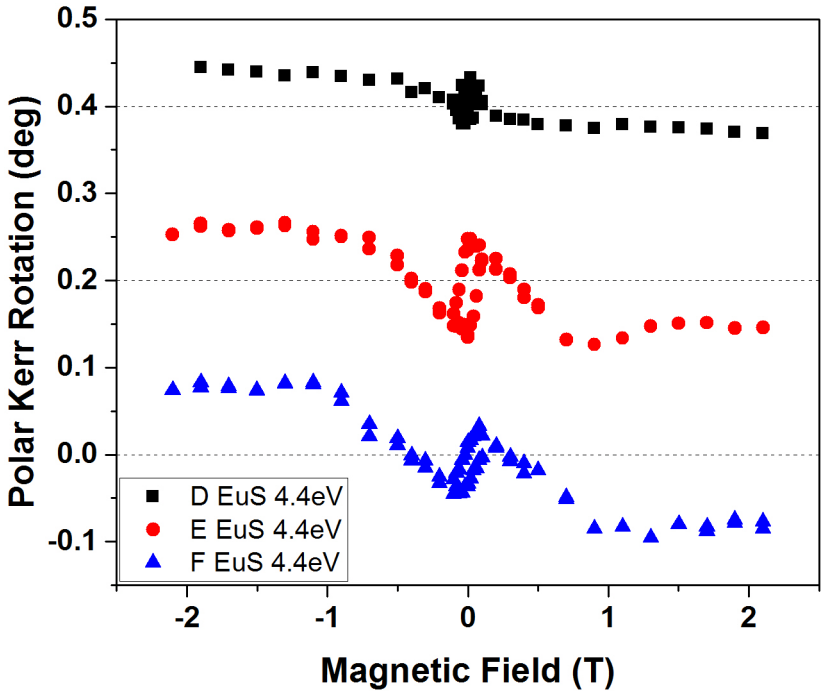

Figure 4.20: Calculated EuS hysteresis loops for samples D–F at 4.4 eV

The overall Kerr rotations and the calculated spectral Co contribution are smaller for samples D–F than in samples A–C, while the calculated EuS contribution and general shape of the EuS hysteresis loops seems unchanged. From experimental measurements and estimations it is speculated that the coupling strength between Co and EuS layers is inversely proportional to the EuS thickness [71, 84]. Accordingly, the coupling strength in samples D–F should have increased compared to samples A–C. However, if the coupling effect is limited to the interface and only the first few atomic layers of EuS are involved, the observation of the effect would not necessarily depend on the EuS thickness beyond a certain point, i.e. the maximum number of coupled layers. This might be one reason, why the antiferromagnetic coupling of EuS can be extracted at high energies, using the known magneto–optic enhancement effect between Co and EuS interfaces, in all samples. The actual contribution might then be the same due to the limited range of the coupling. Essentially, a second reason might also explain the smaller Kerr rotations measured in D–F and the subsequent evaluation of the Co and EuS contributions.

The model proposed for calculating the Co and EuS contributions to the spectra from the remanence and applied field spectra essentially supposes a fully parallel and antiparallel alignment of the Co and EuS magnetisations for both cases.

For zero external magnetic field this assumption seems reasonable because of the antiferromagnetic coupling between both materials (even at RT as known from XMCD measurements of similar EuS/Co layers). While the assumption that the antiferromagnetic coupling can be broken at RT also seems reasonable, the real alignment between

both magnetisation vectors at 2.2 T remains speculative. In reality, both magnetisation directions might be misaligned (out of plane) by an angle β under applied field. This would change equation 4.8 to:

$$\theta_{K,2.2T} = \theta_{K,Co} + cos(\beta) \cdot \theta_{K,EuS} \tag{4.14}$$

The term $cos(\beta)$ describes how much of the EuS magnetisation has been aligned parallel to the Co magnetisation. The value of β is unknown and remains up to speculation. The element specific hysteresis loops of sample S26, which had a EuS thickness of 2 nm in each layer, showed that at 2.5 K and 5 T about 40% of the magnetisation were aligned parallel to Co. At RT only moderate magnetic fields up to 600 mT were applied and no breaking of the coupling was found. If the coupling between EuS and Co is indeed stronger for thinner EuS layer, and both Kerr rotations would cancel each other in remanence, the remanence signal for samples D–F would be smaller compared to samples A–C, which is indeed observed in the Kerr spectra shown in figure 4.17. For 2.2 T the alignment would then not be parallel and the EuS contribution (this time adding to the measured Kerr rotation) smaller than in samples A–C because some part of the EuS magnetisation would not be rotated out of plane and thus not contribute to the Kerr rotation. This would explain the smaller Kerr rotation of the samples D–F for maximum magnetic fields.
In the calculation of the individual element contributions, $cos(\beta)$ leads to an increase of the Co rotation and gives a smaller EuS contribution ($cos(\beta) \cdot \theta_{K,EuS}$). Because the value of β is unknown, no further estimates are made for the Co and EuS contributions of samples D–F including the term $cos(\beta)$.

Regardless of the model used for the calculation of of the individual Co and EuS Kerr contributions, the general conclusion drawn from the polar MOKE measurements, i.e. the observation of the antiferromagnetically coupled EuS in the polar Kerr spectra and hysteresis loops at high energies, remain the same and only the individual values change according to the model used for the calculation of the individual element contributions.

4.3 Analysis of EuS/Ni multilayers

This section will deal with various EuS/Ni multilayers and their structural and experimental characterization. The results regarding growth quality, Eu–spin–polarisation by Ni and magneto–optical–Kerr–measurements will be discussed and compared to EuS/Co multilayers.
Magnetic characterization was performed on selected samples via Superconducting Quantum Interference Device (SQUID) magnetometry at a temperature of $T = 5\ K$ under a maximum field of 30 kOe applied in the film plane. The contribution of the diamagnetic background, coming from the Si(001) wafer when one performs in-plane measurements was measured and removed.
The different samples discussed in this section are shown in table 4.3.

sample name	Substrate	Structure (Å)
S21	Si/SiO_x	$[EuS(40)/Ni(40)]_4 + EuS(40)$
S22	Si/SiO_x	$[EuS(40)/Ni(65)]_4 + EuS(40)$
S23	Si/SiO_x	$[Ni(60)/EuS(40)]_9 + Ni(60)$
S24	Si/SiO_x	$[Ni(70)/EuS(20)]_9 + Ni(70)$
S28	Si/SiO_x	$[Ni(80)/EuS(20)]_9 + Ni(80)$
S29	$GaAs/AlGaAs/AlO_x$	$[Ni(80)/EuS(20)]_9 + Ni(80)$
S30	Si/SiO_x	$[Co(60)/EuS(20)]_9$
S31	$GaAs/AlGaAs/AlO_x$	$[Co(60)/EuS(20)]_9$
S37	Si/SiO_x	$[Ni(80)/EuS(20)]_{30} + Ni(80)$
N-C-EuS-1	Si/SiO_x	$[Ni(40)/Co(5)/EuS(40)/Co(5)]_6 + Ni(40)$
S38	Si/SiO_x	$[Ni(80)/Co(3)/EuS(20)/Co(3)]_{20} + Ni(80)$

Table 4.3: EuS/Ni multilayers grown on different substrates at room temperature. Thickness in brackets is given in Å.

The table shows a number of samples with different number of layer repetitions and individual layer thickness of each element. While generally, the numbering of the samples is consecutive, the ordering in the table is not. Instead, it aims to represent the evolution and thought process behind each sample, taking into account the information gathered from measurements of the previous samples. A brief summary is given here, before each of the results are discussed in more detail.
Initially, the samples S21, S22, S23 and S24 were produced in order to characterize the growth of EuS/Ni multilayers and their magnetic properties. S29 and S31 were produced on a GaAs/AlGaAs substrate containing an epitaxial thin layer of about 1 nm of AlO_x functioning as a tunnel barrier. This was done as a first step for the incorporation of EuS multilayers on spin–LEDs, the results of which will be discussed in more detail in chapter 5.
S37 and S38 both contain a higher number of repetitions, to make X–Ray Magnetic

Scattering (XRMS) possible. XRMS measures the asymmetry ratio of right– and left–circularly polarised x–rays at each Bragg–peak of a multilayer sample, which in turn is a measure of the magnetic moment distribution within the layers. In order to achieve a higher number of observable Bragg–peaks, the repetitions in both samples are increased. Additionally, S38 includes approximately one atomic layer of Co at each EuS–Ni–interface. This was done with the aim to take advantage of the improved growth of EuS/Ni layers compared with EuS/Co layers, while taking advantage of the higher spin–polarisation in Eu induce by Co compared to Ni. The sample N-C-EuS-1 was produced as a first test for this idea.

4.3.1 Growth of EuS/Ni multilayers

Figure 4.21 shows the x–ray–reflectivity measurement of S22. The inset shows a magnification, revealing four clear Bragg–peaks, that point to a high multilayer quality. The additional presence of Kiessig fringes, resulting from the interference of the x–rays reflected from the surface with those reflected from the substrate, indicates a negligible surface roughness and high coherence through the whole structure.
Compared to the XRR patterns of similar EuS/Ni multilayers shown in the previous section, one notices the larger number of Bragg peaks and the clearly defined Kiessig fringes. Both point to a superior multilayer quality for the EuS/Ni system.
The relative position of two successive Kiessig fringes (or Bragg peaks) enables one to accurately determine the total film (or multilayer period) thickness according to the following equation [85]:

$$2 \cdot \Lambda \cdot sin(\theta_n - \theta_{n-1}) = \lambda \tag{4.15}$$

where Λ is the multilayer repetition period and λ the wavelength. The Ni layers were found to be about $6-6.5\ nm$ and the EuS ones $4\ nm$ thick. These values are in good agreement with the values estimated by the quartz microbalance ($6\ nm$) during film growth.
TEM and High Resolution Transmission Electron Microscopy (HTEM) measurements of S21 and S24 are shown in figures 4.22 and 4.23 respectively. The overall thickness of S21 as measured is $36.4\ nm$ with a root–mean–square (rms) surface roughness of $1.8\ nm$. This value is almost half of the values reported for similar EuS/Fe and EuS/Co multilayers in other studies [70].
The multilayer growth is initiated by the formation of a layer of EuS on top of the natively formed SiO_x layer on the Si substrate. The initial Ni or EuS layers are of excellent quality, showing sharp interfaces and low interfacial roughness. The Ni layers comprise of nanocrystallites and have an average thickness of $3.8\ nm$, which increases towards the top of the film. Their interfacial rms roughness is $0.65\ nm$. The average layer thickness

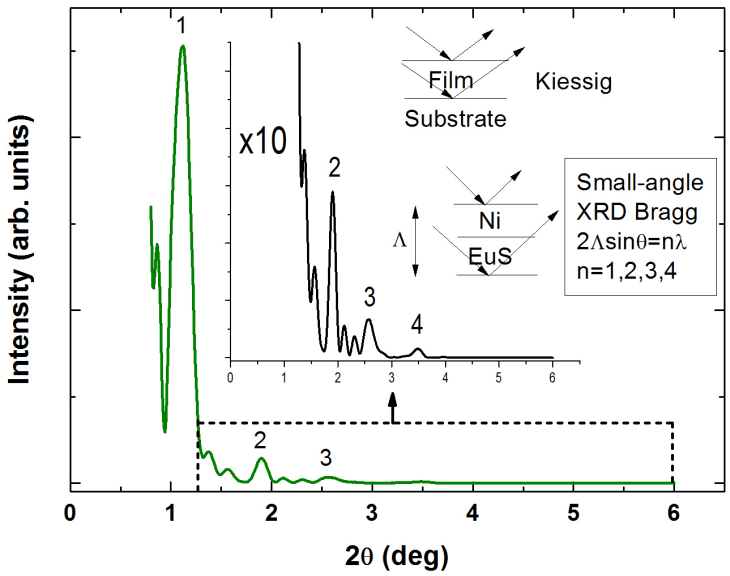

Figure 4.21: X–ray–reflectivity of sample S22. Four Bragg–peaks and additional Kiessig–fringes are present, indicating a high multilayer quality with negligible surface roughness.

of EuS is 4.1 nm. The smoother growth of EuS/Ni multilayers is probably due to the smaller surface energy of Ni as compared to Fe or Co, leading to better wetting of Ni on EuS [86].

The crystalline quality of the S21 multilayer was detected by Selected Area Diffraction (SAD) experiments and a representative pattern is shown in figure 4.22b. The ring pattern superimposed with the Si reflections of its [110] zone axis denotes the multicrystalline nature of the Ni and EuS layers. Furthermore, their reflections are solely attributed to the fcc Ni and fcc EuS phases. The individual Ni and EuS crystallites were also examined by HTEM experiments, as shown in figure 4.22c. The Ni grains predominately exhibited 111–type lattice fringes, with a spacing of $d = 0.203\ nm$, corresponding to their theoretical bulk value [83].

The EuS nanograins usually have an average lattice spacing of $d = 0.296\ nm$, which is 0.8% smaller than their bulk value [17] and can be assigned to the (200) planes of EuS. The same was also the case in EuS/Fe and EuS/Co multilayers as reported by Lewitz et al. [70]. No evidence of an additional Eu_3O_4 phases in the EuS layers was detected by the HTEM shown in figures 4.22 and 4.23.

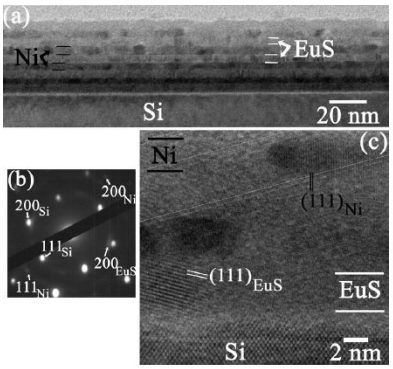

Figure 4.22: a) TEM of S21. Ni and EuS layers are indicated. b) Selected area diffraction (SAD) pattern of the multilayer and a part of the substrate, showing multicrystallinity of the Ni and EuS layers. c) HTEM image showing Ni and EuS nanograins.

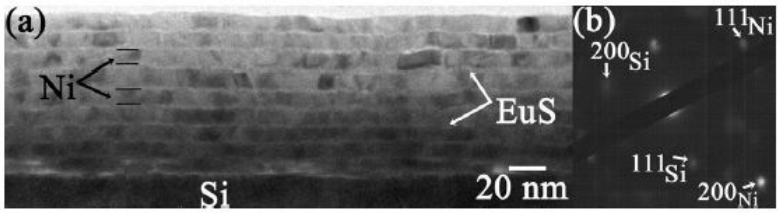

Figure 4.23: a) TEM of S24. Ni and EuS layers are indicated. b) Selected area diffraction (SAD) scan of the multilayer and a part of the substrate, showing multicrystallinity of the Ni layers. EuS is entirely amorphous in this sample.

Figure 4.23a shows a TEM image of S24 which has an overall thickness of 87.1 nm. In spite of the relatively large thickness, the average surface roughness is only about 2.3 nm. Again, growth of the multilayer is initiated by the formation of a layer of Ni on top of the natively formed SiO_x on the Si substrate. The Ni layers have an average thickness of 7.3 nm and an interface rms roughness of 1.1 nm. This particular piece of the Si wafer showed some intrinsic crystal defects, which influenced the thickness of the initial Ni layers but had no effect on the following layers. The overall multilayer growth was not affected by the Si defects.

The Ni layers again comprise of nanocrystallites with height equal to the layer thickness and a width of up to 20 nm. On the other hand, the EuS layers, sandwiched between the Ni layers, are thin (about 2.2 nm thick) and entirely amorphous. This is further supported by the SAD pattern of figure 4.23b. Amorphization of thin EuS layers with their thickness approaching 2 nm has been speculated from the shape of the UV–VIS light absorption spectra by Poulopoulos et al. [81].

Both samples do not show the presence of Eu^{3+}, which means, that all Eu ions should be fully magnetic below their T_C.

The magnetisation hysteresis loop at 5 K for S23 is shown in figure 4.24. The loop was recorded with a maximum field of 30 kOe to ensure complete magnetic saturation but is only presented up to 10 kOe for better clarity. Ni and EuS are fully magnetic at 5 K and the magnetisation is normalized to the total film volume. The calculation of the magnetisation loop (thick line) is based on a Stoner–Wohlfarth–like model [87]. The

best agreement between experiment and calculations was achieved when using a $\sim 5\%$ decreased value for Ni (480 $^{emu}/_{cm^3}$) and a $\sim 5\%$ decreased value of EuS (1140 $^{emu}/_{cm^3}$). These values are within the experimental accuracy of SQUID and volume determination. Besides the direct bilinear antiferromagnetic exchange coupling, which is known to hold between $3d$ and $4f$ magnetic atoms [34, 35] some biquadratic coupling was included in order to improve the fit of the experimental data. As concluded from the TEM measurements, indeed, all Eu ions are ferromagnetic and contribute to the magnetisation.
In contrast, Lewitz et al. found that calculating the experimental magnetisation loops for EuS/Co and EuS/Fe multilayers with the same model was only possible when a magnetisation value equal to half of the bulk EuS value was used [70]. This is due to the fact that only approximately half of the Eu was in the divalent state (which was observed by XAS) and, consequently, ferromagnetic. The fact that the magnetisation curve of S23 can be reproduced using almost the bulk values for Ni and EuS is further indirect evidence for the fact that a larger portion of Eu is in the divalent state in EuS/Ni multilayers.
The antiferromagnetic exchange constant value J_{AF}, determined by the calculation of S23 is 0.59 $^{erg}/_{cm^2}$,which is slightly larger than the ones reported by Lewitz et al. for EuS/Co (0.38 $^{erg}/_{cm^2}$) and EuS/Fe (0.45 $^{erg}/_{cm^2}$).

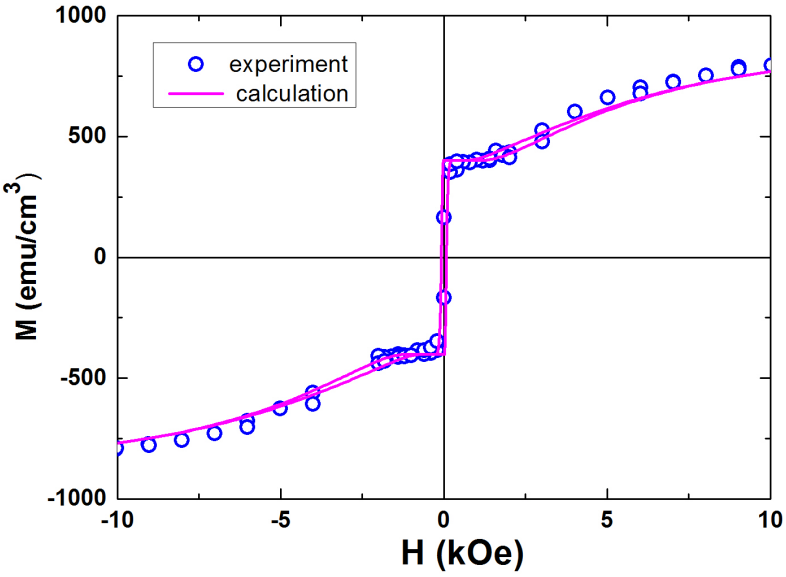

Figure 4.24: SQUID magnetisation loop of S23 recorded at 5 K.

To directly compare the multilayer quality of EuS/Ni and EuS/Co and identify a possible influence of the substrate in use, the samples S29 and S31 were grown on $GaAs/AlGaAs/AlO_x$ substrates.

The multilayer structure for S29 and S31 was simultaneously deposited on the GaAs–based substrates and standard Si wafers with native SiO_x. The two samples were grown on successive dates and their multilayer quality measured by x–ray–reflectivity. The results of the samples grown on the GaAs–based substrates are shown in figure 4.25.

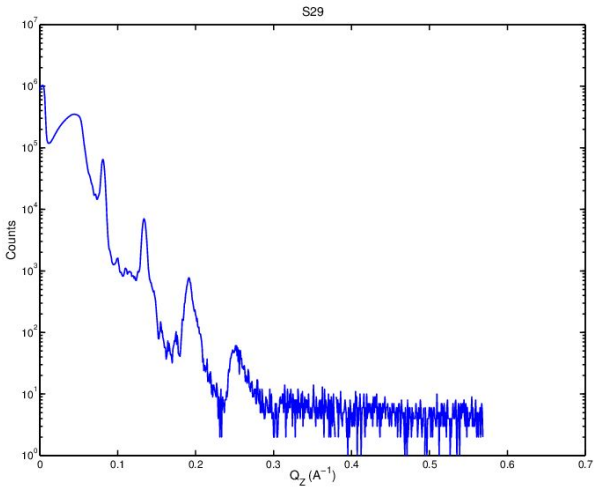

(a) X–Ray–Reflectivity measurement of S29 showing four Bragg–peaks.

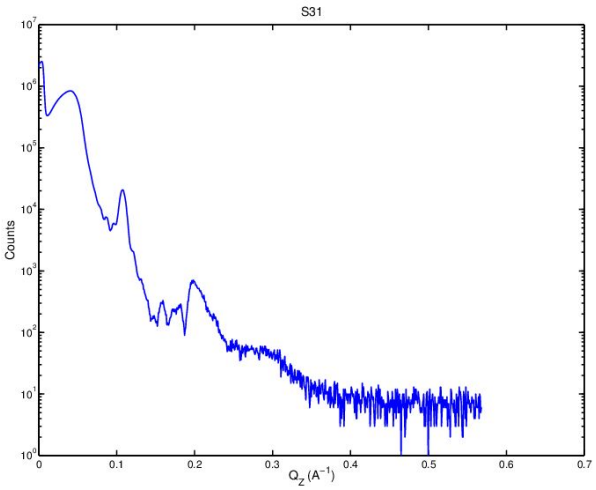

(b) X–Ray–Reflectivity measurement of S31 showing two Bragg–peaks.

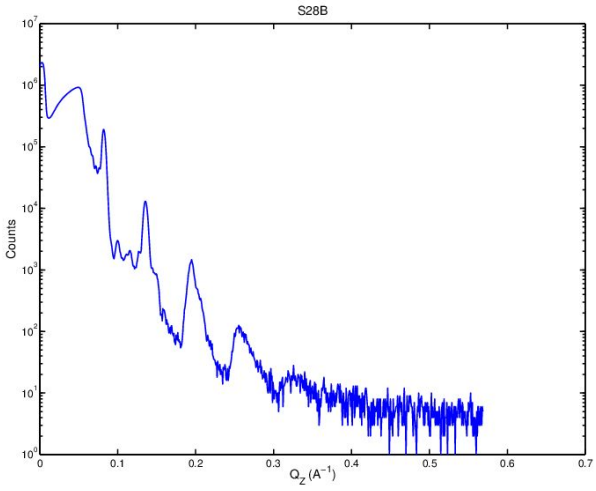

(c) X–Ray–Reflectivity measurement of S28 showing four Bragg–peaks.

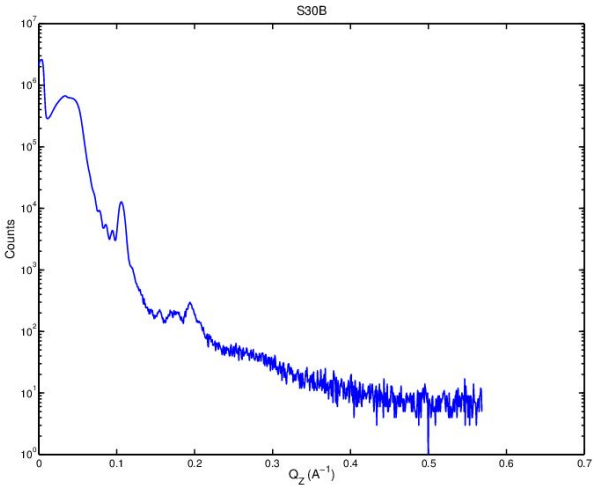

(d) X–Ray–Reflectivity measurement of S30 showing two Bragg–peaks.

Figure 4.25: XRR of samples S28–S31

For S29, four clear Bragg–peaks are observed, compared to only two for S31. The different substrate do not affect the multilayer quality. S28 and S29 show an equal number of Bragg–peaks which appear at the same positions. The same is true for S30 and S31. These results again corroborate the much smoother growth and reduced roughness within

EuS/Ni multilayers compared to EuS/Co ones.

4.3.2 XMCD of EuS/Ni multilayers

X–Ray–absorption spectra and XMCD signal at the Eu L_2-edge were recorded for some of the EuS/Ni samples. The measurements were performed again at the E.S.R.F.
Figure 4.26 shows the x–ray–absorption of S24 in the energy range around the Eu L_2-edge (thick black line) at RT. No absorption peak of Eu^{3+} is found in this sample. For comparison, the XAS of S26 is also plotted (dashed red line), where absorption peaks for divalent and trivalent Eu were found. For clarity, the absorption spectra have been offset on the y–axis by 1 unit.

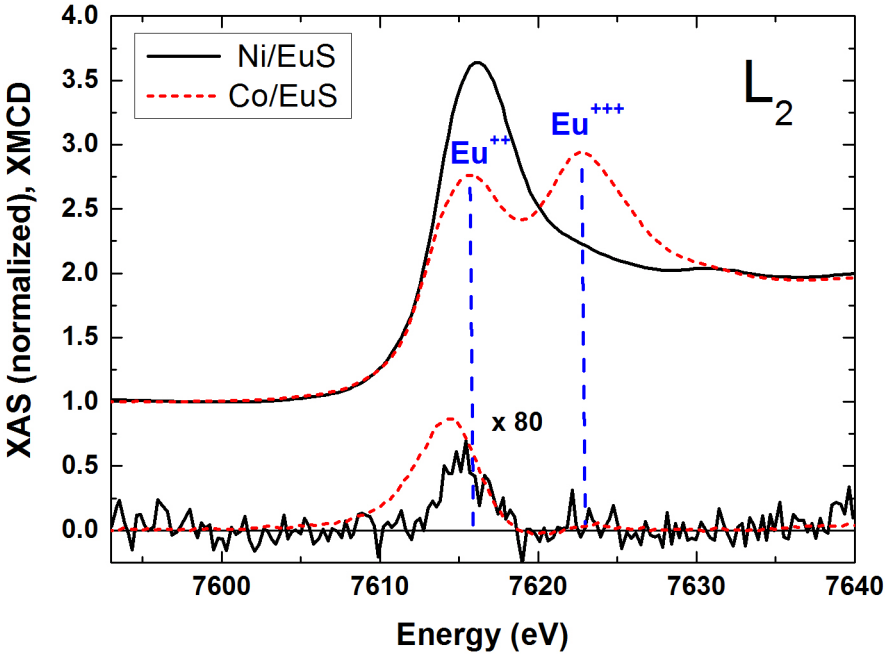

Figure 4.26: XAS and XMCD signal at the Eu L_2-edge of S24 at RT. For comparison S26 is also shown (dashed line). The x–ray–absorption–spectra are shifted along the y–axis for clarity. Both samples show RT spin–polarisation in Eu.

Both samples have a similar bilayer thickness of 2 nm EuS and 7 nm $3d$–metal each. The number of repetitions of S24 is lower (9) compared to S26 (15) however. The XAS measurement of S24 confirms the absence of Eu^{3+}, in agreement with the cross–section–TEM analysis on similar EuS/Ni layers.
Additionally, the XMCD signal for S24 and S26 is shown below the XAS. It has been multiplied by 80 for better clarity. Again, the XMCD signal is located entirely at the divalent absorption edge. The XMCD signal is also positive for both S24 and S26, meaning, that Eu is spin–polarised in both samples at RT. The signal however, is larger for S26 compared to S24 which means that the polarisation effect of Ni on Eu is smaller compared

to Co on Eu. This would result in a smaller magnetic moment per Eu ion. Equation 4.1 estimates a magnetic moment of 0.5 $\frac{\mu_B}{ion}$ for Eu in S26, which contained $\sim$ 45% divalent Eu. In S24 approximately all Eu atoms are in the divalent state, while the integrated XMCD signal (proportional to the magnetic moment of Eu) of S24 is about half of S26. This gives a polarisation that is approximately 4.4 times weaker in EuS/Ni multilayers. This results in an average magnetic moment of 0.11 μ_B per Eu ion in S24.
The result is reasonable: Pt acquires a maximum induced magnetic moment 2–3 times smaller in Ni/Pt multilayers than in similar Co/Pt ones.
Finally, there are energy shifts of $0.5 - 1$ eV at the Eu peaks in both XAS and XMCD spectra between S24 and S26. These shifts are too large to originate from a monochromator misalignment. Through *ab initio* calculations for EuN, Ruck et al. [73] showed that these shifts are observed because of the influence of the weighted ratios of the absorption spectra of divalent and trivalent Eu, found in samples S25 and S26.

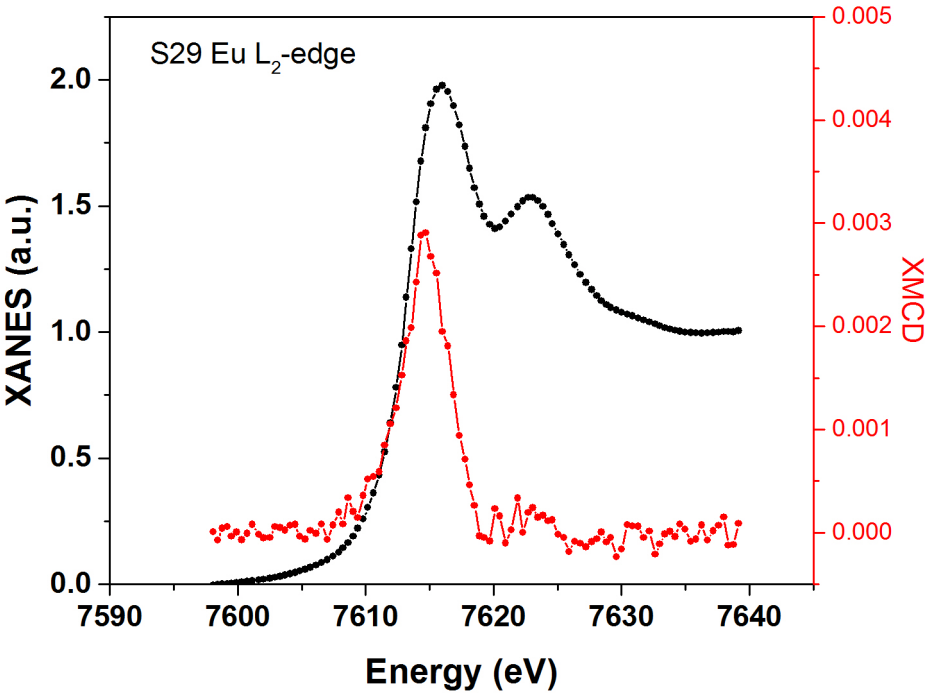

Figure 4.27: XAS and XMCD signal at the Eu $L_2 - edge$ of S29 at RT. The XAS shows some trivalent Eu is present in S29. Therefore, the XMCD signal is smaller compared to S24.

4.3.3 Future XRMS measurements of sample S38

Since the polarisation induced in the EuS layers was found to be larger in EuS/Co multilayers at RT, but the multilayer quality worse compared with EuS/Ni multilayers, a multilayer structure with very thin Co layers between the EuS and Ni layers was designed. The idea was that the overall growth of such a structure would be dominated by

the flat growth of Ni, while the thin Co layers would enhance the Eu polarisation at the interfaces. Additionally, the defects resulting in the presence of trivalent Eu in EuS/Co multilayers, were hoped to be avoided or at least significantly reduced. A prototype sample with six repetitions of Ni and EuS layer thickness of 4 *nm* each and Co thickness of 0.5 *nm* at each interface was produced and measured with x–ray–reflectivity. As shown in figure 4.28, three clear Bragg–peaks are observed and a fourth one is only slightly visible and indicated. The multilayer period, i.e. one Ni/Co/EuS/Co repetition, was calculated to be 9 *nm*, matching the intended thickness values as shown in table 4.3.
The growth quality as judged by XRR shows that the quality is indeed enhanced compared to pure EuS/Co multilayer and slightly worse compared with pure EuS/Ni multilayers.

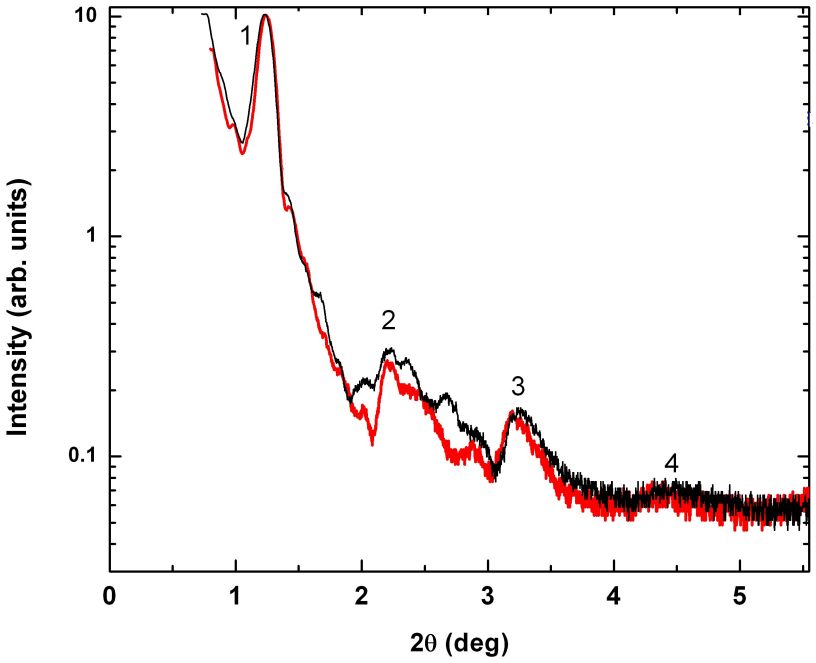

Figure 4.28: Two XRR measurements of the prototype N-C-EuS-1 sample consisting of a EuS/Ni multilayer with Co decorations of 0.3 *nm* at each interface. The growth quality is reduced compared to pure EuS/Ni multilayers but considerably better compared to pure EuS/Co multilayers. Four Bragg peaks are indicated by numbers.

The effect of Eu polarisation induced at RT in the vicinity of Ni and Co is believed to be an interface effect. However, XMCD only gives an average value for the layer or layers measured. No information about the extend of the polarised region can be inferred from XMCD measurements.
Naturally, the next step in the study of EuS/Ni and EuS/Co multilayers is to really measure how far the induced polarisation extends into the individual EuS layers. For this purpose, XRMS measurements will be done on samples S37 and S38.

XRMS is similar to XMCD and is essentially a polarisation–sensitive reflectivity measurement. Initially, a XRR determines the presence and positions of Bragg–peaks. After that the x–ray–beam can be set to the desired angle of incidence and the individual XMCD signal of each Bragg–peak can be recorded.
The asymmetry ratio is defined as the quotient of the difference of right– and left–circular polarised x–rays intensities divided by the sum of both and can be measured for each Bragg–peak individually. From the asymmetry ratio the extend of the magnetisation into a material can be calculated.
To ensure a higher number of Bragg–peaks, the repetition of the bilayer sequences was increased. Figures 4.29 and 4.30 show the reflectivity measurements of two samples designed to be measured with XRMS at the E.S.R.F. in the near future.

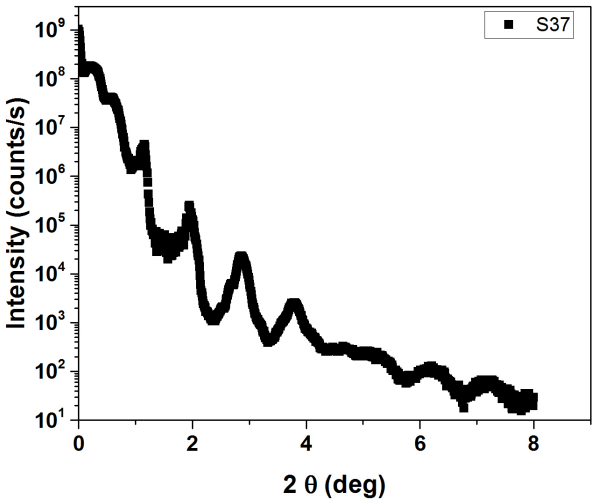

Figure 4.29: XRR of sample S37 showing four Bragg–peaks.

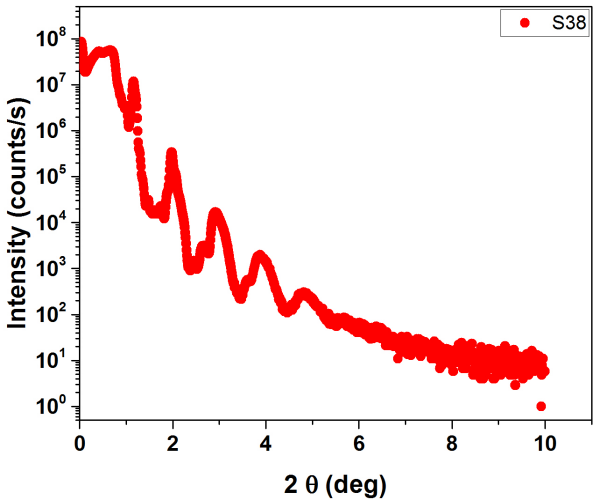

Figure 4.30: XRR measurement of sample S38 showing five Bragg–peaks.

4.4 Summary of Results

EuS/Co and EuS/Ni multilayers were discussed in this chapter. The EuS/Co multilayers are generally less smooth and show an increasing surface roughness with more layer repetitions compared with EuS/Ni multilayers. High resolution TEM scans and XAS show the presence of Eu^{3+} in EuS/Co layers, which is attributed to the formation of defects during growth. The trivalent Eu however, does not contribute to the XMCD of these samples. However, it reduces the average magnetic moment per atom found in these samples, because of its paramagnetism.
XMCD measurement at 5 K of two EuS/Co samples with EuS thickness of 2 and 4 nm in each layer, show a clear peak at the Eu L_2 edge which is proportional to the magnetisation

in EuS. The signal has a maximum value in remanence, where the EuS is antiferromagnetically coupled to Co. An external magnetic field rotates the magnetisation direction of EuS in the direction of the Co magnetisation. 17 T are not enough to align both magnetisation 100% parallel. At RT the XMCD of both samples shows antiferromagnetic alignment between EuS and Co magnetisations. The intensity is lower compared to the 5 K measurement. EuS and Co remain antiferromagnetically coupled for external magnetic fields of at least 600 mT.

XRR and TEM measurements of EuS/Ni multilayers show a much smoother growth of both materials with minimal surface and interface roughness compared to EuS/Co multilayers. XAS shows a largely decreased amount of Eu^{3+} found in these multilayers. XMCD of EuS/Ni multilayers show EuS spin polarisation at RT. The L_2 XMCD signal is smaller than the one found for EuS/Co multilayers with similar EuS thickness.

Both Co and Ni show an enhancement of the EuS T_C which is attributed to the magnetic proximity effect (see chapter 2). The enhancement effect seems to be inversely proportional to the EuS layer thickness.

Polar MOKE measurements at RT were performed on EuS/Co multilayers on a magnetic substrate consisting of Co/Pd multilayers which show inherent perpendicular magnetic anisotropy. High quality magnetic substrates were produced that show a square hysteresis. Additional EuS/Co multilayers deposited on top showed a varying degree of squareness which was close to 90% for multilayers containing thin individual Co layers and decreased with Co thickness.

Measurements of six different samples, A–F, showed different Kerr energy spectra when recorded with zero magnetic field and 2.2 T. The hysteresis loops recorded at different energies changed their shape and saturated at higher magnetic fields in the UV energy range. This higher saturation was attributed to the influence of ferromagnetic EuS which is antiferromagnetically coupled to Co, in agreement with the earlier XMCD measurements. It was possible to disentangle the Co and EuS contributions to the spectra and the hysteresis loops at UV energies for all samples.

Samples having a smaller EuS layer thickness showed about the same degree of Kerr rotation. Two possible explanations for this were discussed, one involving the parallel alignment of only a fraction of the EuS magnetisation at maximum external field. The other one was based on the assumption that the magnetic proximity effect is limited to the fist few atomic layers of EuS and Co only and thus limits the observation of additional Kerr rotation from ferromagnetic EuS beyond a certain thickness.

Finally, growth results of EuS/Ni having much more repetitions than earlier samples were shown. These samples are the basis for future XRMS measurements, that will give more insight into coupling mechanism and how much it extends into the EuS interior.

Chapter 5

Spin–injection from EuS multilayers

The following chapter will deal with the attempt to grow EuS multilayers and single bilayers on top of GaAs–based spin–LEDs and subsequently measure the degree of spin–polarisation in Eu with EL measurements. These were performed in cooperation with the group of Professor Munekata of the Tokyo Institute of Technology. Prof. Munekata researches efficient spin–injection methods of ferromagnetic materials into GaAs–based spin–LEDs using a thin epitaxial AlO_x tunnel barrier [88, 89].
The general working principle of a spin–LED will be described and results of the initial attempts to combine EuS multilayers with them will be shown. The final results will show the first experimentally observed spin–injection from EuS–based layers into spin–LEDs.

5.1 Principle of a spin–LED

Optical Selection Rules

The physical behaviour of a spin–LED is governed by the optical selection rules. There are two ways of producing a spin–polarised EL: One is the the excitation of the LED by irradiation and the creation of spin–polarised excited states which will decay through selection rules and emit spin–polarised luminescence. The second way is to inject a spin–polarised current in the LED and have it recombine in the LED's active region, again emitting spin–polarised luminescence.
Exemplary, the schematic band structure of GaAs is shown in figure 5.1a.
The conduction band is separated from the valence band, which is energetically degenerate for light holes (LH) and heavy holes (HH) at the Γ point. Due to spin–orbit interaction, there is an additional spin–orbit–split–off band about 0.34 eV below the valence band at $k = 0$ [90]. In figure 5.1b the interband transition probabilities for right and left–circularly polarised light are shown. Strictly, the probabilities are only exactly valid at $k = 0$. In a first approximation, they can also be used as a rule of thumb in the vicinity

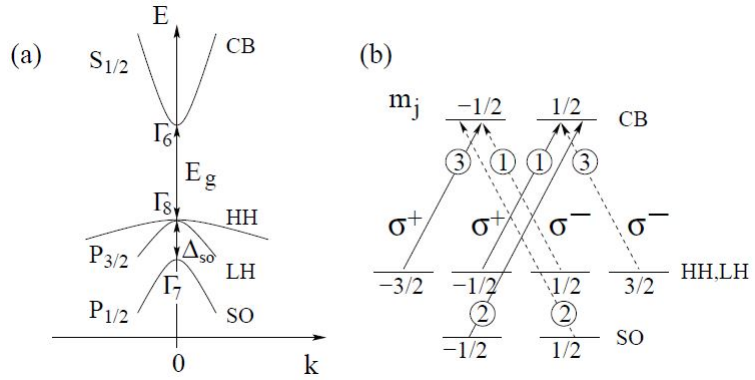

Figure 5.1: (a) Schematic Band Structure of GaAs around the center of the Brillouin zone. E_g and Δ_{so} denote the energy gap and spin–orbit splitting between the Γ_7 and Γ_8 bands. The conduction band (CB), Heavy–Hole (HH), Light–hole (LH) and Spilt–off band (SO) are also shown. (b) Selection rules for interband transitions between the m_j sublevels for circularly polarised light σ_+ and σ_-. The relative transition intensities are given by the numbers in circles. From [3].

of $k = 0$ [7]. The transitions are indicated by arrows and their probabilities represented by numbers next to the arrows. The transition probabilities involving a heavy hole are three–times more likely than the ones involving light holes. If one takes into account transitions from the spin–orbit–split–off band, the transition probabilities are equal for both types of circularly polarised light.
The polarisation of an electron system P_e is given by:

$$P_e = \frac{n_+ - n_-}{n_+ + n_-} \tag{5.1}$$

where n_+ and n_- are the density of electrons carrying spin–up and spin–down respectively. The degree of circular polarisation P_c is further given by:

$$P_c = \frac{I^+ - I^-}{I^+ + I^-} \tag{5.2}$$

where I^+ and I^- are the intensities of right and left circularly polarised light. Assuming the conduction electrons to be spin–polarised and the holes to be unpolarised, the intensities for right and left–circularly polarised light would be given by:

$$P_c = \frac{(0.75 \cdot n_+ + 0.25 \cdot n_-) - (0.75 \cdot n_- + 0.25 \cdot n_+)}{(0.75 \cdot n_+ + 0.25 \cdot n_-) + (0.75 \cdot n_- + 0.25 \cdot n_+)} = \frac{1}{2} \cdot \frac{n_+ - n_-}{n_+ + n_-} = \frac{1}{2} \cdot P_e \tag{5.3}$$

The measurable circular luminescence is thus connected to the initial electron spin polarisation in the conduction band by the factor of 1/2. If the EL is detected after external excitation (e.g. through a laser) and $E \gg E_g + \Delta_{so}$ no degree of circular polarisation will be measurable because the recombination probabilities for right and left circularly

polarised light are equal (see figure 5.1 (b)).
Dyakonov and Perel suggested that removing the degeneracy in heavy and light hole bands should increase the measurable circular polarisation [91]. Therefore, some spin–LEDs use two–dimensional quantum wells (QW) as active recombination regions which remove the energetic degeneracy between heavy and light holes, leading to an energetically higher level of the heavy–hole band. Because of that and the fact that the heavy–hole–transitions are three times more likely than the light–hole–transitions, the conduction band to light–hole transitions can be disregarded when evaluating the EL polarisation, which then becomes

$$P_c = P_e \tag{5.4}$$

The same effect can be found in strained semiconductor layers (growth induced, e.g. through lattice mismatches). Vasilev et al. reported a P_c of 0.8 induced by photoluminescence [92] and Oskotskij a value larger than 0.9 [93].

Impedance mismatch

The general idea of a spintronic device is to inject (and detect) spin–polarised carriers into semiconductors. An initial device proposed by Datta and Das suggested the use of ferromagnetic metals as an injection source [94]. Experiments with devices using a direct ferromagnetic metal–semiconductor interface have only shown less than 1% spin polarisation [95, 96].
A reason for this was given by Schmidt et al., who showed that the different conductivities of the metal and semiconductor are mainly responsible for the low injection efficiency [97]. This is known as the impedance mismatch.
There are a number of ways around this problem. Oestreich et al. proposed the use of diluted magnetic semiconductors which would act as spin–aligners for the injected electrons [98]. This was experimentally observed by a number of groups, e.g. by Ohno et al. using (Ga,Mn)As [99], by Fiederling et al using ($Be_xMn_yZn_{1-x-y}Se$) [100] and Jonker et al. using $Z_{1-x}Mn_xSe$ [101], who all achieved much higher spin injection efficiencies. The drawback of using diluted magnetic semiconductors lies in their low Curie temperature and indeed, all experiments mentioned were performed at low temperatures.
Another solution to the impedance mismatch problem was found by Rashba [102] as well as Fert and Jaffres [103] who propose tunnel contacts as a solution. The principal idea of the tunnel barrier is to function as a spin–selective additional resistance, dominating the charge transport from ferromagnetic metal into the semiconductor. The transmission through the tunnel barrier is proportional (to first order) to the product of the density of states on both sides of the barrier (metal and semiconductor). The spin–selectivity arises from the spin–asymmetry in the ferromagnetic metal.

The concept of tunnelling to achieve higher spin–injection efficiencies has been used in metal–semiconductor Schottky barriers operated in reverse bias, e.g. by Albrecht et al. [104], Li et al. [105] and van 't Erve et al. [106].
Other tunnel barriers have been used by a variety of groups, e.g. Motsnyi et al. [107], Benabderrahmane et al. [108] and Nishizawa et al. [88] have used AlO_x–based tunnel barriers, while Mgo was used by Jiang et al. [109] and Sasaki et al. [110].

Detection Geometries

There are three general emission types of spin–LEDs: the Faraday, Voigt and Hanle configuration. This thesis will explain the two common ones, the Faraday and Voigt configuration.
Most spin–LEDs make use of quantum wells, which are typically in the 10 nm–thickness–regime. The advantage of the quantum wells lies in the possible direct observation of the electron spin–polarisation because of the lifted energetic degeneracy between light–hole and heavy–hole energy states.
In a quantum well, the angular momentum of the heavy holes lies in the growth direction, i.e. perpendicular to the surface. Because of this, the quantization axis for the optical transitions is also perpendicular to the surface and favours surface emission. This is known as the Faraday configuration.
As most magnetic materials have their easy axis of magnetisation in–plane due to shape anisotropy, surface emitting spin–LEDs need external magnetic fields to rotate the sample magnetisation out of plane, which usually requires larger magnetic fields. Also, the typical escape distances for the photons in surface emitting devices is usually around 100 nm, which minimizes photon reabsorption.

The Voigt or edge–emitting configuration on the other hand, does not require large magnetic fields as it can make use of the aforementioned shape–anisotropy and requires only moderate magnetic fields to magnetically saturate the samples along the emission direction. The distances that the photon has to travel in an edge–emitting device are usually much larger compared to surface–emitting devices, which might pose a problem due to reabsorption during the detection process.
Edge–emitting spin–LEDs do not work with quantum wells as was demonstrated by Fiederling et al., who investigated the spin–injection in top and side emission [111]. In his studies, Fiederling used a 15 nm wide quantum well. However, as shown by van 't Erve et al. if the size of the quantum well is increased from 10 to 50 nm, the angular momentum of the heavy holes is no longer exclusively oriented perpendicular to the surface but starts to rotate in–plane with increasing quantum well thickness, which makes the observation of polarised EL from side–emission possible [112]. Nishizawa et al. used

even wider, bulk–like, active areas of about 500 nm to observe polarised EL.
In these wide active areas, the degeneracy between light and heavy hole is no longer lifted, which reduces the observable optical polarisation to 50% ($P_c = \frac{1}{2} \cdot P_e$).
An overview of the achieved spin–polarisations for the different types of spin–LEDs is given by Bsiesy [113] and Holub and Bhattacharya [114].

5.2 Experimental Setup

A schematic overview of the experimental setup used for the EL measurements is shown in figure 5.2. The sample is mounted on a custom–built sample holder which is shown in figure 5.3. The holder consists of a copper block, which acts as the ground, and individual copper fingers, acting as front contacts on each sample.
The holder is designed to hold multiple samples at once. Each sample is placed between the copper block and the copper finger, which is then tightened with a screw to the copper block. Because of the very small sizes of the samples and the copper fingers, this procedure is quite delicate and it may take several tries to get a steady connection. A golden wire attached to the copper finger acts as an additional backup contact.
Once the sample is mounted, the sample holder is placed inside a cryostat, containing a superconducting magnet. The cryostat can cool down to 4 K, allowing a maximum magnetic field of 2 T. At RT, only measurements without magnetic field are possible.
The EL emitted from the sample passes the cryostat window, a collimating lens ($f = 20\ cm$), a second focusing lens ($f = 50\ cm$), a quarter wave plate, an analyser, a chopper and reaches an optical fibre input, where the signal is transmitted to a monochromator and detected by a photo–multiplier–tube.

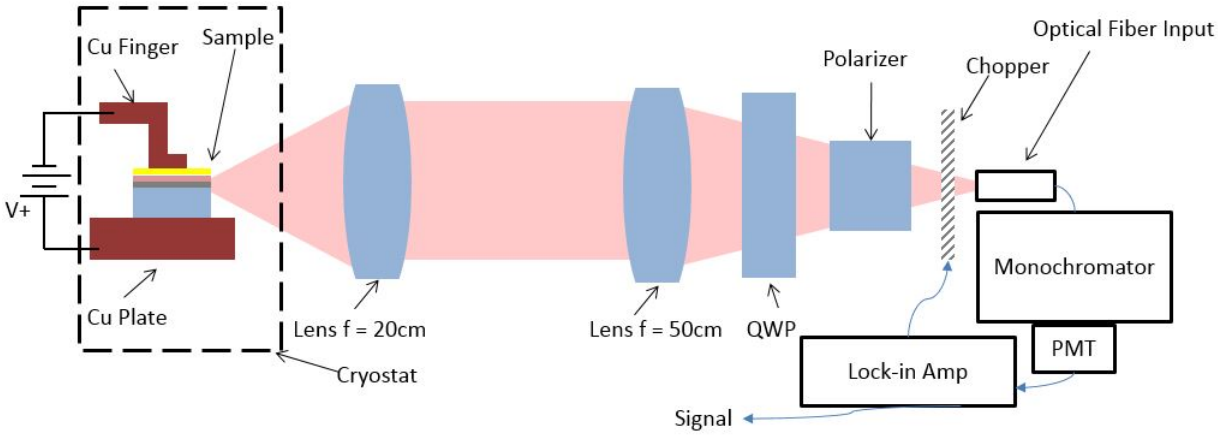

Figure 5.2: Schematic diagram of the setup used for EL measurements. The schematics are not shown to scale and individual parts appear smaller or larger than their real–life counterparts.

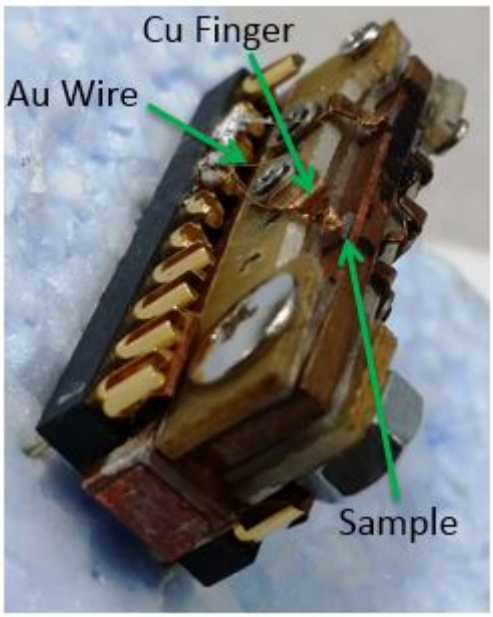

Figure 5.3: Photograph of the custom–built sample holder. The sample, Cu finger and Au wire are indicated by arrows.

The chopper is operated by a lock–in–amplifier, used to enhance the signal–noise–ratio of the measurement. The measured signal is then received and stored on a lab computer.
The sample is connected with a power supply, which could supply up to 105 mA of maximum current for the measurements performed during the stay at the lab. The power supply additionally acted as multimeter, allowing the measurement of current–voltage characteristics (I–V–curves) of the samples.
To verify that electroluminescent light was indeed emitted by the sample, a CCD–camera was pointed at the sample holder. A simultaneous measurement of the EL polarisation and the detection of EL light was not possible, because of the sample holder's position in the cryostat. It was impossible to place the CCD camera, so that the sample holder would be visible while all the other optical components were in place. For the observation of the EL light from the sample, it was necessary to remove the optical components. If EL light was detected, the components were moved back into place and the measurement was started.

5.3 Results

The samples shown in this section were evaporated either in the Balzers chamber or the MBE growth chamber, shown in chapter 3. All El measurements were carried out in side–emission.
As an initial test, the EuS multilayers were grown on the first series of substrates received from Japan, which did not yet contain the AlO_x barrier. As shown in chapter 4, growing

EuS multilayers on these substrates, did not change the growth and roughness observed in the EuS/Co layers. Following these results, a second series of substrates was sent. Given their successful experience using the AlO_x, Prof. Munekata encouraged a first try with the tunnel barrier. The samples were prepared by e–beam–evaporation by members of his group and had the following structure: $AlO_x/n-AlGaAs/n-GaAs$. On top of these, two samples were prepared in the Balzer chamber at RT.
They were named S–LED–1 and S–LED–2, having the two structures
$Au(10\ nm)/[Ni(8\ nm)/EuS(2\ nm)]_9/substrate$ and
$Au(10\ nm)/Ni(8\ nm)/EuS(2\ nm)/substrate$ respectively. The Au was evaporated on top to ensure better electrical contacts. After preparation, they were sent to Japan for EL measurements.

5.3.1 AlO_x tunnel barrier

A SQUID measurement was taken at 5 K of S–LED–1 with external magnetic field parallel to the GaAs (110) direction, which is shown in figure 5.4. The external magnetic field was varied between $-2\ T$ and $2\ T$. The magnetisation is not saturated for high fields, reaching a maximum value of about 230 $\frac{emu}{cm^3}$, where emu stands for electromagnetic unit. At zero external magnetic field, the magnetisation is at around 110 $\frac{emu}{cm^3}$ as shown in the inset. The net magnetic moment of Ni is larger compared with EuS in S–LED–1, so the Ni magnetic moment will follow the external magnetic field. The measurement shows that almost the entire net magnetic moment of the EuS/Ni multilayer is oriented parallel to the substrate's (110) direction and small magnetic fields ($0.2-0.3\ T$ as judged from the inset) are enough to saturate it in the (110) direction. The magnetisation per unit volume is given by:

$$M = \frac{N[\frac{Atoms}{unitcell}] \cdot \mu[\frac{\mu_B}{Atom}]}{V_{Unitcell}} \tag{5.5}$$

Calculating the magnetisation for Ni ($0.6\ \frac{\mu_B}{Atom}, a = 3.52\ \mathring{A}$) and EuS ($7\ \frac{\mu_B}{Atom}, a = 6.968\ \mathring{A}$) gives:

$$M_{Ni} = \frac{4 \cdot 0.6\mu_B}{(3.52 \cdot 10^{-10}m)^3} = 5.1\ \cdot 10^5\ \frac{A}{m} = 5.1 \cdot 10^2 \frac{emu}{cm^3} \tag{5.6}$$

$$M_{EuS} = \frac{4 \cdot 7\mu_B}{(6.968 \cdot 10^{-10}m)^3} = 1.22\ \cdot 10^6\ \frac{A}{m} = 1.22 \cdot 10^3 \frac{emu}{cm^3} \tag{5.7}$$

using, that $\frac{emu}{cm^3} = 10^3\ \frac{A}{m}$. S–LED–1 theoretically contains 80% Ni and 20% EuS, which are antiferromagnetically coupled (at 5 K, i.e. the measurement temperature, the entire layers are antiferromagnetically coupled), so the net magnetisation of S–LED–1 is given

by the weighed difference between Ni and EuS magnetisations:

$$M_{S-LED-1} = 0.8 \cdot 0.51 \cdot 10^3 \frac{emu}{cm^3} - 0.2 \cdot 1.22 \cdot 10^3 \frac{emu}{cm^3} = 1.64 \cdot 10^2 \frac{emu}{cm^3} \quad (5.8)$$

This value is in agreement with the saturation value at low magnetic fields. Until 0.5 T the magnetisation appears to be constant at about 160 $\frac{emu}{cm^3}$. With increasing magnetic field, the antiparallel coupling starts to break up and the moments of Eu and Ni are aligned parallel which increases the measured net magnetisation. At 2 T, a magnetisation value of about 230 $\frac{emu}{cm^3}$ is found. According to equation 5.8, this corresponds to an in–plane–projection of the EuS magnetic moment of about 70%. The remaining 30% do not lie in the measurement plane and do not contribute to the in–plane magnetisation.

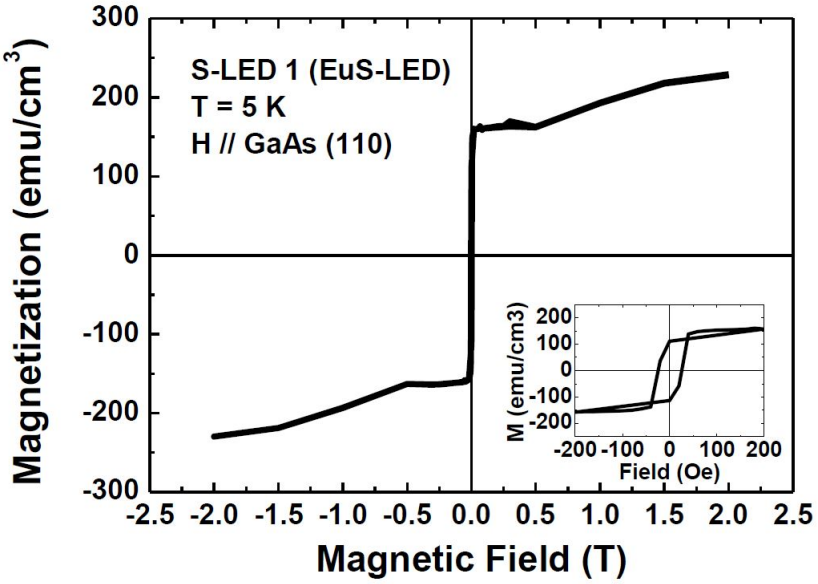

Figure 5.4: SQUID measurement of S–LED–1 at 5 K. The inset shows the remanent magnetisation of the EuS/Ni multilayer. The sample magnetisation is constant for low magnetic fields up to 0.5 T. Higher magnetic fields break up the antiferromagnetic coupling and the net magnetisation increases.

I–V curves of S–LED–1 were measured at RT and 5 K and are shown in figure 5.5a and 5.5b. The curves are plotted with logarithmic scale and the current values for reverse bias (negative) are shown as absolute values. For comparison, in figure 5.5c and 5.5d the I–V curves of a typical spin–LED with Fe and AlO_x barrier are shown.
For the typical Fe–spin–LED, the I–V–curves at low and RT appear symmetric, which is attributed to the presence of the AlO_x barrier, i.e. the carrier transport is dominated by tunnelling through the barrier for forward and reverse bias. Indeed, Munekata et al. were able to show that fitting the I–V–curves presented in [88] with Simmons' equation [115] for the tunnel current, gave a barrier height of about 2.8 eV and a barrier width of 1 nm.

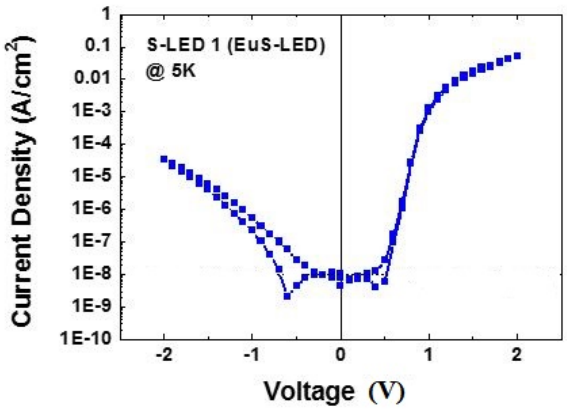

(a) I–V curve of S–LED–1 at 5 K in logarithmic scale. The absolute value of the current in reverse bias is shown.

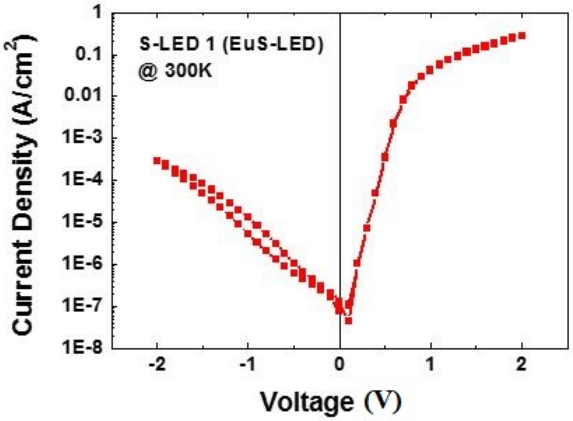

(b) I–V curve of S–LED–1 at 300 K in logarithmic scale. The absolute value of the current in reverse bias is shown.

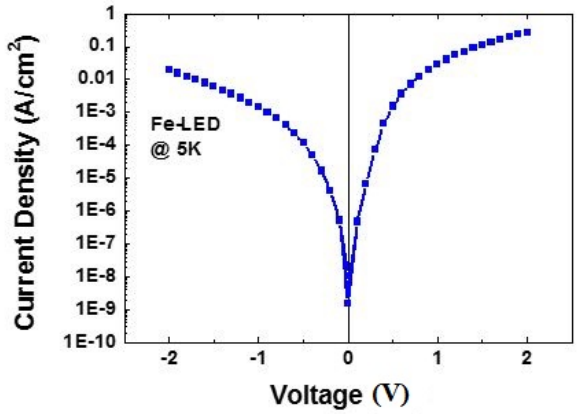

(c) I–V curve of an Fe layer on a spin–LED at 5 K logarithmic scale. The absolute value of the current in reverse bias is shown.

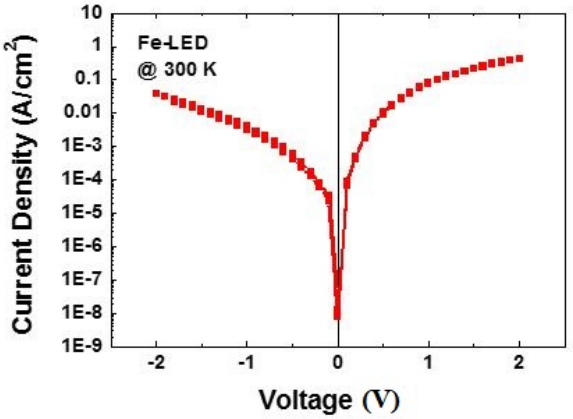

(d) I–V curve of an Fe layer on a spin–LED at 300 Kin logarithmic scale. The absolute value of the current in reverse bias is shown.

Figure 5.5: I–V curves of S–LED–1

Both values were in good agreement with similar values observed for the barrier height and the intended thickness of the AlO_x layer.
Forward and reverse bias current approximately differ by a factor of 10. At lower temperature, there are less carriers available, reducing the measured current. Nevertheless, for the Fe–LEDs, the maximum currents are still comparable.
For S–LED–1, the I–V–curves are not symmetric. Instead, the measured current is always higher for forward bias by several orders of magnitude, as opposed to the Fe–LED. The current threshold is also higher for S–LED–1 (about 0.8 V at 5 K, 0.6 V at 300 K) compared to the Fe–LED (about 0.6 V at 5 K, 0.4 V at 300 K). The carrier transport in S–LED–1 does not seem to be dominated by tunnelling, which could be the case if Ni was the first layer in contact with the AlO_x barrier, but instead by the first EuS layer located between Ni and AlO_x.
Finally, the EL of S–LED–1 was measured. Measurements were performed at ± 1 T and at remanence. The results are shown in figure 5.6. The degree of circular polarisation is low for the three cases. Measuring at ± 1 T gives a negative degree of polarisation (-0.7% at 1 T and -0.6% at -1 T). At remanence, a degree of +0.8% is observed. The energy corresponds to transitions in the GaAs substrate's active region. The difference of right and left circularly polarised light emitted from the LED is too low to draw any conclusions about the influence of the EuS/Ni layers. The low degree resembles the first tries of realizing spin–injection with Fe layers on spin–LED's which were unsuccessful due to the problem of the impedance mismatch between metals and semiconductors. It appears, that the presence of the AlO_x barrier has prevented successful spin–injection from the Ni/EuS side into the GaAs active region.
Theoretically, EuS should behave as a spin–filter below its T_C (as discussed in the theoretical section about EuS). As a spin–selective tunnel barrier, EuS should then have two different barrier heights for spin–up and spin–down electrons, favouring the spins aligned parallel to the Eu magnetic moment. Because the entire layer of EuS is ferromagnetic at 5 K, the EuS tunnel barrier would have a thickness of about 2 nm. The AlO_x barrier has an additional thickness of about 1 nm and acts as a second tunnel barrier which is not spin–selective. Assuming that the majority of the electrons tunnelling through the EuS spin–selective–barrier from the Ni side are spin–polarised, the presence of the additional AlO_x tunnel barrier would decrease the injection efficiency largely because of the second tunnelling step that has to take place at the barrier. So, while a tunnel barrier solves the impedance mismatch problem between metals and semiconductors and allows for spin–injection, here it hinders any significant spin–injection. Because of the discouraging findings for S–LED–1, it was decided not to analyse S–LED–2. Instead, a second series of samples were prepared on spin–LED wafers, this time without the AlO_x barrier.

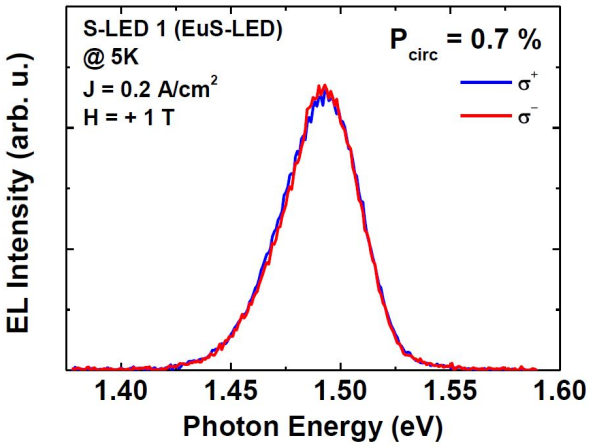

(a) EL of S–LED–1 at 5 K at 1 T

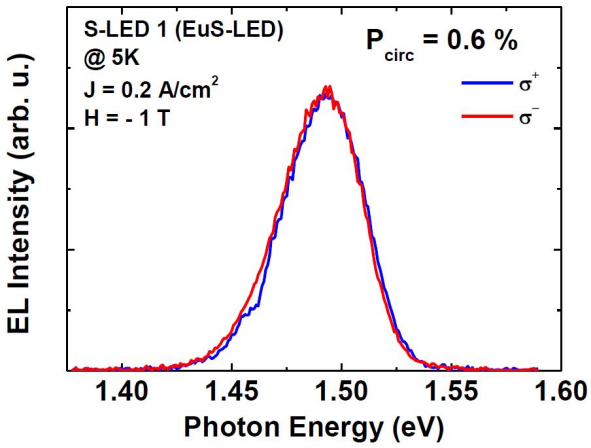

(b) EL of S–LED–1 at 5 K at -1 T

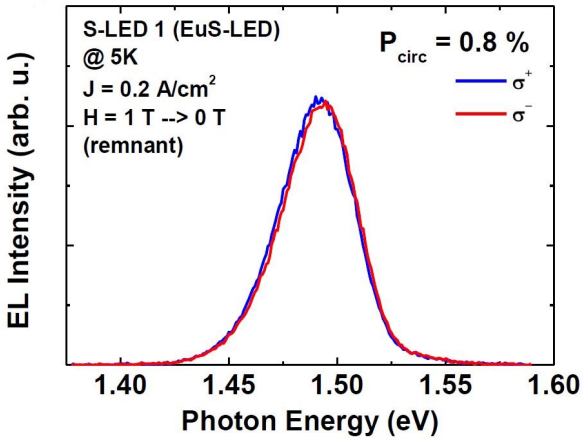

(c) EL of S–LED–1 at 5 K at remanence

Figure 5.6: EL of S–LED–1

5.3.2 Custom spin–LED

The custom spin–LED wafers were bought from the South Korean company Optowell. The structure of such an LED is shown in figure 5.7. Naturally, the wafers will be oxidised on top, which is usually removed by heating before further processing of the wafers. The oxygen was removed in Japan and a thick amorphous Arsenic passivation layer deposited afterwards to prevent renewed oxidation. The Arsenic passivation process is described by Knorr et al. [116]. According to Knorr et al. the Arsenic layer could be removed by heating the wafer to about 250 $°C$.

n-GaAs	GaAs cap	15 nm	Si : 5E18 cm^{-3}
n-$Al_{0.3}Ga_{0.7}As$	Clad	500 nm	Si: 1E17 cm^{-3}
i-$Al_{0.3}Ga_{0.7}As$		15 nm	
p-GaAs	Active	500 nm	C : 1E18 cm^{-3}
p-$Al_{0.3}Ga_{0.7}As$	Clad	500 nm	C : 1E18 cm^{-3}
p-GaAs		500 nm	C : 1E18 cm^{-3}
p-GaAs sub. (100)		350 μm	Zn : 1.3-2.0E19 cm^{-3}

Figure 5.7: Configuration of the custom ordered spin–LED wafer, showing each layer thickness and doping concentration.

Sample Preparation

After receiving the treated wafers from Japan, an initial test of removing the As passivation layer was carried out in the growth chamber of the MBE system. The As was removed by heating the wafer to about 250 $°C$ for 90 to 120 minutes. The crystalline quality of the substrate was checked by *in situ* RHEED and the absence of oxygen and other contaminations checked by AES. Both RHEED and AES confirmed that the As layer was absent.

Four different samples were prepared on the custom wafers in the Balzers evaporation chamber. Each time, the wafers were heated to 400 $°C$ (the heater in the Balzers chamber is further away from the substrates and the higher temperature was chosen to compensate for the larger distance) for 90 to 120 minutes. The samples are shown in table 5.1.

Each sample was started with EuS as the first layer. EuS/Co layers were chosen for most of the samples. Most samples only have a bilayer of EuS/Co or EuS/Ni because only the

sample name	Structure (Å)
J1	$[EuS(20)/Co(60)]_1/EuS$
J2	$[EuS(20)/Co(60)]_2/EuS$
J3	$EuS(20)/Ni(80)$
J4	$EuS(10)/Co(60)$

Table 5.1: Overview of the samples prepared on the custom spin–LED wafers for EL measurements.

final (initial) EuS/AlGaAs interface is important for the spin–injection. The intention of sample J2 having two repetitions of EuS/Co was to check, if that has any influence on the measured circular polarisation. The idea behind J4 was to decrease the thickness of the EuS tunnel barrier by half which should result in a higher degree of polarisation.
To ensure the possibility of emitting EL, the samples were initially tested for photoluminescence. The samples were excited with a HeNe–laser with 4 mW power and their emitted photoluminescence recorded through an optical fibre connected to a monochromator and a CCD camera. All samples showed photoluminescence in the expected energy region corresponding to transitions in the GaAs active region. After checking the presence of photoluminescence, the samples were capped with a thick gold cover layer for better electrical contacts.

EL measurements

For the EL measurements, the samples were cut into pieces smaller than 1 mm x 2 mm. All samples were tested for EL at low temperature (8 K) and prior to each measurement their I–V curves were recorded. The I–V curves revealed a lot of leak current for some pieces, whereas others showed LED current–voltage–characteristics. Due to the high leak current (which probably resulted due to some defects on the surface or impurities) and limitation of the power supply to about 100 mA, unfortunately, most samples did not show EL at all. The ones that showed initial EL sometimes burned through and short circuited either before or during a running measurement.
Nevertheless, it was possible to record the EL spectra for some samples. Most of the EL measurements show a very low signal–to–noise–ratio which could be due to two things. One is a very low EL intensity. The other one is due to the light detection path: The presence of EL was checked by a CCD camera for which the optical components had to be moved out of the light path. When the voltage applied to the sample was increased enough, so that a stable light emission was visible with the camera, the components were put back into place and the camera removed. It cannot be excluded, that the signal was not entirely focused on the detector which would result in a lower signal. Also, during repetitive measurements of one and the same sample piece, it was noticed that the

intensity of the emitted light went down over time, due to the degradation of the LED. Given that the circular polarisation is calculated by the intensities of the emitted right and left circularly polarised light, this posed a challenge.
Due to the low signal–to–noise–ratio, it is unclear, if most of the samples really showed polarised EL. As an example, a measurement of a piece of sample J2 at 8 K and 1 T is shown in figure 5.8.

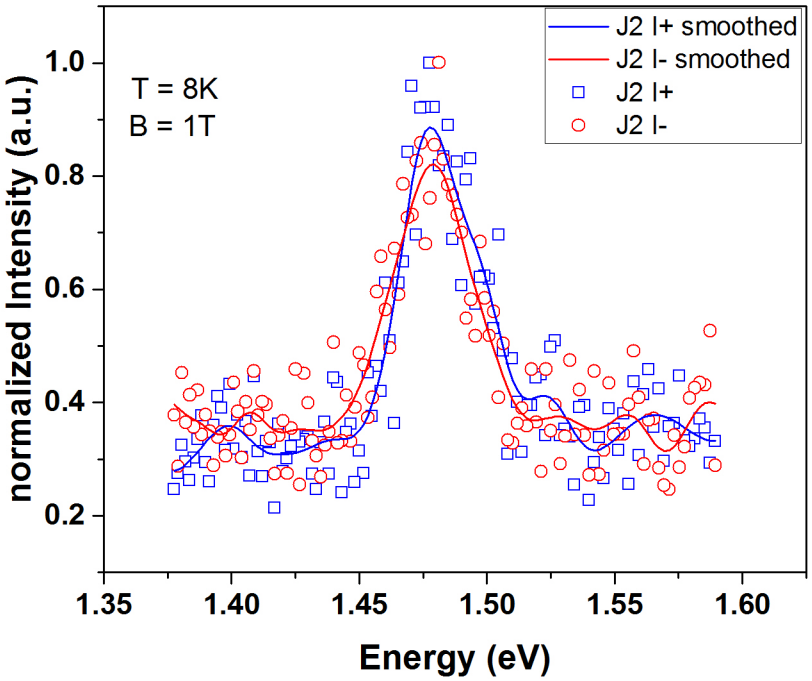

Figure 5.8: Electroluminescence measurement of J2 at 8 K and 1 T. The signal–to–noise–ratio is quite small. The recorded intensities for right and left circularly polarised light have been smoothed. The calculated degree of circular polarisation after smoothing is $P_c = 5.9\%$.

The intensity has been normalized, however, the measurement is quite noisy. The raw data suggests that the intensity of right circularly polarised light is slightly higher than left circularly polarised light. Both raw data sets were smoothed and are indicated in figure 5.8. The smoothed data now shows a clear difference for both intensities. The degree of circular polarisation calculated from the smoothed data is $P_c = 5.9\%$. Another sample piece of J2 however, showed a much higher signal–to–noise–ratio and a clear difference for left and right circularly polarised EL. The piece was measured at 8 K with a maximum applied field ± 2 T and in remanence for both initial field directions. The results are shown in figures 5.9 and 5.10.
The observed degree of circular polarisation is $P_c = -5.3\%$ for positive remanence (zero magnetic field after initially applying a magnetic field of $+2$ T) and $P_c = 5.3\%$ for negative remanence (zero magnetic field after initially applying a magnetic field of -2 T).
The observed change of sign of P_c for both remanent states indicates that the observed

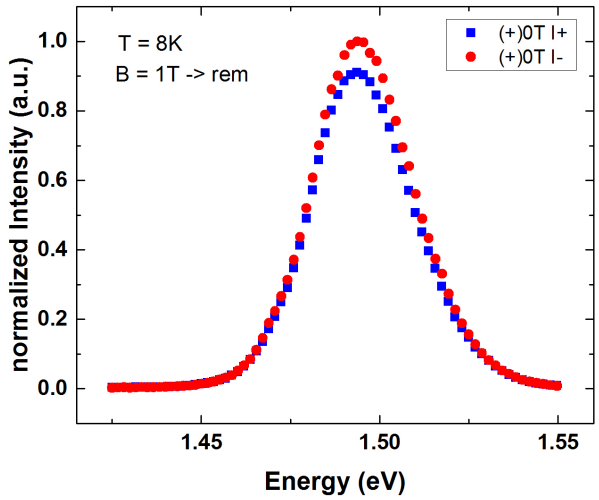

Figure 5.9: Electroluminescence measurement of J2 at 8 K at positive remanence.

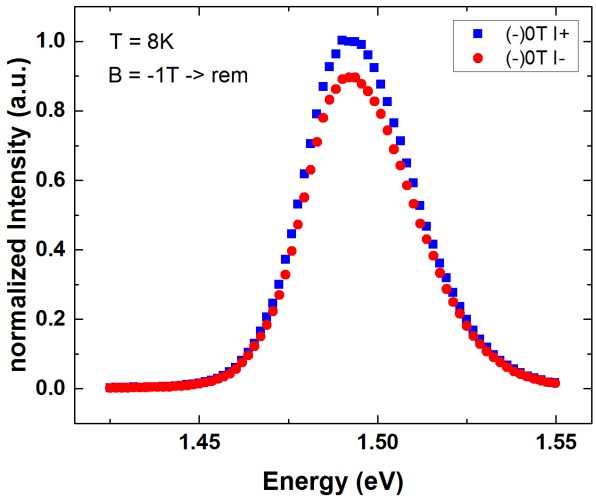

Figure 5.10: Electroluminescence measurement of J2 at 8 K at negative remanence.

degree of polarisation is indeed due to the spin–polarised current from the injection side and not due to artefacts. When the direction of the external magnetic field changes, so does the spin–polarisation at the injector side. The transition probabilities governing the recombination of spin–up and spin–down electrons in the GaAs active region are still valid and thus, according to equation 5.3 the sign of the circular polarisation changes.
The degree of P_c found for this piece of J2 is similar to the estimate from the smoothed raw data of another piece of J2 (figure 5.8). The results of the second piece are more convincing because of the clearly observed intensity difference and the change of sign for both magnetic field directions.
The degree of P_c is somewhat low, however. Given that all of the EuS should be ferromagnetic at 8 K a higher degree of spin–polarised current injection could be expected.
The polarisation of the injected electron current calculated by $P_e = 2 \cdot P_c$ for sample J2 is $P_e = 10.6\%$. There are two ways in which the current can flow from the front contact of the LED (Gold covered Co/EuS) to the back contact (p–GaAs substrate). One is through tunnelling through the ferromagnetic EuS layer and the other being a direct current through the EuS conduction band. Both would result in a spin polarised current. The tunnelling through the EuS would be spin–selective with a lower barrier height for the spins having a parallel alignment to the EuS magnetic moment. For the case of direct current, it would pass through the exchange split $5d$ conduction band of EuS. The energy splitting is about 0.34 eV in the ferromagnetic state of EuS and would favour the parallel alignment of the electron spins to the EuS magnetic moment.

After the successful measurement of polarised EL in this particular piece of J2, it was also measured at RT. No magnetic field could be applied at RT, due to the superconducting magnet, so that only one remanence measurement was possible. The measurement is

shown in figure 5.11.

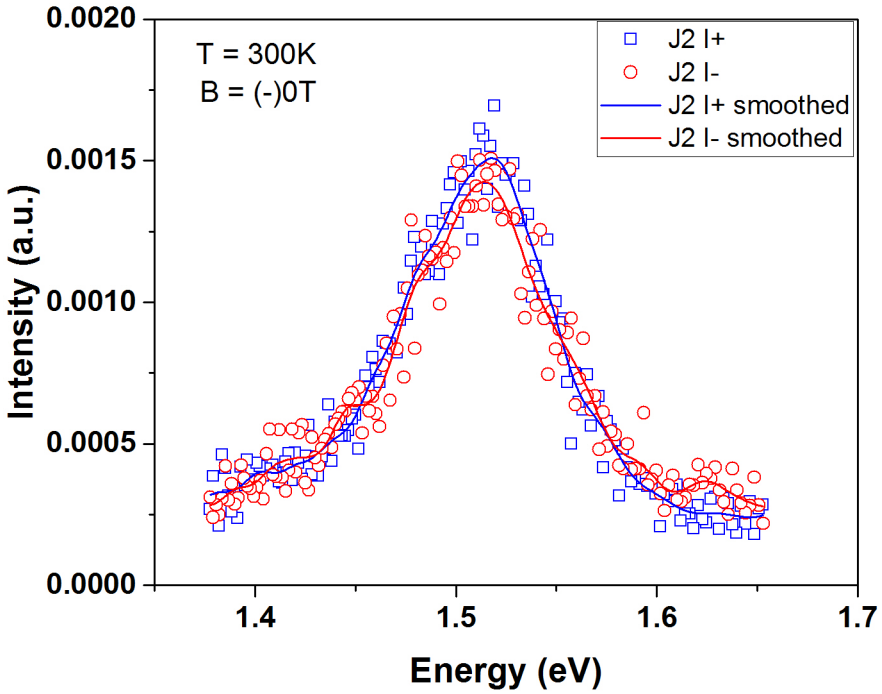

Figure 5.11: Electroluminescence measurement of J2 at RT and negative remanence. The signal–to–noise–ratio is much smaller compared to low temperature. The recorded intensities for right and left circularly polarised light have been smoothed. The calculated degree of circular polarisation after smoothing is $P_c = 2.3\%$.

The external magnetic field is zero but indicated as negative remanence, as the external magnetic field's last direction regarding the sample was negative, before the temperature was raised. The intensity of the measured data is lower compared with the measurement at 8 K, which could either be due to the focus of the EL not being entirely on the detector or because of a higher recombination rate of holes and electrons in the GaAs wafer due to the increased temperature, which would result in a decreased EL intensity.
The raw data again only suggests a difference between RCP and LCP EL and needs to be smoothed in order to extract a value for P_c. A value of $P_c = 2.3\%$ is calculated. The sign of the degree of circular polarisation is the same as the one measured at 8 K, which is encouraging.
The degree of circular polarisation found at RT is less than at 8 K, which could indicate that the EuS layer is no longer entirely ferromagnetic. Part of it will remain antiferromagnetically coupled to the Co, but the exact extend of the coupling into the EuS layer has yet to be investigated. So far, an interfacial coupling extending to the first few monolayers of EuS is assumed. Within this assumption, it would be reasonable to say that the spin–polarised carriers are created again either through tunnelling through a now thinner EuS barrier or through directly passing through the spin–polarised conduction band of the (again thinner) ferromagnetically ordered layer of EuS. In both cases, a paramagnetic EuS

barrier would still need to be passed before entering the wafer. In this second EuS part, the conduction band would no longer be spin–polarised and spin scattering could lead to a decrease of the number of spin–polarised electrons reaching the active region in the GaAs.

In summary, the calculated circular polarisation of the EL measured at RT could originate from the antiferromagnetic exchange coupling between EuS and Co. However, due to the fact that no magnetic field could be applied to check if there is a sign change for P_c with changing magnetic field and the inconclusive raw data render the general results of circular polarisation at RT and the conclusion drawn from it at least questionable.

5.3.3 TEM analysis of samples on spin–LED

To further understand why most of the samples did not show steady EL and high leak currents, part of the remaining pieces of the samples J1–J3 were analysed by TEM.

J1 (EuS/Co/EuS)

The TEM results of samples J1 are shown in figure 5.12.

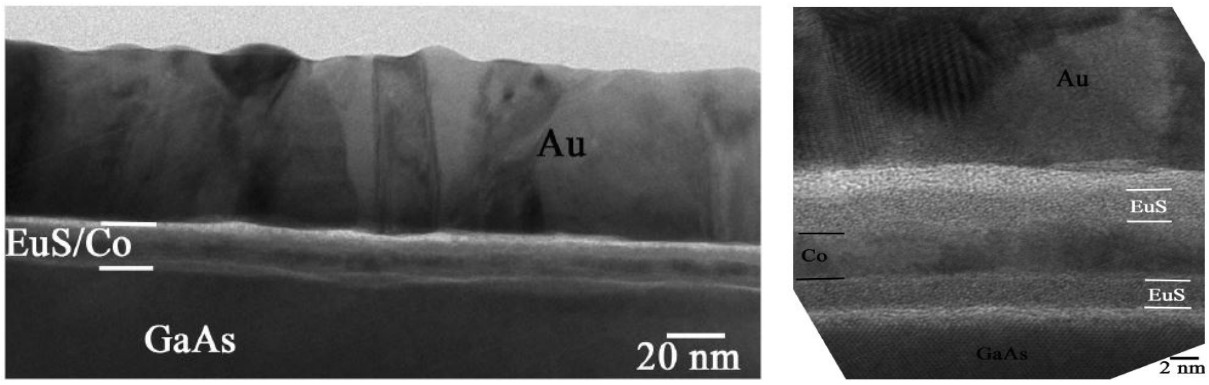

(a) TEM of J1 (b) HTEM of J1

Figure 5.12: TEM measurement of sample J1 showing some interface roughness between the AlGaAs substrate and the first EuS layer. The morphology and roughness of the substrate is followed throughout the layer.

The analysis reveals, that the overall thickness of J1 is 74.2 nm on average. The Co layer has dimensions that range from 3.8 nm up to 4.0 nm, which results in roughness in this layer ($\approx 0.8\ nm$). The same trend applies to the EuS layers, which have thickness ranging from 2.4 nm (bottom layer) up to 3.9 nm (top layer). All three layers of EuS, Co and Au follow the morphology and thickness variations of the GaAs substrate, which is not flat. Their structural details were identified by precise measurements in the HTEM images and present some interesting differences, as shown in figure 5.12b. The Co metallic layers

comprise of, almost exclusively, hexagonal Co phase. On the other hand, both EuS layers do not possess any crystallinity, but are entirely amorphous.
Chemical analysis revealed the presence of Co, Eu and S in the multilayer region, Au in the capping layer, as well as Al, Ga and As in the substrate underneath. Oxygen was the only impurity element detected, which was present due to the oxidised regions prior to the initial EuS layer and after the second EuS. The presence of oxidised regions between the top GaAs buffer layer and the initial EuS could either stem from an incomplete removal of the initial oxygen layer or, more likely, could have formed just after the removal of the Arsenic capping layer and before the deposition of the first EuS layer. The entire deposition however, takes place in high–vacuum, which should prevent the quick reoxidation of a surface on the timescale of hours. It cannot be excluded, that the initial EuS layers in the crucible contained some EuO (or Eu_2O_3) which would then be evaporated first onto the sample.

J2 $((EuS/Co)_2/EuS)$

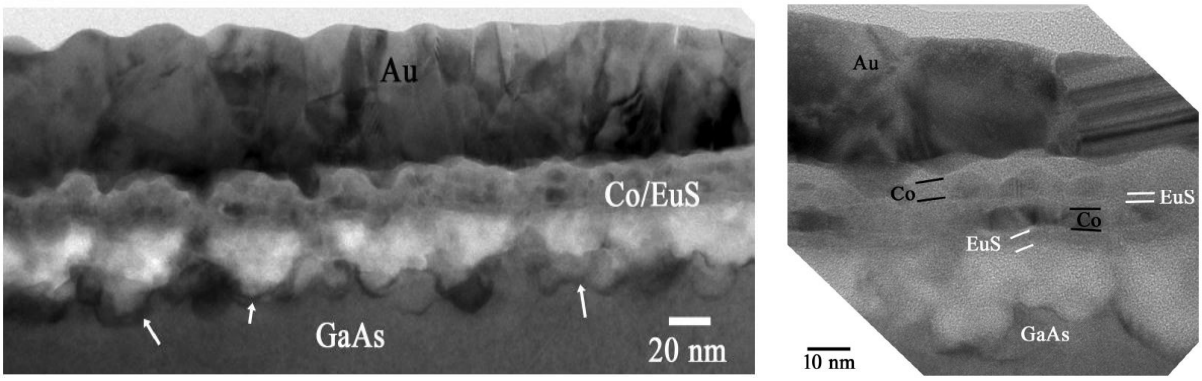

(a) TEM of J2 (b) HTEM of J2

Figure 5.13: TEM measurement of sample J2 showing extensive interface roughness between the AlGaAs substrate and the first EuS layer. The morphology and roughness of the substrate is followed throughout the layer.

The overall thickness of J2 is 94.8 nm on average, ranging from 89.6 nm up to 103.3 nm in different areas. Both the Co/EuS multilayer regions, as well as the GaAs substrate suffer from a large amount of roughness, thickness variations and defected regions, as indicated by white arrows in figure 5.13a. The two Co layers have dimensions in the range of 3.7 nm up to 4.7 nm, with the layer closer to the GaAs substrate being thicker compared to the one above it. Roughness in these layer is also observed, as a result of the non-flat substrate. The same applies to the EuS layers, which have thickness ranging from 3.6 nm on average (bottom layer) down only to 1.6 nm (top layer). All the layers follow the morphology and thickness variations of the GaAs substrate, as shown in figure 5.13b. As for J1, the Co layers are predominantly in the hcp phase and the EuS layers

entirely amorphous.
Chemical analysis revealed the presence of the same elements as found in J1, though this time a larger amount of oxygen was found due to larger region being oxidised.

J3 (EuS/Ni)

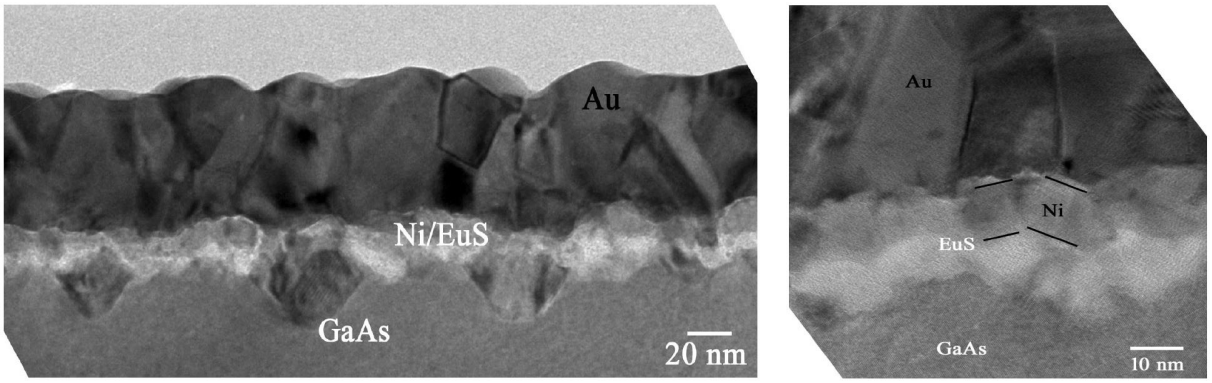

(a) TEM of J3 (b) HTEM of J3

Figure 5.14: TEM measurement of sample J3 showing extensive interface roughness between the AlGaAs substrate and the first EuS layer. The morphology and roughness of the substrate is followed throughout the layer.

The overall thickness of J3 is 81.8 *nm* on average, ranging from 74.2 *nm* up to 85.6 *nm* in different areas. Both the Ni/EuS multilayer regions, as well as the GaAs substrate suffer from a large amount of roughness, thickness variations and defected regions, as shown in figure 5.14a. In addition, a large amount of V–shaped defects are present in the substrate. The Ni layer has a thickness of 9.1 *nm*, on average, with a large thickness span ranging from 5.0 *nm* up to 12.4 *nm*. The high resolution measurement shown in figure 5.14b, again shows that all layers follow the morphology and thickness variations of the substrate.
The Ni metallic layers comprise of, almost exclusively, fcc Ni phase. The EuS layer is again entirely amorphous.

Summary of results for J1–J3

In summary, the results found from the TEM analysis show that all samples show a non–flat spin–LED substrate, while J2 and J3 show considerable interfacial roughness, oxidised parts and defected areas. This was very unexpected and puts the results found from the EL measurements into perspective.
During sample preparation, J1 was heated for a longer time compared to the other samples, which might explain why J1 has a somewhat smoother substrate with less roughness compared to J2 and J3.

The defected areas and oxygen present at the GaAs/EuS interface could also explain, why the I–V curves of some pieces of the samples showed a large leak current and why some pieces did not show any EL.
Given the high amount of roughness and defects found in J2, it is surprising, that a finite circular polarisation of the EL was observed. Nevertheless, the observation of polarised EL with and without magnetic field and the change of sign of P_c with changing the direction of the external magnetic field, suggest that it was indeed possible to observe EL from the sample piece and the corresponding spin–polarised electrons were injected from the EuS/Co injector side.
It is reasonable to assume that a smoother, flat interface between the GaAs and EuS would increase the injection efficiency, as rough interfaces decrease the injection efficiency [105, 117].

Untreated Substrate

To clarify the source of the defected areas on the surface, an untreated wafer piece was analysed by TEM.
The results shown in figures 5.15a and 5.15b reveal that the substrate is initially flat and smooth. However, several defects are also observed on top of its surface, which have often pyramidal/trigonal shape and are indicated by white arrows in figure 5.15a.
The single crystalline quality of the AlGaAs substrate and the amorphous state of the As capping layer are clearly seen in the HTEM image (figure 5.15b). Furthermore, a representative region of the pyramidal defects on top of the surface is depicted. The lattice fringes clearly show that the defects correspond to the two sets of (111) planes of AlGaAs and measurements of their interplanar spacing confirmed that they are identical with their counterparts in the AlGaAs substrate. Moreover, the defect and the substrate have exactly the same orientation, i.e. [011] of AlGaAs. Theoretically, the substrates are capped with a 15 nm GaAs final layer. The defects on top of the AlGaAs could indeed be formed by GaAs, possbily during the removal of oxygen and/or later during the Arsenic passivation of the surface.
Surrounding the defects, amorphous As is found with a total thickness in the range of 150 nm. Chemical analysis shows the presence of Ga, As and Al and confirms that the defect is chemically identical to the substrate underneath it. A small oxygen content is also found in the spectrum (not shown), stemming mainly from the area of the As capping layer. Also, the presence of a tiny amount of oxygen inside the AlGaAs defect cannot be entirely excluded.
The analysis of the untreated wafer shows that initially, there is no oxygen in the surface. Pyramidical As defects, which might have formed during the As passivation, are observed

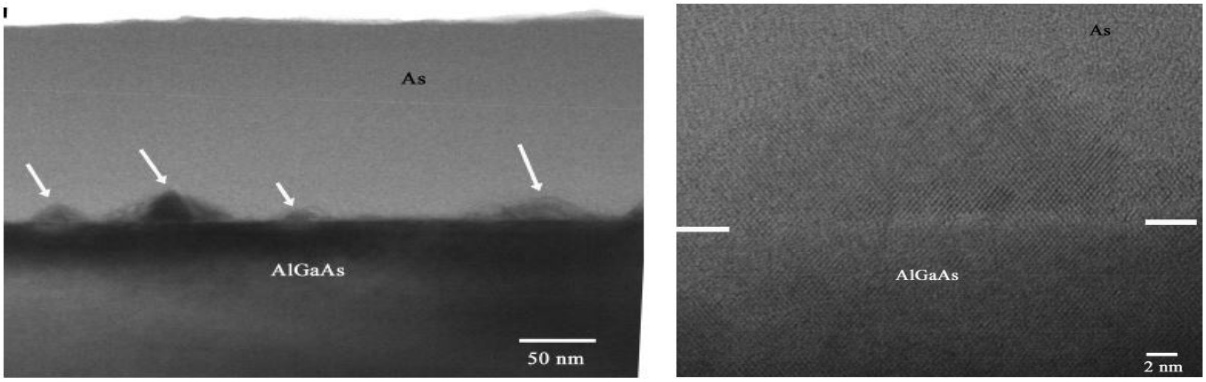

(a) TEM measurement of an untreated spin–LED substrate.

(b) HTEM measurement of an untreated spin–LED substrate.

Figure 5.15: TEM measurement of an untreated As passivated wafer.

on the surface though.

Reducing surface roughness

The most recent set of samples was prepared in the MBE growth chamber because of the much better background pressure compared to the standard Balzers evaporation chamber. Two samples were produced and their substrates heated for about 90 minutes to 250 and 400 $°C$ respectively. The two temperatures were chosen in order to test the influence on the amount of interface roughness present after evaporation.
The TEM analysis of both samples revealed that again, both samples showed rough interfaces and some defects were present in the substrate. Compared to J1–J3, the substrates were found to be smoother for the newest samples and no oxygen was observed at the interface. Still, regions with roughness, strain, structural and V–shaped defects are present and are indicated by black arrows in figure 5.16a.
Moreover, the high resolution TEM measurements revealed that the defects in the substrate are almost entirely located in the GaAs capping layer as shown in figures 5.16a, 5.16b and 5.17b. The GaAs capping layer has a thickness of about 18 nm, close to its nominal thickness of 15 nm (see figure 5.7).
Figure 5.17a shows the presence EuS located on top of the substrate, which is indicated with vertically pointed black arrows. The horizontal black arrows define the position of the film/substrate interface.
In conclusion, the most recent TEM measurements show that it was possible to reduce the amount of oxidised regions by preparing the multilayers in the MBE chamber with better vacuum. The interfaces still show roughness and defects located in the GaAs capping layer and the reason for this is still unclear. Possibly, a longer period of annealing would smoothen the GaAs after the removal of the Arsenic capping layer and lead to a smoother interface with EuS.

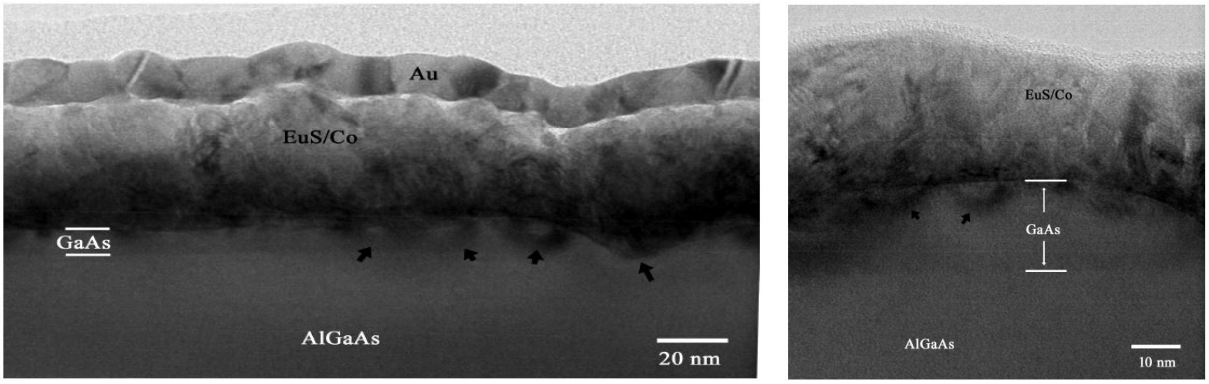

(a) TEM measurement of S202. (b) HTEM of S202.

Figure 5.16: TEM measurement of sample S202.

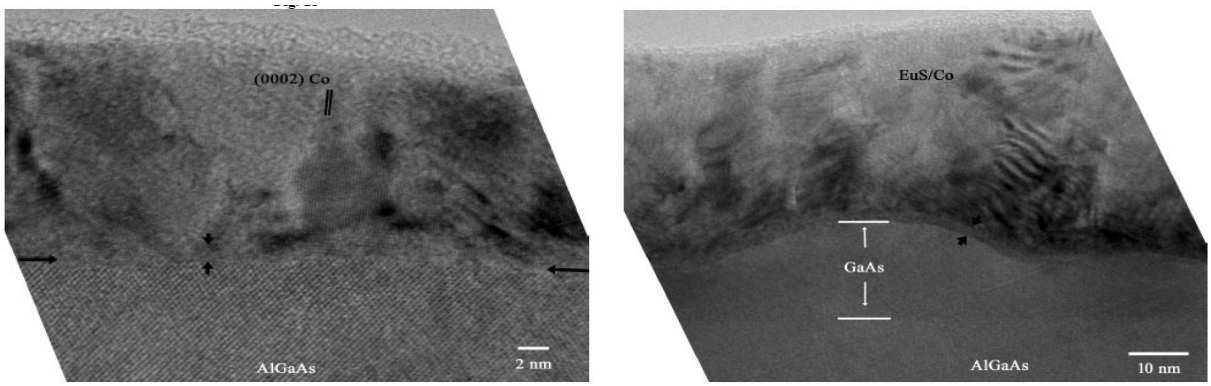

(a) HTEM of S201 (b) HTEM of S201

Figure 5.17: TEM measurement of sample S201.

5.4 Summary of Results

In this chapter the first attempts to inject spin–polarised electrons from EuS/Ni and EuS/Co multilayers into AlGaAs/GaAs–based LEDs were presented. The initital test using a multilayer of EuS/Ni together with a spin–LED and a thin AlO_x tunnel barrier showed a $P_c < 1\%$ at 5 K, which was attributed to the presence of the AlO_x barrier which most likely acted as an unwanted (and unnecessary) second tunnel barrier next to the spin–polarised tunnel barrier of EuS at 5 K, thus limiting the spin–injection.
Part of a second series of samples of EuS/Co layers on top of custom evaporated spin–LED–substrates without the AlO_x barrier showed a clear $P_c \approx 5\%$ at low temperature with applied magnetic field and in remanence. Changing the direction of magnetic field changed P_c accordingly, which is an indication that the observed effect is due to spin–polarised electrons injected into the GaAs active region. Other pieces revealed a low signal–to–noise ratio, which made the effect less clear.
RT measurements of the EL polarisation showed a low signal–to–noise ratio. Smoothing the raw data and calculating P_c did not contradict the earlier findings at low temperature. Additional TEM analysis revealed some extensive interface roughness between the spin–LED and the EuS multilayers which could account for the low degree of P_c observed at low temperature and some of the problems observed during the EL measurements. The most recent samples grown in the MBE chamber show an improvement of the surface roughness and reduction of oxygen found at the interfaces.

Chapter 6

Growth of EuS on InP(001) and InAs(001)

The growth of EuS on the two substrates InP(001) and InAs(001) is discussed in this chapter. Initial measurements of EuS grown on both substrates were collected during the course of a master thesis by Joël Griesmar [118], who was introduced to the MBE setup and personally guided throughout the time of his master thesis. Later samples, solely grown on InAs, were prepared personally.

6.1 InP and InAs

InP and InAs are two III–V semiconductors that crystallize in the *zinc–blende* structure (In and As/P fcc lattices are displaced by $^1/_4 \cdot a$ along the volume diagonal). InP has a lattice constant of $a_{InP} = 5.869$ $\mathring{A}$ and InAs one of $a_{InAs} = 6.058$ $\mathring{A}$. Both are very close in value to the lattice constant of EuS ($a_{EuS} = 5.968$ $\mathring{A}$). The misfit between InP (InAs) and EuS is only 1.7% (1.3%), which is very small and could favour epitaxial growth along the $< 001 >$ direction. Both InP and InAs have not been used as substrates for growing EuS previously.
For the initial tests of growing first EuS layers, a number of pieces cut out from commercial InP(001) and InAs(001) wafers were ordered.

After insertion into the MBE, the pieces were initially checked by AES, which revealed that the pieces had a layer of native oxide and some carbon (organic) contamination. To clean the wafer pieces, they were sputtered with Argon gas for circles of 30 minutes ($E_{kin} = 1000 - 2000$ $eV, \approx 10$ μA emission current) and repeatedly checked by AES afterwards. It was found that sputtering for about one hour rendered a clean InP (InAs) surface. The wafer pieces were annealed at 300 $°C$ for 30 minutes afterwards. Exemplary, an AES measurement is shown before and after the cleaning process for an InP wafer piece

in figure 6.1. The different elements found in the spectrum are indicated by arrows. After sputtering and subsequent annealing of the surface, the oxygen and carbon contaminations are no longer observed.

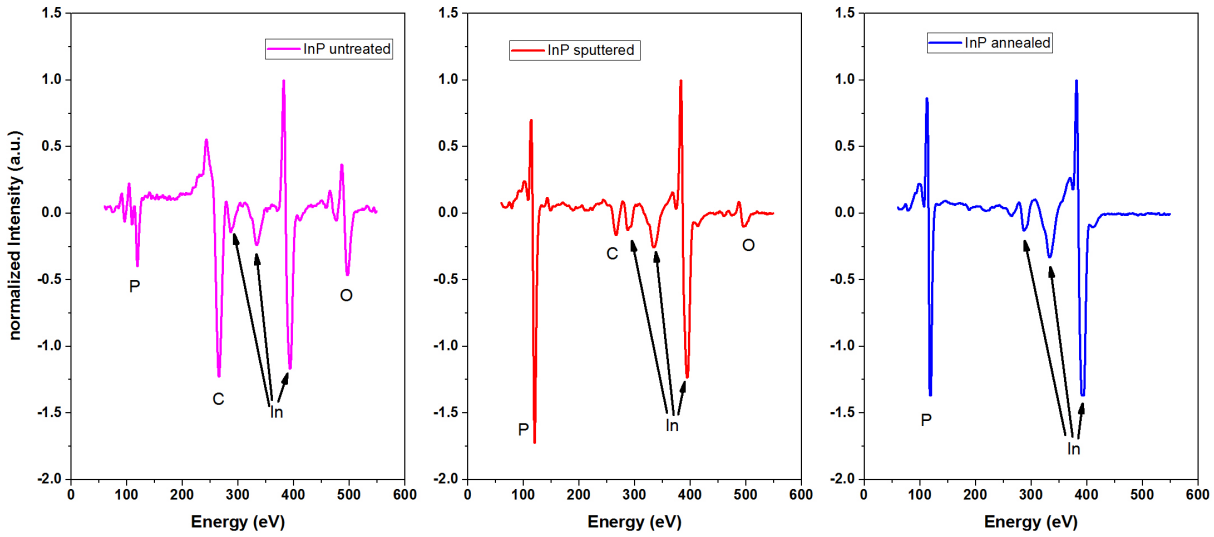

Figure 6.1: AES measurement of an InP substrate before and after the cleaning process. The different elements are indicated by arrows. After sputtering and annealing the wafer, no oxygen or carbon peaks are found and the substrate is clean.

Subsequently, the InP (InAs) substrates were investigated by low–energy–electron–diffraction (LEED). Both substrates show surface reconstructions, that depend on the elements which terminate the surface, i.e. In–terminated surfaces will show a 4x2/c(8x2) reconstruction and As (P) terminated surfaces show a 2x4 reconstruction [119, 120].
Typical LEED results for clean InP and InAs substrates are shown in figure 6.2 in logarithmic scale. The patterns were recorded for incident electron energies of 72 eV. The surface reconstruction is clearly visible. Along the y–axis, the four times larger surface unit cell is observed, while the two times larger cell is seen along the x–axis. In figure 6.2b the reciprocal length a* and the four–times larger unit cell are indicated.
The electron beam's diameter is in the μm regime and hits a comparably large area of the sample. In this area, both types of surface reconstruction, i.e. the 4x2 and c(8x2), are found in different domains and appear superimposed in the LEED. Therefore, the spots originating from the four–times and eight–times larger unit cells appear very close together and every second row of spots appears smeared out.

Figure 6.3 shows the two individual LEED patterns of a 4x2 and a c(8x2) reconstruction to further clearify this. When both patterns are superimposed, the experimentally observed pattern is seen. The observation of this reconstruction pattern suggests In–terminated substrates after cleaning.

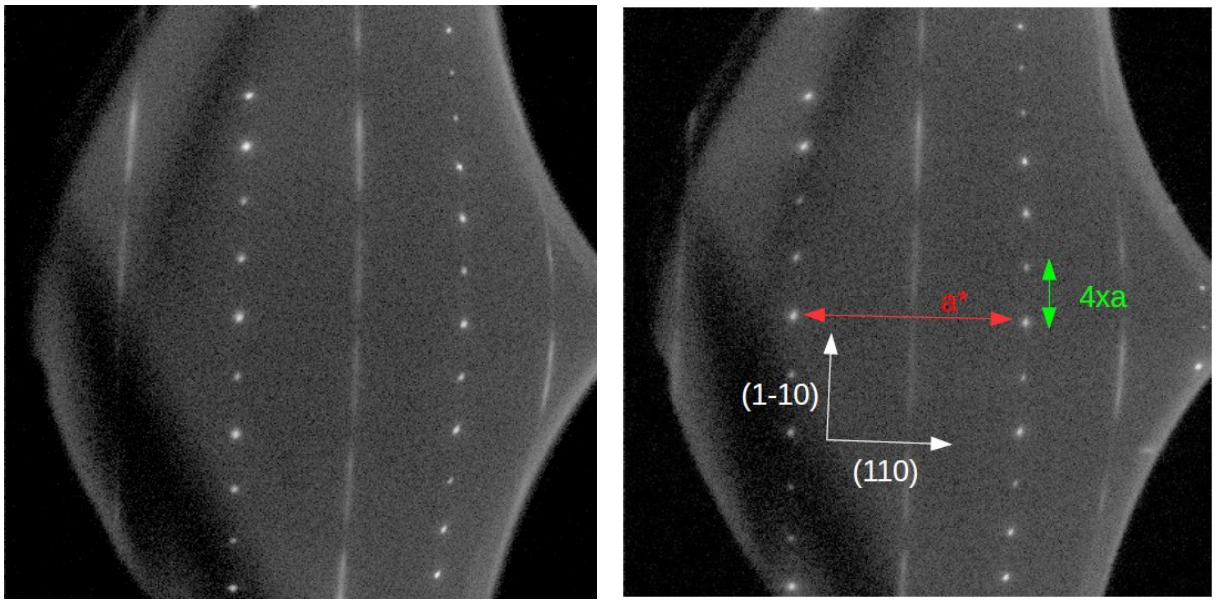

(a) InP Leed 72 eV (b) InAs Leed 72 eV

Figure 6.2: LEED at 72 eV of InP and InAs.

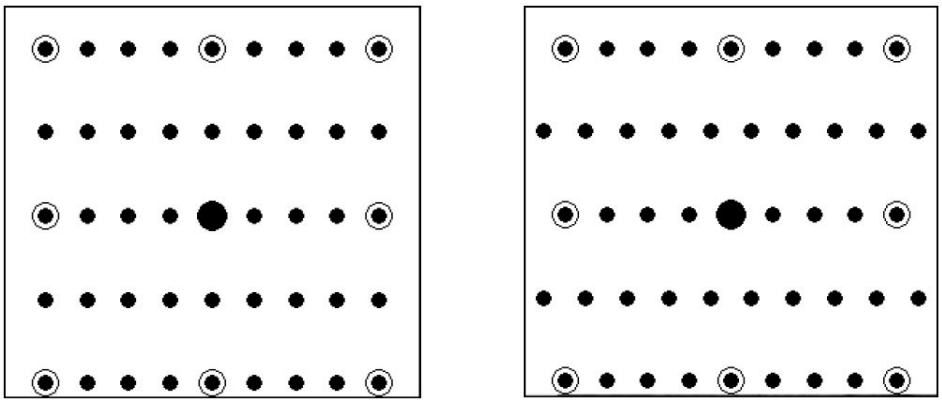

(a) 4x2 surface reconstruction (b) c(8x2) surface reconstruction

Figure 6.3: Different surface reconstructions. a) 4x2 surface reconstruction. b) c(8x2) reconstruction.

Length conversion

The distances in the LEED scans are typically given in the deflection voltages. One usually wants to convert the distances in k–space observed in LEED to real lengths. For this reason, a conversion factor between the length observed in Volts and the 'actual' reciprocal length is needed. Due to the LEED optics this conversion factor is not the same for all energies.
One way of getting the right conversion factor is to measure a standard surface at a given energy (in this case the 7x7 reconstruction of Si(111)), where the distances in real space are known. If a new structure, e.g. EuS deposited on InAs or InP, is observed at the same energy one can then calculate the real length between two spots. The so calculated real length of the spot distances were 4.14 and 4.29 $\mathring{A}$ for InP and InAs respectively. These values correspond to the nearest–neighbour distance of two In atoms on the surface, i.e. $\frac{a}{\sqrt{2}}$, the distance of two In atoms along the surface diagonal of the unit cell. Both values agree well with the theoretical values expected for the InP and InAs surface unit cells.

6.2 EuS films

A number of samples with different EuS thickness and growth temperature were prepared on the cleaned InP substrates. After each deposition process, the films were checked by AES and SPA–LEED.
Unfortunately, due to continuous problems with the in–situ combined AFM/STM setup, it was not possible to investigate the surface of the evaporated films *in situ*. Some samples however, could be measured in an *ex situ* AFM setup.
Initially, the growth of samples was centered around growing EuS on InP and InAs at RT, so the majority of the samples was produced at around 23 $°C$, while some samples were additionally evaporated at higher substrate temperatures. The evaporated thickness was checked by a quartz microbalance located in the vicinity of the sample holder inside the chamber. The conversion factor (tooling factor) linking the actual film thickness on the substrate with the one displayed on the quartz balance was known from earlier calibrations. These calibrations are usually done with thick films, from which the tooling factor is calculated. Usually, the films deposited are thin or at least thinner than the calibration samples. In a first approximation, the tooling factor is taken to be constant for every thickness. This does not necessarily have to be the case. Generally, when referring to the film thickness, the thickness calculated by quartz balance display and tooling factor is meant and the real thickness might deviate within a few percent of this value.

6.3 Results on InP

AES and SPA-LEED

The AES measurements of the films show the characteristic Eu, S, In and P peaks for EuS films as shown in figure 6.4. Here, the AES signal is plotted for samples evaporated at RT. The In and P peaks are decreasing in intensity for increasing EuS thickness. Likewise, the S and Eu peaks are increasing and reach saturation after a films thickness of about 4 nm. A small In peak is still detectable at a thickness of 4 nm but has clearly disappeared for 8 nm and thicker films.

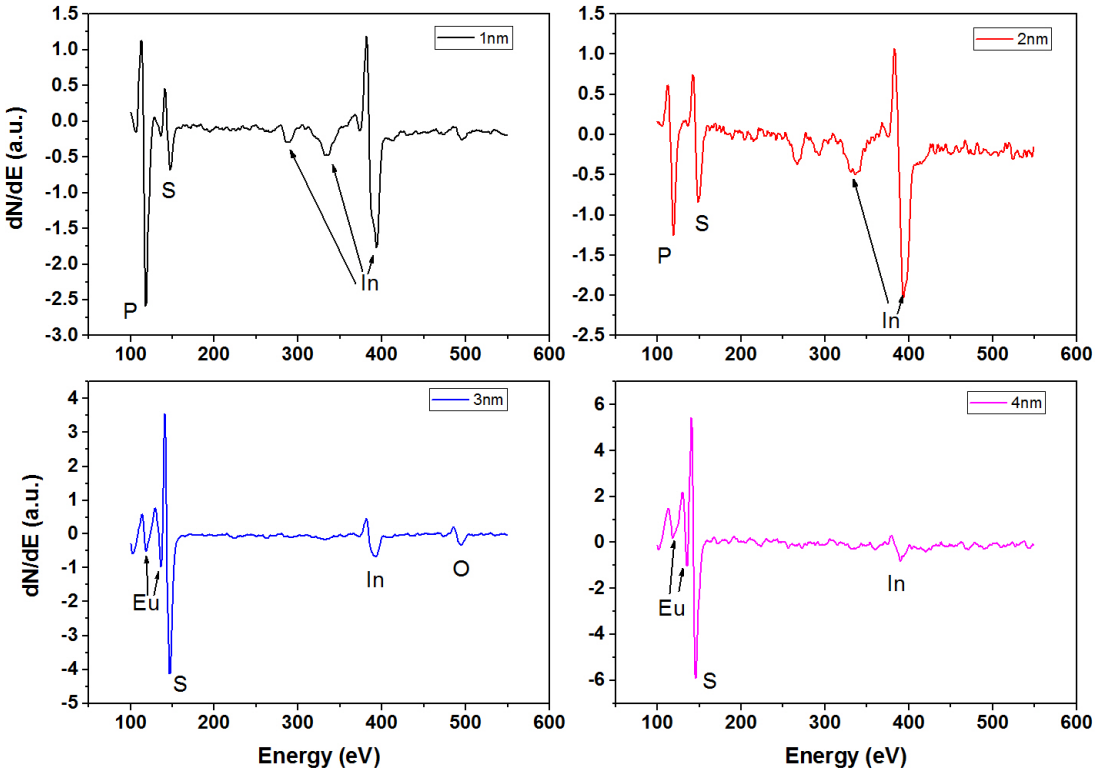

Figure 6.4: AES measurements of EuS films grown on InP(001) at RT.

The intensity of Auger peaks is related to the amount of material present on the surface [121]. For a cleaned InP (or InAs) sample, the In peak intensity will be saturated. With increasing amount of material deposited, the peak intensity will decrease, until it is no longer observable.
In figure 6.5 the In intensity is plotted over the deposited EuS thickness for films grown at 100 $°C$ substrate temperature. The experimental data is compared with two models:

$$I_{In,1} = I_{In,sat} \cdot exp(-\frac{d}{\lambda_{In,EuS} \cdot cos(\theta)}) \quad (6.1)$$

$$I_{In,2} = I_{In,sat} \cdot (1-x) \cdot exp(-\frac{d}{\lambda_{In,EuS} \cdot cos(\theta)}) + x \cdot exp(-\frac{d+h}{\lambda_{In,EuS} \cdot cos(\theta)}) \quad (6.2)$$

Here, $I_{In,sat}$ is the saturated intensity of the pure bulk In, d is the homogeneous thickness of the film, x the percentage of substrate area covered with islands, h the island height, θ is the emission angle of the electrons with respect to the surface normal and $\lambda_{A,B}$ is the attenuation length of Auger electrons in material B when emitted by material A. In the typical Auger measurement, the electrons are emitted quasi perpendicular to the surface, so that $cos(\theta) = 1$. $\lambda_{In,EuS}$ was calculated by free software from the N.I.S.T. [1] using parameters of bulk EuS for the film, giving $\lambda_{In,EuS} = 1.123\ nm$.

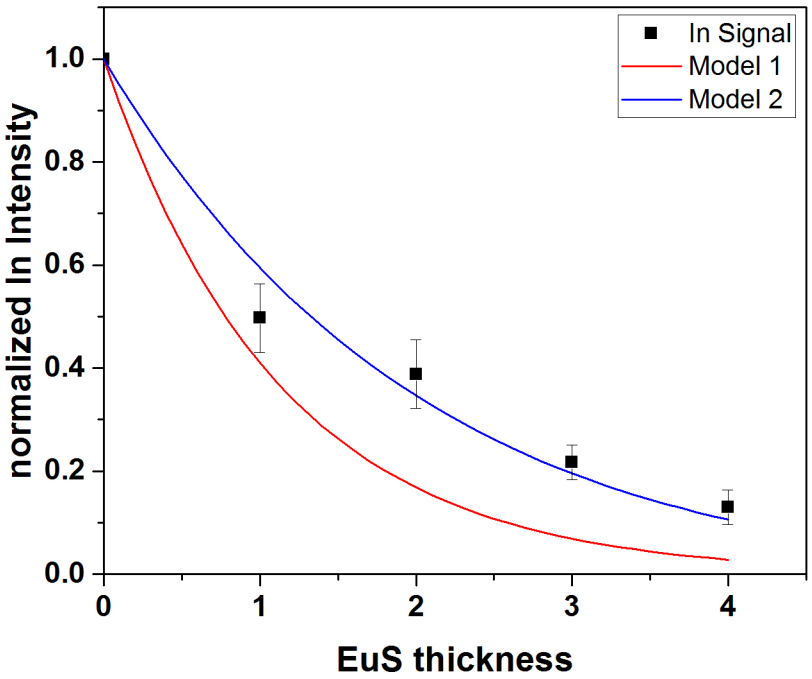

Figure 6.5: Normalized AES In intensity of thin EuS films grown on InP(001) at 100 $°C$.

Model 1 (equation 6.1) assumes a constant thickness d of EuS on top of the substrates. In this case, d would correspond to the value given by the quartz balance and the coverage would be homogeneous, i.e. FM growth. Model 2 (equation 6.2) assumes layer plus island growth (i.e., Stranski–Krastanov–like growth). In this model a homogeneous thickness is assumed to cover the entire substrate area and the fraction area x is covered with islands with constant height h. The overall deposited material as measured by the quartz balance adds a restriction to the values that x, d and h can assume:

[1] National Institute of Standards and Technology

$$d_{quartzbalance} = d + x \cdot h \tag{6.3}$$

For model 1 the film thickness was set to the thickness given by the quartz balance. For model 2 the values of d and x were linearly increased with the amount deposited (i.e. $d = 0.43 \cdot d_{Quartzbalance}$ and $x = 0.13 \cdot d_{Quartzbalance}$). With these values the homogeneous thickness for the thickest films (i.e. 4 nm deposited amount) was 1.76 nm and the amount of film covered with additional islands 52%. The height of the islands would amount to 4.4 nm for these values.
The general conclusion that can be drawn from the two models is that EuS does not grow layer by layer. Instead, it appears that there is some homogeneous coverage of the substrate, together with island growth (Stranski–Krastanov–like growth).
Model 2 used to fit the experimental data is quite simple and only takes into account two different layers, i.e. one with homogeneous coverage and a second layer composed of islands with the same height. Of course, models taking even more layers and different heights into account would be better suited to describe the experimental findings, however, this would not change the general conclusion of a non–flat surface with islands and different layer heights, drawn from these two models.

The LEED scans of samples grown on InP further solidify this picture. For samples with 1 and 2 nm EuS thickness, the observed LEED spots are quite sharp, but considerably broadened with increasing thickness. The electron energy was 72 eV, which corresponds to a in–phase relation considering a step height of one atomic layer of EuS in (001) direction, i.e. 2.98 $\mathring{A}$.
The broadening of the LEED spots points to increasing surface roughness with the amount deposited and a fast decrease of transfer length which could be due to small island structures formed by EuS. For EuS films of 1 nm the surface reconstruction of InP is weekly observed which also points to areas which are not covered by EuS.
No surface reconstruction of EuS is known and none is observed so that the LEED pattern corresponds to a simple 1x1 pattern. Figure 6.6 shows the LEED measurements of a set of EuS films on InP to show the evolution of the spot size.

The observation of LEED spots shows the presence of a largely ordered crystalline surface. The spots must originate from a crystalline layer of EuS for two reasons: One, the spots are observed for all samples, even the ones with very large thickness. Second, LEED is a surface sensitive technique with probing depths of only a few tens of Angströms. The AES measurements show that no substrate signal is seen for thicker films than 4 nm EuS, which suggests a (in part) homogeneously covered surface. If this surface was amorphous, no spots would appear.

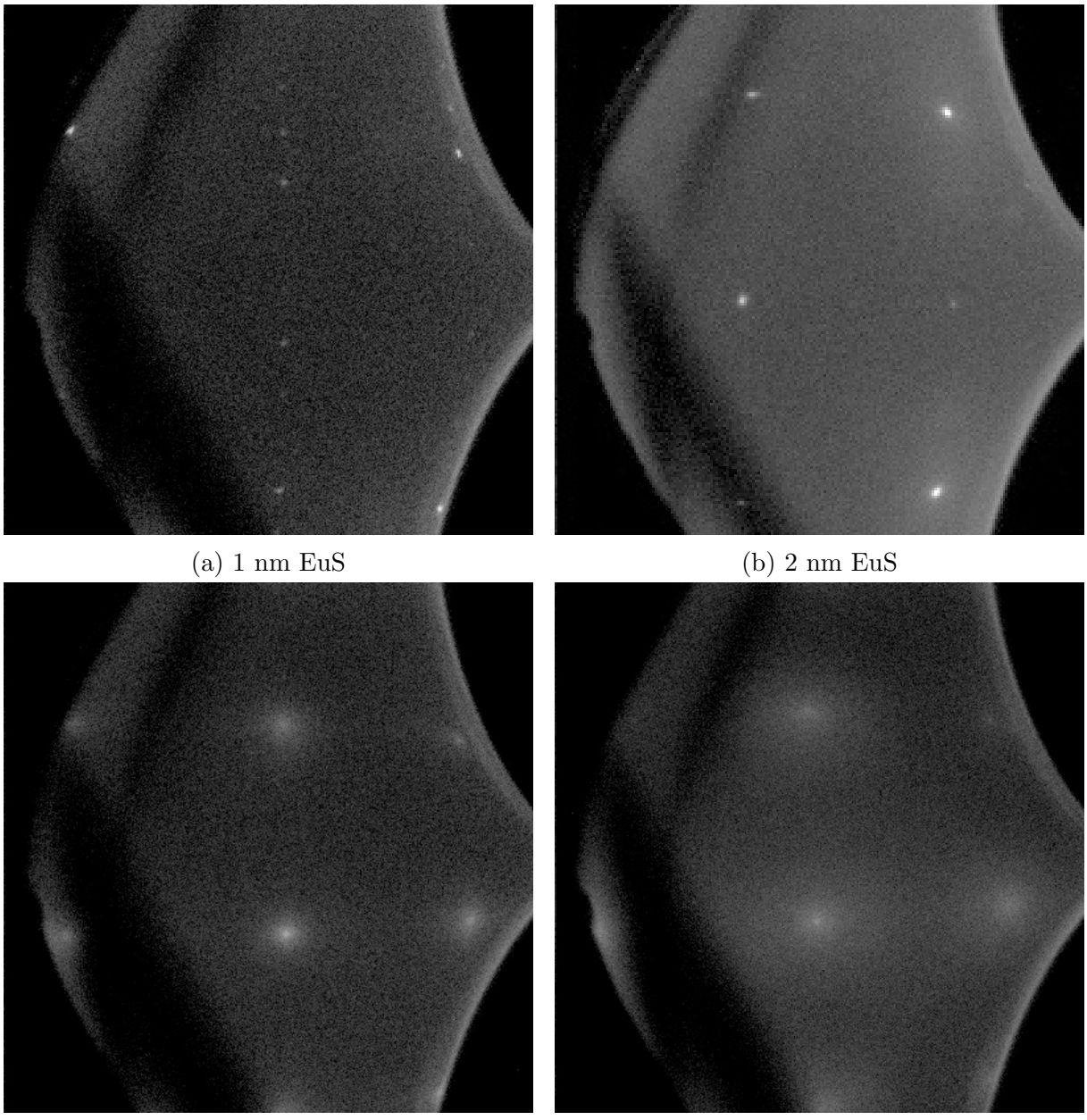

(a) 1 nm EuS

(b) 2 nm EuS

(c) 3 nm EuS

(d) 4 nm EuS

Figure 6.6: LEED patterns of EuS films on InP(001) recorded at 72 eV. The patterns are shown in logarithmic scale.

The Full Width Half Maximum (FWHM) of the (00) spots of each sample is shown in figure 6.7. For this, line profiles along the (110) direction were taken of the (000) spot and divided by the length of the Brillouin zone. As is evident, there is an increase of the spot size with increasing EuS thickness. The spots size also increases for increased substrate temperature.

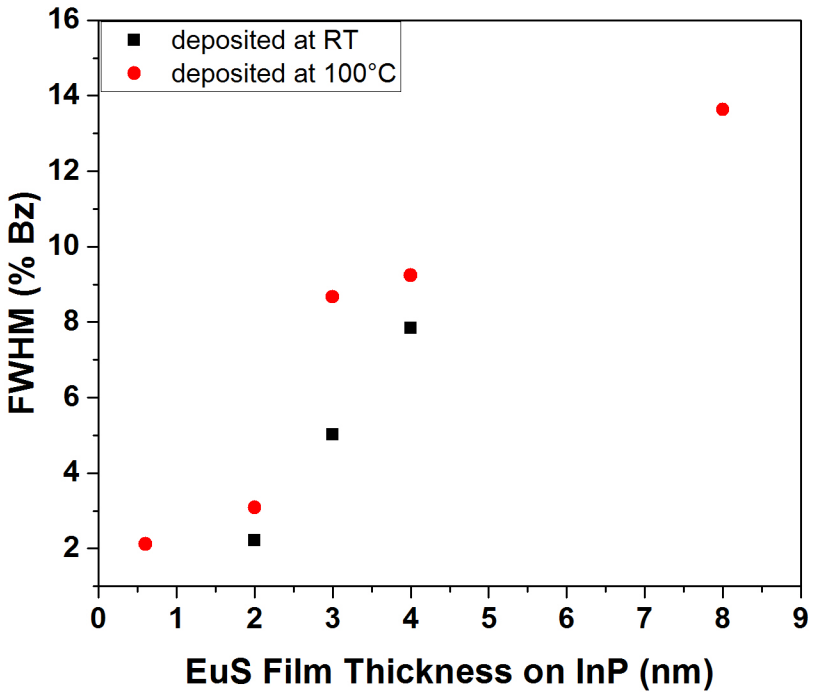

Figure 6.7: FWHM of EuS films on InP deposited at different substrate temperatures. The broadness of the spots increases with film thickness. A clear temperature influence can not be extracted from the data.

AFM

The combined STM/AFM in the MBE was largely inoperable during the time of this thesis. The results that have been obtained using the STM/AFM setup are questionable and mostly unreliable. Therefore, no *in situ* characterization of the samples was possible. It was possible to measure some samples in an *ex situ* AFM. These results will be presented for EuS films on InP and InAs.

AFM measurements of a 4 nm EuS film on InP(001) deposited at RT are shown in figure 6.8. The scans show areas of 1 μm x 1 μm and 2 μm x 2 μm. The surface is not smooth and generally shows a ragged, island–like structure. Line profiles of the two scans reveal island sizes of $50 - 100$ nm size with heights between 1 nm and 4 nm found in the

1 μm x 1 μm scan and larger heights of up to 6 nm appearing less frequently in other areas of the sample as shown in figure 6.8b.

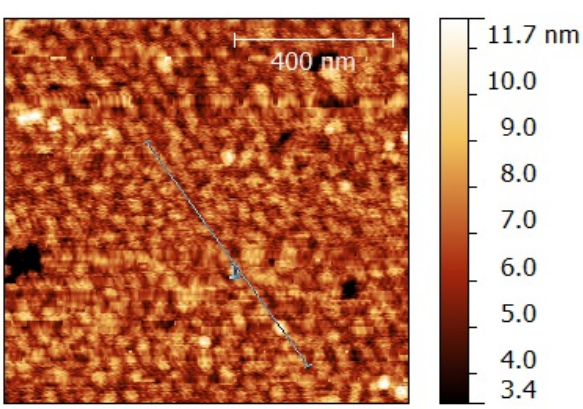

(a) 1 μm x 1 μm scan of 4 nm EuS deposited on InP

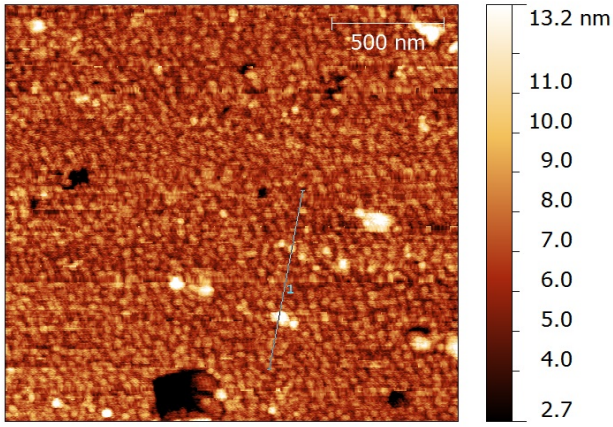

(b) 2 μm x 2 μm scan of 4 nm EuS deposited on InP

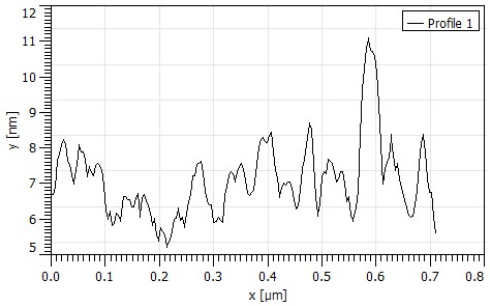

(c) Line profiles of 1 μm x 1 μm scan of 4 nm EuS deposited on InP

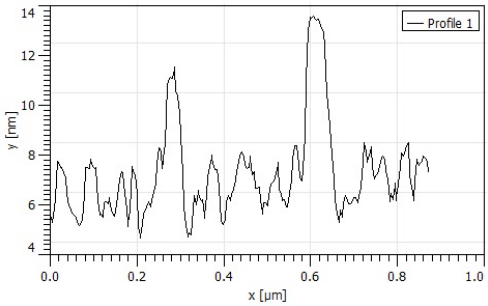

(d) Line Profiles of 2 μm x 2 μm scan of 4 nm EuS deposited on InP

Figure 6.8: AFM measurements of a 4 nm EuS film on InP deposited at RT. The surface shows small islands which appear randomly distributed. Their heights differ between 1 and 4 nm. Even larger heights of up to 6 nm are found in the 2 μm x 2 μm scan (b) but appear less frequently.

In conclusion, the SPA–LEED and AFM measurements of EuS films deposited on InP(001) show evidence of a mixed layer– plus island–growth and suggest the formation of EuS layers with considerable roughness.

6.4 Results on InAs

AES and SPA-LEED

All samples deposited on InAs(001) were also measured by AES and analysed by SPA–LEED after deposition and in some cases ex–situ AFM measurements were performed. The Auger spectra of films with EuS thickness of 4 nm and below show the presence of Eu, S and In in the energy range between 50 eV and 550 eV. The Arsenic peaks around $50 - 100$ eV are suppressed by the more intense Eu peaks and are therefore usually not observed. For EuS films thicker than 4 nm no In peaks were observed, so that the homogeneously covered area of the substrate is thick enough that all intensity from the substrate is surpressed. The evolution of the Auger spectra for films grown on InAs at RT is shown in figure 6.9.

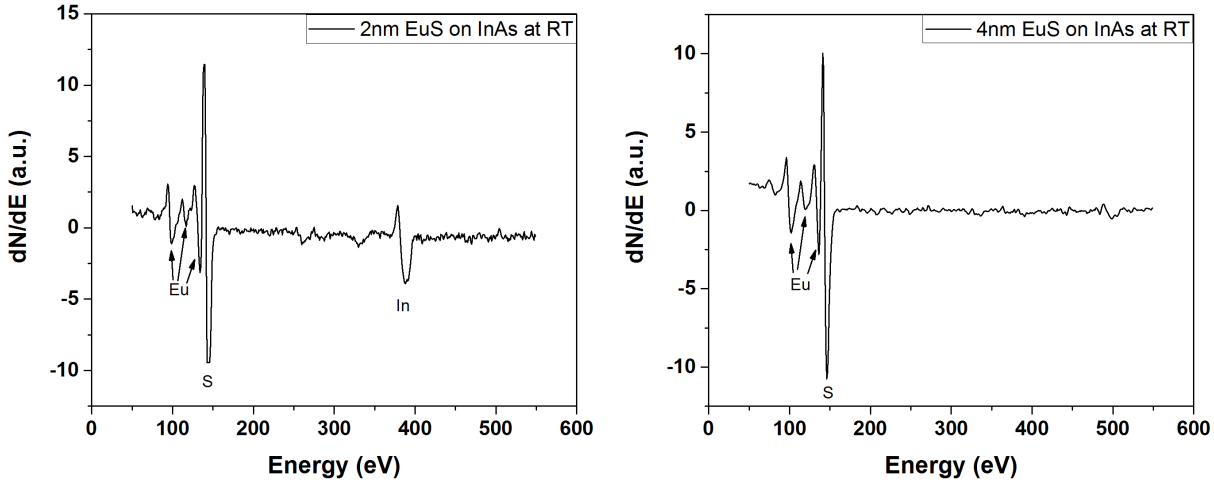

(a) 2 nm EuS on InAs (b) 4 nm EuS on InAs

Figure 6.9: (a) 2 nm EuS deposited on InAs at RT. Eu, S and In are observed in the spectrum. (b) 4 nm EuS film deposited on InAs at RT. The In signal is no longer observable which suggests a homogeneous coverage of the surface that is large enough to surpress the substrate signal.

In the LEED patterns of samples with EuS thickness of 1 nm and below, the initial InAs surface reconstruction is still visible, though the intensity of the spots located at the (1x1) positions is about one order of magnitude higher. The surface reconstruction is no longer observed for films with thickness of 2 nm and more.
LEED patterns of films grown at RT are shown in figure 6.10. The films seem to have equally sharp spots (even for EuS thickness up to 10 nm), while films grown at higher temperature show a different behaviour: For energies corresponding to an in–phase condition (≈ 70 eV) the (00) and (11) spots appear sharp, while the (10) spots appear quite broad. This is illustrated in figure 6.11.

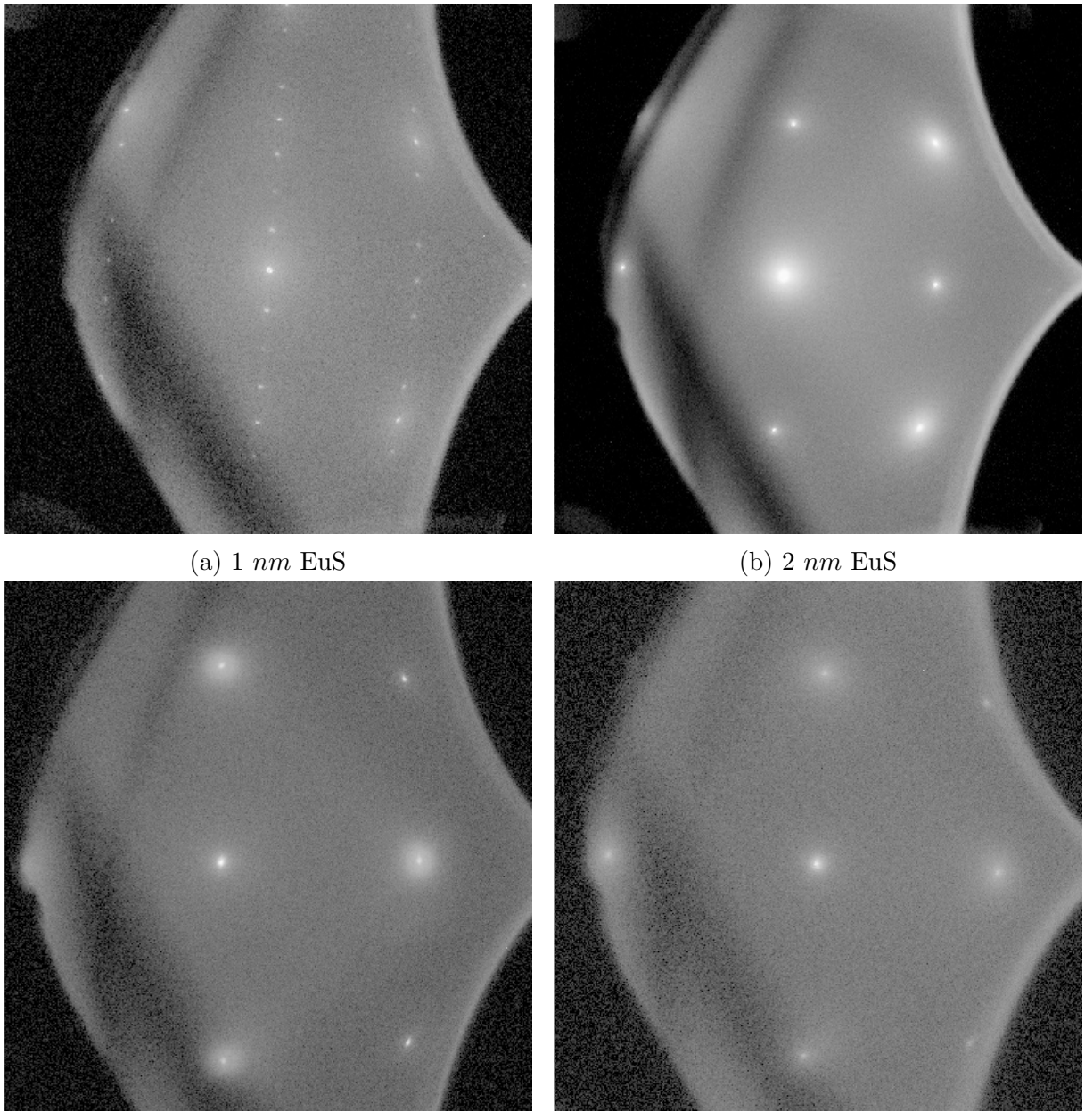

(a) 1 nm EuS (b) 2 nm EuS

(c) 4 nm EuS (d) 10 nm EuS

Figure 6.10: LEED patterns of EuS films deposited at RT on InAs(001) recorded at 72 eV. The patterns are shown in logarithmic scale.

As in the case of EuS deposited on InP, the LEED spots observed on samples grown on InAs also stem from crystalline EuS layers. The reasoning is in principle the same as for samples grown on InP.
Equally sharp spots are an indication of a largely flat surface with minimal surface roughness. A very rough surface would broaden all spots, as was found for thicker films deposited on InP. If more than one atomic layer is probed by the electron beam, a third periodicity in z–direction has to be fulfilled (3rd Laue condition) in order to see a maximum of constructive interference, i.e. sharp LEED spots. As seen from figure 2.9 one can generally discern between the influence of two atomic layers, stepped surfaces and many atomic layers. This can be done by varying the energy of the incoming electrons, i.e. changing the scattering factor S.
Therefore, a 4 nm EuS film evaporated at 300 $°C$ substrate temperature (sample X4), was measured with varying electron energies. The LEED patterns for in–phase (70 eV, $S = 4.0$) and out–of–phase (85 eV, $S = 4.5$) condition are shown in figure 6.11.
Spot profiles were measured of the (00) spot of a 4 nm EuS film, evaporated at 300 $°C$, along the (110) direction and are plotted in figure 6.12a. Figure 6.12b shows the maximum intensity of the (00) spot for each electron energy. A clear oscillation between maximum intensity for integer values of S can be seen, while minima are observed for the out–of–phase condition. The oscillations clearly show that the LEED spot intensities are collected from several surface layers. No shoulders appear in the line profiles for the out–of–phase condition, which would be expected if only two atomic layers would contribute to the intensity. Therefore, more than two layers are involved which points to a randomly stepped surface with unequal step sizes.
The reason why the sharpness of the (00) and (10)/(01) spots changes with incident energies is the following: If more than one layer is observed, the reciprocal lattice rods that cut the Ewald sphere are no longer equally sharp (resulting in equal intensity and spot sharpness) but resemble something similar to a 'pearl necklace' (see figure 2.9) The thin parts of this 'necklace' correspond to points were the 3rd Laue condition is fulfilled and the spots appear sharp, if the Ewald sphere cuts rods at these points. If the rods are cut at a thicker part, the spots will appear quite broad and the intensity will be smeared out. For a given energy (and scattering phase) the Ewald sphere cuts different rods at different points of the 'necklace', resulting in different spot broadness. Varying the energy for a fixed point will move the Ewald sphere along this point's rod and broaden and sharpen the observed spot periodically. Likewise, other spots will appear sharp and broad periodically.

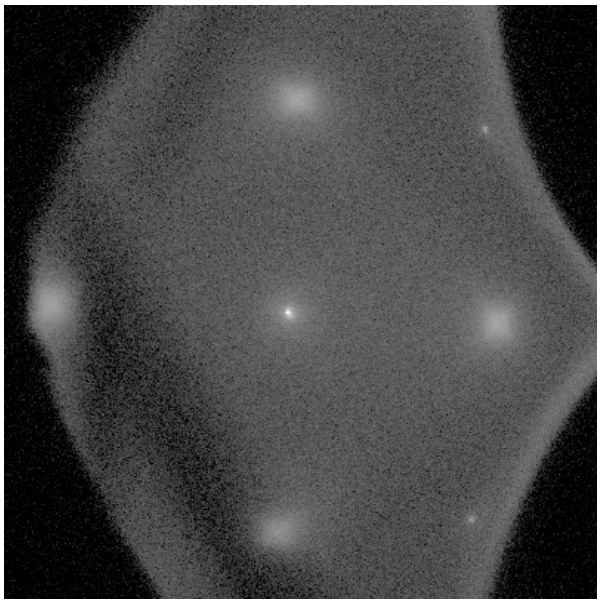

(a) 4 nm EuS deposited at at at 300° C, measured at 70 eV.

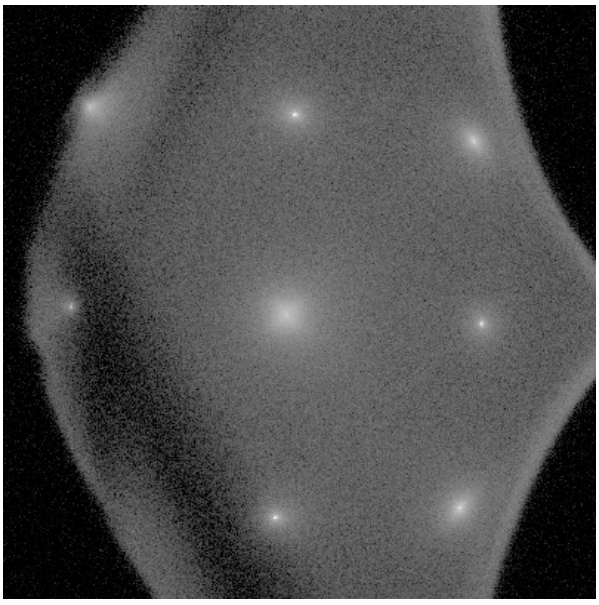

(b) 4 nm EuS deposited at at at 300° C, measured at 85 eV.

Figure 6.11: LEED patterns of sample X4 recorded at 70 eV and 85 eV. The patterns are shown in logarithmic scale. (a) shows a sharp (00) spot due to the in–phase condition of the incident electron energy. The (10) and (01) spots appear quite broad. In (b) the incident electron energy fulfills the out–of–phase condition, so the (00) spot is quite broad. Simultaneously, the (01) and (10) spots appear sharp, because they are in–phase.

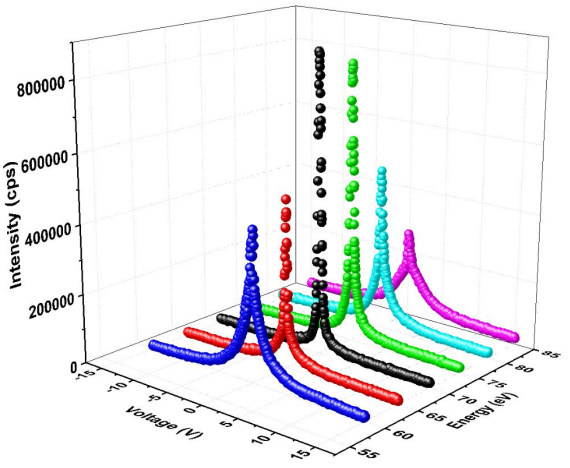

(a) Line profiles along the (110) direction of the (000) spot of a 4 nm EuS film deposited at 300°C

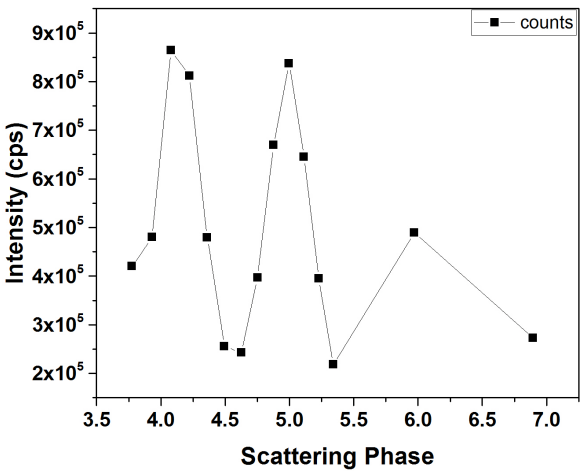

(b) (000) spot intensity for different scattering phases

Figure 6.12: SPA–LEED analysis of 4 nm EuS film deposited at 300° C on InAs. (a) Line profiles of the (000) spot along the (110) direction for different energies (scattering phases). (b) Oscillation of the (000) peak intensity for different scattering phases.

A series of EuS films grown at substrate temperatures of 300° C all show this behaviour of sharp (00) spot and broad (10)/(01) spots for integer values of the scattering phase. Some samples showed a structured diffuse peak rather than just a diffuse round peak. This structure resembles a cross and is indicated exemplary in figure 6.13. This points to larger structures, maybe elongated rectangularly shaped islands. These would show sharp spots corresponding to the long side of the rectangle and broad spots for the short side. The cross–like appearance would then be due to these elongated structures growing in different domains on the surface, which would be equally observed and mixed in the LEED pattern. This would be similar to the mixing of the 1x2 and 2x1 Si(001) surface reconstructions, which also appear superimposed in their typical LEED pattern [53, 122]. Similar cross–like structures have indeed been observed experimentally for elongated island growing on Si(001) [123].

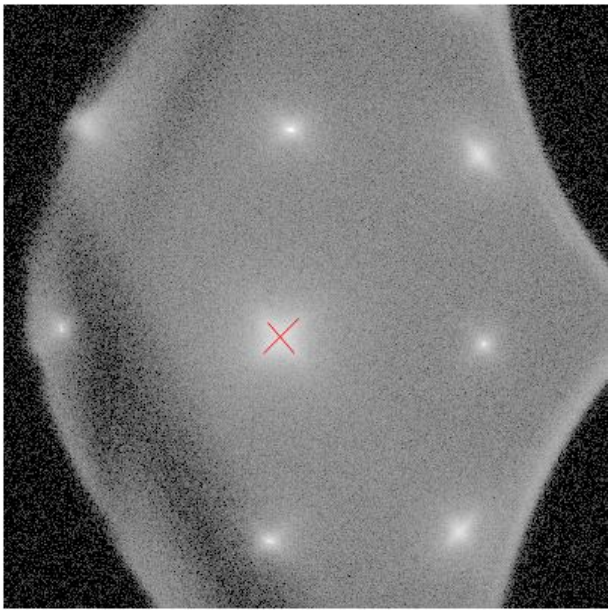

Figure 6.13: LEED pattern of a 10 nm EuS film deposited at 300° C recorded at 85 eV ($S = 4.5$). The (00) spot appears structured in the form of a cross.

As a measure of the sharpness of the (00) spots, their FWHM is shown for all samples grown on InAs in figure 6.14. The spot size increases with increasing thickness but is generally smaller compared to spots observed on InP (see figure 6.7). A clear temperature trend cannot be seen. Generally, the FWHM of the spots for EuS films up to 4 nm is below 3% of the Brillouin zone.

Overall, the growth of EuS seems to be smoother on InAs judged by the LEED scans which show clear spots even for films with very large thickness of up to 20 nm. The spot half–width of a 20 nm EuS films deposited on InAs at RT (8% Brillouin zone) is comparable to a 4 nm film deposited on InP at RT (see figure 6.7).

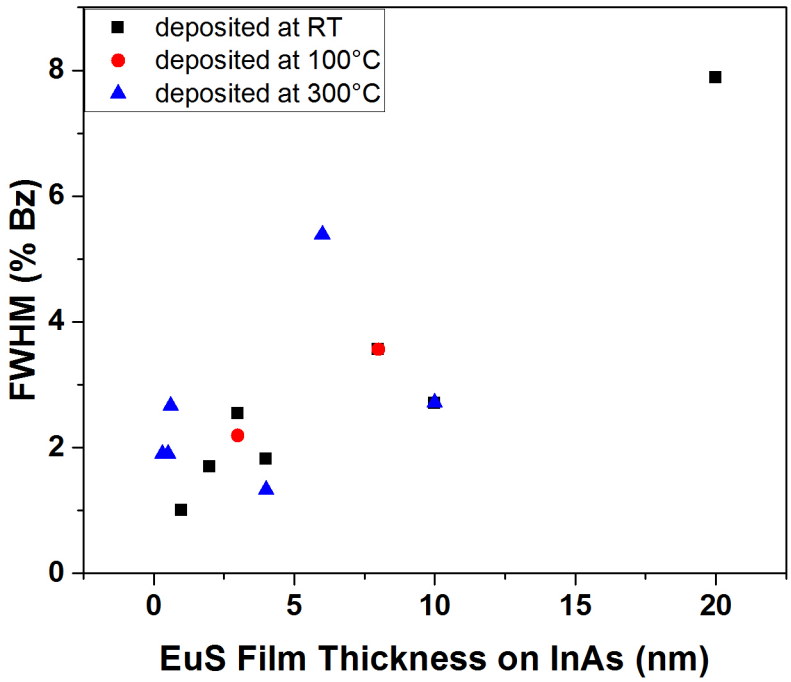

Figure 6.14: FWHM of EuS films on InAs deposited at different substrate temperatures. The broadness of the spots increases with film thickness. A clear temperature influence can not be extracted from the data.

AFM

AFM measurements of a 2 nm EuS film deposited at 100 $°C$ and a 4 nm film deposited at RT are shown in figure 6.15. Larger smooth areas are observed on both samples with occasional high structures. Line scans on these, show a height between 3 nm and 5 nm with a width of about 50 nm. The smoother areas are several hundreds of nanometers wide and show height differences in the order of half a nanometer. This is very close to one or two atomic layer distances in EuS along the (001) direction, i.e. 2.98 $\AA$ and 5.96 $\AA$. The AFM results agree well with the observation made by LEED and indeed suggest a generally smooth growth of EuS on InAs. No clear temperature effect can be deduced from the AFM measurements which is due to the limited number of samples that were checked by AFM.

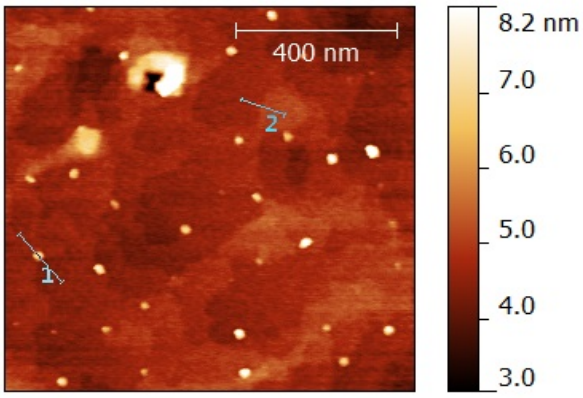

(a) 1x1 μm scan of 2 nm EuS deposited on InAs at 100 $°C$

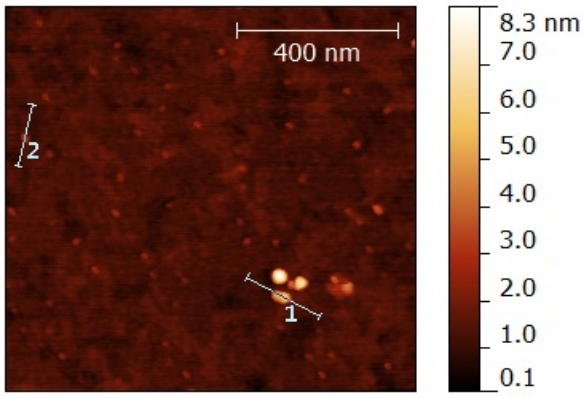

(b) 1x1 μm scan of 4 nm EuS deposited on InAs at RT

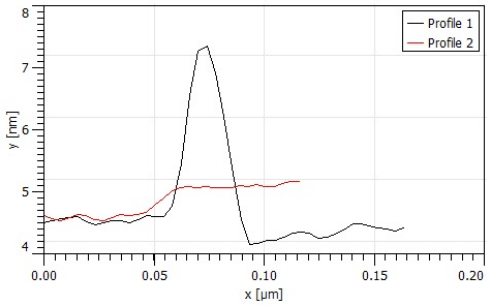

(c) Line profiles of 1x1 μm scan of 2 nm EuS deposited on InAs at 100 $°C$

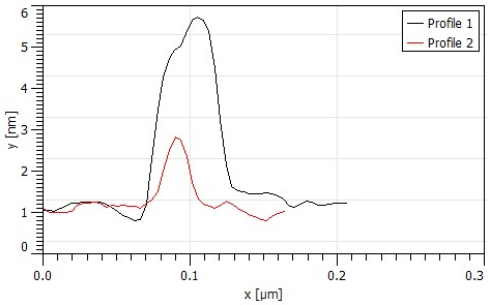

(d) Line Profiles of 1x1 μm scan of 4 nm EuS deposited on InAs at RT

Figure 6.15: (a) AFM measurement of a 2 nm EuS film on InAs deposited at 100 $°C$. (b) Line profile taken from (a). (c) AFM measurement of a 4 nm EuS film on InAs deposited at RT. (d) Line profile taken from (c).

TEM of two 10 nm EuS film

Two 10 nm EuS films were deposited on InAs, one at RT (sample X8), the other at 300 $°C$ (sample X9). Both were analysed by TEM.

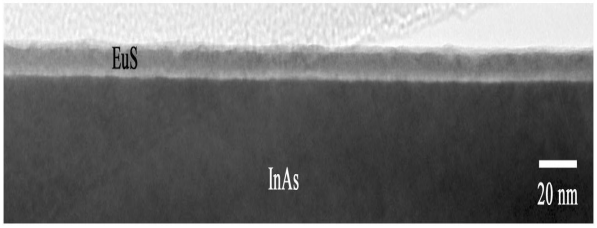

(a) TEM of sample X8

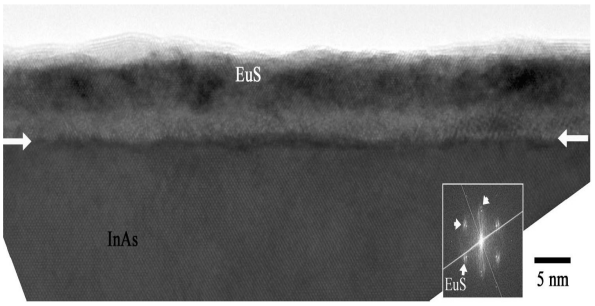

(b) HTEM of sample X8. The EuS/InAs interface is indicated by white arrows. The inset show the Fourier transformation of the image.

Figure 6.16: TEM of sample X8

Sample X8 shows a smooth, flat EuS film on the generally flat InAs substrate as shown in figure 6.16a. Some small oxidised areas at the interface were observed in higher resolution scans (not shown). The average EuS film thickness is 8.8 nm and slightly below its intended value of 10 nm. The average surface roughness in the EuS layers is 0.8 nm. The smooth and flat EuS layer agrees well with the conclusions drawn from the SPA–LEED analysis, i.e. smooth and flat growth of EuS on InAs at RT.
Figure 6.16b shows a HTEM measurement of X8. The EuS/InAs interface is indicated by white arrows. The EuS layers were prone to damage by the electron beam and became amorphous within minutes after exposure. Part of the oxidised regions is visible on top of the substrate in figure 6.16b. Nonetheless, the EuS layers show crystalline ordering and reveal epitaxial growth of EuS on InAs. The inset in figure 6.16b shows the Fourier transform of the image. The Fourier transformation shows the expected InAs reflections as well as the additional EuS reflections (indicated by small white arrows).
High resolution scans of X8 also revealed the presence of oxidised Eu crystallites, which were attributed to Eu_2O_3. Chemical analysis revealed that the Eu/S ratio is larger than 1, which corroborates the existence of oxidised Eu phases.

Sample X9 also shows a smooth EuS/InAs interface, indicated by white arrows in figure 6.17a. The average EuS thickness is 8.2 nm, which is also slightly less than the intended 10 nm. The roughness found in the EuS film is 1.5 nm and almost a factor of two higher compared to X8. The increased surface roughness agrees with the observation made by SPA–LEED, that the surface roughness in EuS layers increases with increasing substrate

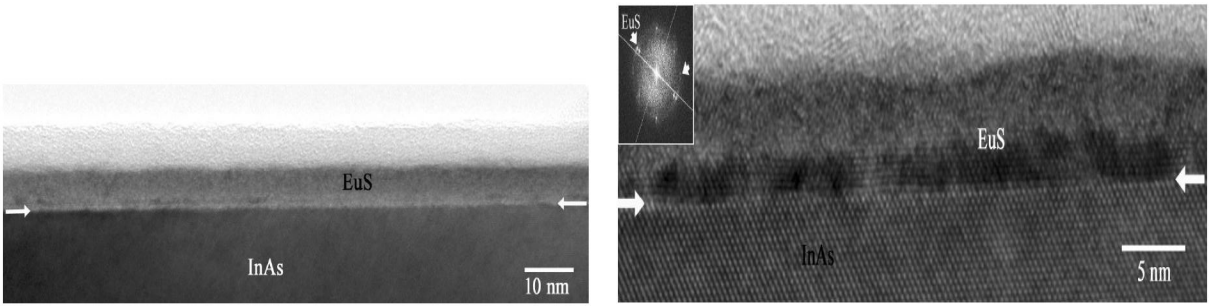

(a) TEM of sample X9

(b) HTEM of sample X9. The EuS/InAs interface is indicated by white arrows. The inset show the Fourier transformation of the image.

Figure 6.17: TEM of sample X9

temperature.

Sample X9 does not show larger defected or oxidised areas, though chemical analysis revealed the same lack of sulfur and an increased oxygen amount in the EuS layers, which suggests the formation of Eu–oxides.

The HTEM image of X9 shown in figure 6.17b shows the epitaxial growth of EuS on InAs. The interface between film and substrate is again indicated by white arrows, while the inset shows the Fourier transform of the image. The Fourier transform reveals the presence of the same spots, i.e. InAs and EuS, as found in X8. The high crystalline quality of the EuS layers at the interface is clearly visible in the HTEM scan.

6.5 Summary of the Growth Results

This chapter has dealt with the growth of EuS on InP(001) and InAs(001). The samples were grown at different substrate temperatures, ranging from RT to 400 $°C$. The growth was characterised by AES, SPA-LEED, AFM and TEM. Crystalline order of the grown EuS layers was observed on both substrates. The LEED spots were shown to originate from more than just one surface layer. The same LEED pattern is observed for films with small ($1-2$ nm) and large ($4-20$ nm) EuS film thickness. AES revealed the presence of Eu, S and In (and P in the case on InP) after film deposition. For samples grown on both substrates the substrate elements were no longer visible after the nominal deposition of 4 nm EuS.

Films grown on InP showed increasing surface roughness in form of broadened LEED spots. AFM measurements showed the presence of many small islands with typical widths between $50-100$ nm.

EuS films grown on InAs showed smooth growth and sharp LEED spots even for a film thickness of 20 nm for samples grown at RT. Samples grown at higher substrate temperature also showed smooth growth, while their intensity contribution seemed to originate

from several surface layers. Some samples showed evidence of the formation of structured elongated structures (islands) in the form of cross–like LEED spots.
AFM measurements of samples grown on InAs also show a largely flat surface with individual step heights close to the height of 1–2 atomic layers of EuS(001).
TEM analysis of two 10 nm EuS films deposited on InAs at RT and 300 $°C$ showed the epitaxial growth of EuS as well as the presence of oxidised Eu phases which is due to a lack of S in the EuS layers.

Chapter 7

Conclusion and Outlook

Conclusion

Ferromagnetic semiconductors are considered ideal candidates for application in the field of spintronics, which aims at combining the electron spin and conventional electronics. For this, the creation, detection and manipulation of spin polarised currents is necessary. This thesis has dealt with the material EuS, a semiconducting ferromagnet with a low T_C of 16.5 K in several ways.
Due to its localized, half–filled $4f$ electronic state, it has a high, spin–only magnetic moment of 7 μ_B and is one example of an ideal Heisenberg ferromagnet. Its low Curie temperature makes a direct integration of the material impossible at RT, so ways in order to enhance T_C need to be found. One possible way was found in Co–EuS macroscopic ferrimagnets in the 1990's. The reason for this enhancement effect was given by the magnetic proximity effect between Co and EuS. It was speculated that the same effect should exist between Ni and EuS.

EuS/Co multilayers were analysed by means of x–ray–magnetic–circular–dichroism, polar magneto–optical–Kerr–effect, x–ray–reflectivity measurements and transmission–electron–microscopy. Antiferromagnetic coupling was found in these multilayer at 5 K and even at RT which is attributed to the EuS spin polarisation. This was the first convincing experimental evidence of a EuS T_C enhancement up to RT. The growth of EuS/Co layers shows increasing surface roughness with increasing number of layer repetitions and the presence of defect–induced, unwanted trivalent Eu was found by XAS and TEM. Because of the paramagnetic nature of trivalent Eu, its presence reduced the average magnetic moment per Eu atom in the EuS/Co layers. EuS/Ni layers also showed spin–polarisation in EuS at RT. The induced polarisation was less compared to Co, however, the growth was much smoother as revealed by TEM analysis. Most samples did not show the presence of trivalent Eu, while other showed a small presence. The overall growth qualities of EuS/Ni

multilayers are superior to EuS/Co multilayers.
Further, polar MOKE measurements on similar EuS/Co multilayers were made on a magnetic substrate consisting of Co/Pd multilayers which show inherent perpendicular magnetic anisotropy. In these samples it was possible to observe the antiferromagnetic coupling of EuS and Co at RT and separate both contributions to the Kerr rotation with a simple model. The observation of the EuS Kerr signal was possible because of the known magneto–optical enhancement effect present in EuS/Co layers in the ultraviolet energy range.

First attempts to inject spin–polarised electrons from EuS/Ni and EuS/Co multilayers into spin–LEDs were shown. An initial EuS/Ni multilayer on a spin–LED with a thin AlO_x tunnel barrier showed a very small degree of circular polarisation at 5 K of $P_c < 1\%$. This was explained with the presence of the AlO_x barrier which most likely acted as an additional tunnel barrier after the spin–polarised tunnel barrier of EuS.
A second series of EuS/Co multi– and bilayers were tested on custom–evaporated spin–LED wafers. Most tested sample pieces did not show a clear degree of circular polarisation in the EL measurements at 8 K and at RT.
One sample piece however, showed a clear $P_c \approx 5\%$ at 8 K. The circular polarisation was observed in remanence and with applied magnetic field. A sign reversal of P_c was observed when reversing the external magnetic field, which confirms, that the spin injection was due to the EuS/Co system. The results are the first experimentally observed successful spin injection from EuS/Co layers, which proves the feasibility of spin injection from these systems. The comparably small injection efficiency is attributed to the large amount of surface roughness and defects found in all sample pieces that were measured, as revealed by TEM analysis. First attempts to improve the growth quality of the EuS/Co layers on top of the spin–LED wafers were successful and the amount of roughness and defects were reduced, although not completely.

For the future creation of high quality epitaxial layers of EuS, its growth was studied on InP(001) and InAs(001). AES revealed that films grown on both substrates do not show a substrate signal beyond a EuS film thickness of 4 nm, which suggests a homogeneous coverage. LEED and TEM (for samples deposited on InAs) measurements show a high degree of crystalline order. Overall, the growth on the InP substrate showed the formation of many small islands and generally rough surface. The growth on InAs however, revealed a much smoother growth with large flat terraces, making InAs a better candidate for further studies of EuS growth. This is supported by TEM measurements.

Outlook

During this thesis XMCD measurements have shown the same polarisation effect of EuS in EuS/Ni multilayers as was found earlier in EuS/Co multilayers. The degree of spin–polarisation measured was smaller compared to Co but the growth of EuS/Ni multilayers is superior with less to no trivalent Eu found in the EuS layers. So far, the enhancement effect is only assumed at the interface of EuS and Co/Ni. XRMS measurements can reveal if the magnetisation extends into the interior of the EuS layers or if it is indeed only limited to the interfacial layers. Samples with more layer repetitions have been already produced for these measurements, but beam time was allocated only recently, so that these measurement could not be included in this thesis. Their results however, will contribute to the further understanding of the underlying coupling effect between EuS and Co/Ni.

The results might also contribute to a better model for the observed Kerr rotations in such multilayers at RT. Polar Kerr measurements of Ni/EuS on magnetic substrates at RT and at low temperatures could also provide further insight.

The continuation of EL measurements of EuS/Co(Ni) layers on spin–LED wafers and the creation of smooth EuS/wafer interfaces will most likely increase the achievable injection efficiencies. These measurements could and shoudl be extended to RT, when a better sample quality is ensured.

Finally, the growth study of EuS on InAs has shown very promising results of creating smooth epitaxial layers. These should be analysed *in situ* with STM. Epitaxial EuS layers could show an enhanced coupling to Co and Ni. Measuring the magneto–optic response of such epitaxial layers to check for the presence of ferromagnetism below EuS T_C will also be a next logical step. Eventually, modern photoemission spectroscopy could be done on high quality epitaxial layers of EuS to calculate the exact band structure.

Bibliography

[1] G. E. Moore. Cramming more components onto integrated circuits. *Electronics*, 38(8):114–117, 1965.

[2] S. A. Wolf, D. D. Awschalom, R. A. Buhrman, J. M. Daughton, S. von Molnár, M. L. Roukes, A. Y. Chtchelkanova, and D. M. Treger. Spintronics: A Spin-Based Electronics Vision for the Future. *Science*, 294(5546):1488–1495, 2001.

[3] I. Zutic, J. Fabian, and S. Das Sarma. Spintronics: Fundamentals and applications. *Rev. Mod. Phys.*, 76:323–410, Apr 2004.

[4] Claudia Felser, Gerhard H. Fecher, and Benjamin Balke. Spintronics: A Challenge for Materials Science and Solid-State Chemistry. *Angewandte Chemie International Edition*, 46(5):668–699, 2007.

[5] G Schmidt and L W Molenkamp. Spin injection into semiconductors, physics and experiments. *Semiconductor Science and Technology*, 17(4):310, 2002.

[6] G Schmidt. Concepts for spin injection into semiconductors - a review. *Journal of Physics D: Applied Physics*, 38(7):R107, 2005.

[7] M. Oestreich, M. Bender, J. Hübner, D. Hägele, W. W. Rühle, T. Hartmann, P. J. Klar, W. Heimbrodt, M. Lampalzer, K. Volz, and W. Stolz. Spin injection, spin transport and spin coherence. *Semiconductor Science and Technology*, 17(4):285, 2002.

[8] David D. Awschalom and Michael E. Flatté. Challenges for semiconductor spintronics. *Nature Physics 3*, 3:153–159, 2007.

[9] R. A. de Groot et al. New Class of Materials: Half-Metallic-Ferromagnets. *Physical Review Letters*, 50(25):2024–2027, 1983.

[10] B. T. Matthias, R. M. Bozorth, and J. H. Van Vleck. Ferromagnetic Interaction in EuO. *Phys. Rev. Lett.*, 7:160–161, Sep 1961.

[11] T. R. McGuire, B. E. Argyle, M. W. Shafer, and J. S. Smart. Ferromagnetism in divalent Europium Salts. *Applied Physics Letters*, 1(1):17–18, 1962.

[12] S. Van Houten. Magnetic interaction in EuS, EuSe, and EuTe. *Physics Letters*, 2:215–216, October 1962.

[13] J. S. Moodera, X. Hao, G. A. Gibson, and R. Meservey. Electron-Spin Polarization in Tunnel Junctions in Zero Applied Field with Ferromagnetic EuS Barriers. *Phys. Rev. Lett.*, 61:637–640, Aug 1988.

[14] X. Hao, J. S. Moodera, and R. Meservey. Spin-filter effect of ferromagnetic europium sulfide tunnel barriers. *Phys. Rev. B*, 42:8235–8243, Nov 1990.

[15] P. Wachter. The optical electrical and magnetic properties of the europium chalcogenides and the rare earth pnictides. *C R C Critical Reviews in Solid State Sciences*, 3:189–241, 1972.

[16] P. Wachter. Electronic structure, magnetic exchange and electrical transport properties of the magnetic compounds EuS, GdS and GdP. *Physics Reports*, 44:159–186, 1978.

[17] P. Wachter. Chapter 19 Europium chalcogenides: EuO, EuS, EuSe and EuTe. In *Alloys and Intermetallics*, volume 2 of *Handbook on the Physics and Chemistry of Rare Earths*, pages 507 – 574. Elsevier, 1979.

[18] J. Schoenes. Magnetooptik und elektronische Struktur der magnetisch ordnenden Europiumchalkogenide. *Zeitschrift für Physik*, B 20:345–368, 1975.

[19] J. Schoenes. Exchange and superlattice band splittings in europium chalcogenides; A magneto-optical study in high magnetic fields. *Journal of Magnetism and Magnetic Materials*, 11(1):102 – 108, 1979.

[20] A Mauger and C. Godart. The magnetic, optical and transport properties of representatives of a class of magnetic semiconductors: the europium chalcogenides. *Physics Reports*, 141:51–176, 1986.

[21] S. Demokritov, U. Rücker, and P. Grünberg. Enhancement of the Curie temperature of epitaxial EuS(100) films caused by growth dislocations. *Journal of Magnetism and Magnetic Materials*, 163(1):21 – 26, 1996.

[22] R. Gambino and P. Fumagalli. Magneto-optic Properties of Macroscopic Ferrimagnets. *IEEE Transactions on Magnetics*, 30:4461–4462, 1994.

[23] P. Fumagalli, A. Schirmeisen, and R. J. Gambino. Exchange-induced enhancement of T_C in $Co_{1-x}EuS_x$ macroscopic ferrimagnets. *Phys. Rev. B*, 57:14294–14298, Jun 1998.

[24] C. Müller, H. Lippitz, J.J. Paggel, and P. Fumagalli. Evidence of exchange-induced spin polarization in the magnetic semiconductor EuS. *Journal of Applied Physics*, 95(11):7172–7174, June 2004.

[25] C. Müller, H. Lippitz, J.J. Paggel, and P. Fumagalli. Evidence of exchange-induced spin polarization in the semiconductor EuS at 300K. *Journal of Applied Physics*, 99:073904, 2006.

[26] G. Güntherodt, P. Wachter, and D. M. Imboden. Energy Level Scheme and the Effect of Magnetic Order on the Optical Transitions in Europium Chalcogenides. *Phys. kondens. Materie*, 12:292–310, 1971.

[27] D. E. Eastman, F. Holtzberg, and S. Methfessel. Photoemission studies of the electronic structure of EuO, EuS, EuSe and GdS. *Physical Review Letters*, 23(5):226–229, 1969.

[28] G. Busch, P. Junod, and P. Wachter. Optical absorption of ferro- and antiferromagnetic europium chalcogenides. *Physics Letters*, 12(1):11 – 12, 1964.

[29] T. Kasuya. Exchange Mechanisms in Europium Chalcogenides. *IBM Journal of Research and Development*, 14(3):214–223, May 1970.

[30] J.B. Goodenough. *Magnetism and the Chemical Bond*. Wiley, 1963.

[31] L. Liu. Magnetic interactions in europium compounds. *Solid State Communications*, 46(1):83 – 85, 1983.

[32] Ven-Chung Lee and L. Liu. Indirect exchange interaction in dilute magnetic semiconductors. *Phys. Rev. B*, 29:2125–2130, Feb 1984.

[33] W. Zinn. Microscopic studies of magnetic properties and interactions. Recent results on europium-monochalcogenides. *Journal of Magnetism and Magnetic Materials*, 3:23–36, 1976.

[34] B. Scholz, R. A. Brand, and W. Keune. The spin texture in Fe/Tb multilayers. *Hyperfine Interactions*, 68(1):409–412, 1992.

[35] M. S. S. Brooks, L. Nordström, and B. Johansson. Magnetism of RFe_2 compounds. *Journal of Applied Physics*, 69(8):5683–5684, 1991.

[36] U. Rücker, S. Demokritov, R.R. Arons, and P. Grünberg. Antiferromagnetic interlayer coupling in epitaxial Fe/EuS (100) bilayers. *Journal of Magnetism and Magnetic Materials*, 156(1):269 – 270, 1996.

[37] Jinke Tang, Christine E O'Connor, and Li Feng. Magnetotransport and antiferromagnetic coupling in nanocomposites EuS-Co. *Journal of Alloys and Compounds*, 275-277:606 – 610, 1998.

[38] M. Szot, L. Kowalczyk, K. Gas, V. Domukhovski, W. Knoff, V.V. Volobuev, A.Yu. Sipatov, A.G. Fedorov, and T. Story. Magnetic Properties of EuS/Co Multilayers on KCl and BaF_2 Substrates. *ACTA PHYSICA POLONICA A*, 114(5):1397–1402, 2008.

[39] I. N. Goncharenko and I. Mirebeau. Ferromagnetic Interactions in EuS and EuSe Studied by Neutron Diffraction at Pressures up to 20.5 GPa. *Phys. Rev. Lett.*, 80:1082–1085, Feb 1998.

[40] W. Söllinger, W. Heiss, R. T. Lechner, K. Rumpf, P. Granitzer, H. Krenn, and G. Springholz. Exchange interactions in europium monochalcogenide magnetic semiconductors and their dependence on hydrostatic strain. *Physical Review B*, 81(15), 2010.

[41] Xiangang Wan, Jinming Dong, and Sergej Y. Savrasov. Mechanism of magnetic exchange interactions in europium monochalcogenides. *Phys. Rev. B*, 83:205201, May 2011.

[42] Christian Müller. *Magnetooptische und magnetisch Eigenschaften dünner Co/EuS-Schichtproben*. PhD thesis, Freie Universität Berlin, Institut für Experimentalphysik, 2006.

[43] C. W. Chen and S. Zeitman. Epitaxy in Thin Films of EuS. *Journal of Applied Physics*, 36(2):669–670, 1965.

[44] K. Reichelt and J. Viehweg. Epitaxial growth of high-vacuum evaporated EuS on mica. *Journal of Applied Physics*, 44(9):4242–4242, 1973.

[45] M. Mirabal-Garcia, P. Grünberg, and W. Zinn. Magneto-optical studies of epitaxial EuS films on silicon. *Journal of Magnetism and Magnetic Materials*, 28(3):313 – 318, 1982.

[46] B. Saftic, N. Rasula, W. Zinn, and J. Chevallier. Molecular beam epitaxy and magnetic properties of EuS films on silicon. *Journal of Magnetism and Magnetic Materials*, 28(3):305 – 312, 1982.

[47] W. Zinn, B. Saftic, N. Rasula, M. Mirabal, and J. Köhne. EuS ferromagnetic semiconductor films grown epitaxially on silicon. *Journal of Magnetism and Magnetic Materials*, 35:329–336, 1983.

[48] C. J. P. Smits, A. T. Filip, J. T. Kohlhepp, H. J. M. Swagten, B. Koopmans, and W. J. M. de Jonge. Magnetic and structural properties of EuS for magnetic tunnel junction barriers. *Journal of Applied Physics*, 95(11):7405–7407, 2004.

[49] Shinya Senba, Naoki Matsumoto, Mitsuhiro Jomura, Hironori Asada, Tsuyoshi Koyanagi, Kengo Kishimoto, and Yasuhiro Fukuma. Characterization of epitaxial EuS(111) thin films on $BaF_2(111)$ and $SrF_2(111)$ substrates grown by molecular beam epitaxy. *Journal of the Korean Physical Society*, 62(12):2109–2112, 2013.

[50] H. Lüth. *Solid Surfaces, Interfaces and Thin Films.* Springer Verlag, 2001.

[51] AG Hillebrands (https://www.physik.uni-kl.de/hillebrands/research/methods/molecular-beam-epitaxy/; last accessed 21.06.2017).

[52] Jan H. van der Merwe and E. Bauer. Influence of misfit and bonding on the mode of growth in epitaxy. *Phys. Rev. B*, 39:3632–3641, Feb 1989.

[53] Giriraj Jnawali. *Growth, Morphology, and Conductivity in Semimetallic/Metallic Films on Si(001).* PhD thesis, Universität Duisburg-Essen, 2009.

[54] Holger Lippitz. *Wachstumsverhalten von dünnen Manganschichten auf Si(100)- und Bismut terminierten Si(100)-Oberflächen.* PhD thesis, Freie Universität Berlin, 2005.

[55] James W. Mayer Leonard C. Feldman. *Fundamentals of surface and thin film analysis.* North Holland, 1986.

[56] Lawrence E. Davis, Noel C. MacDonald, Paul W. Palmberg, Gerald E. Riach and Roland F. Weber. *Handbook of Auger Electron Spectroscopy.* Physical Electronics Industries, Inc., 1976.

[57] Yokoyama Toshihiko, Takeshi Nakagawa, and Yasumasa Takagi. Magnetic circular dichroism for surface and thin film magnetism: Measurement techniques and surface chemical applications. *International Reviews in Physical Chemistry*, 27(3):449–505, 2008.

[58] Gunnar Sommer. Aufbau eines Kerr-Spektrometers und Messungen an magnetisch verdünnten Halbleitern. Master's thesis, Freie Universität Berlin, 2000.

[59] Paul Fumagalli, C. Spaeth, Ulrich Rudiger, and R.J. Gambino. A new magneto-optic enhancement effect in macroscopic ferrimagnets. *IEEE Transactions on Magnetics*, 31(6):3319–3324, 1995.

[60] G Schütz, W Wagner, W Wilhelm, P Kienle, R Zeller, R Frahm, and G Materlik. Absorption of Circularly Polarized X–Rays in Iron . *Physical Review Letters*, 58(7):737–740, FEB 16 1987.

[61] Heiko Wende. Recent advances in x-ray absorption spectroscopy. *Reports on Progress in Physics*, 67:2105–2181, 2004.

[62] J. Stöhr. X-ray magnetic circular dichroism spectroscopy of transition metal thin films. *Journal of Electron Spectroscopy and Related Phenomena*, 75(0):253 – 272, 1995.

[63] J. Stöhr. Exploring the microscopic origin of magnetic anisotropies with X-ray magnetic circular dichroism (XMCD) spectroscopy. *Journal of Magnetism and Magnetic Materials*, 200:470–497, 1999.

[64] B. T. Thole, P. Carra, F. Sette, and G. van der Laan. X-ray circular dichroism as a probe of orbital magnetization. *Phys. Rev. Lett.*, 68:1943–1946, Mar 1992.

[65] B. T. Thole and G. van der Laan. Sum rules for magnetic dichroism in rare earth 4 f photoemission. *Phys. Rev. Lett.*, 70:2499–2502, Apr 1993.

[66] Björn Lewitz. Aufbau und Inbetriebnahme eines polaren Kerr-Spektrometers zur Messung im Ultrahochvakuum. Master's thesis, Freie Universität Berlin, 2007.

[67] Michael Scott. Introducing perpendicular anisotropy in EuS multilayers. Master's thesis, Freie Universität Berlin, 2015.

[68] Arne Grothenrath. Polar MOKE investigation of thin Co/EuS and Ni/EuS multilayers. Master's thesis, Freie Universität Berlin, 2017.

[69] C. Müller, H. Lippitz, J. J. Paggel, and P. Fumagalli. Magneto-optic properties of thin EuS/Co and EuS/Cu films on Si(111) substrates. *Journal of Applied Physics*, 91(10):7535–7537, 2002.

[70] B. Lewitz, A. Straub, V. Kapaklis, P. Poulopoulos, A. Delimitis, S. D. Pappas, and P. Fumagalli. Proximity Effects And Curie Temperature Enhancement In Co/EuS And Fe/EuS Multilayers. *SPIN*, 02(04):1250016, 2012.

[71] S.D. Pappas, P. Poulopoulos, B. Lewitz, A. Straub, A. Goschew, V. Kapaklis, F. Wilhelm, A. Rogalev, and P. Fumagalli. Direct evidence for significant spin-polarization of EuS in Co/EuS multilayers at room temperature. *Scientific Reports*, 2013.

[72] H. Kiessig. Untersuchungen zur Totalreflexion von Röntgenstrahlen. *Annalen der Physik*, 402:715–768, 1931.

[73] B. J. Ruck, H. J. Trodahl, J. H. Richter, J. C. Cezar, F. Wilhelm, A. Rogalev, V. N. Antonov, Binh Do Le, and C. Meyer. Magnetic state of EuN: X-ray magnetic circular dichroism at the Eu $M_{4,5}$ and $L_{2,3}$ absorption edges. *Phys. Rev. B*, 83:174404, May 2011.

[74] V. N. Antonov, B. N. Harmon, and A. N. Yaresko. Electronic structure of mixed-valence and charge-ordered Sm and Eu pnictides and chalcogenides. *Phys. Rev. B*, 72:085119, Aug 2005.

[75] J. Röhler and G. Kaindl. Influence of pressure on the inhomogeneous mixed-valent state of Eu_3S_4. *Solid State Communications*, 36:1055–1057, 1980.

[76] Coenrardus Johannes Petrus Smits. *EuS based thin film layered systems*. PhD thesis, Eindhoven University of Technology, 2006.

[77] H.J.G. Draaisma, W.J.M. de Jonge, and F.J.A. den Broeder. Magnetic interface anisotropy in Pd/Co and Pd/Fe multilayers. *Journal of Magnetism and Magnetic Materials*, 66(3):351 – 355, 1987.

[78] H. J. G. Draaisma and W. J. M. de Jonge. Magnetization curves of Pd/Co multilayers with perpendicular anisotropy. *Journal of Applied Physics*, 62(8):3318–3322, 1987.

[79] P. F. Carcia. Perpendicular magnetic anisotropy in Pd/Co and Pt/Co thin film layered structures. *Journal of Applied Physics*, 63(10):5066–5073, 1988.

[80] Craig Dennis England. *Properties of Cobalt/Copper and Cobalt/Palladium Multilayers*. PhD thesis, University of Arizona, 1991.

[81] Panagiotis Poulopoulos, Björn Lewitz, Andreas Straub, Spiridon D. Pappas, Sotirios A. Droulias, Sotirios Baskoutas, and Paul Fumagalli. Band-gap tuning at the strong quantum confinement regime in magnetic semiconductor EuS thin films. *Applied Physics Letters*, 100(21):211910, 2012.

[82] J. L. Erskine and E. A. Stern. Magneto-optic Kerr Effect in Ni, Co, and Fe. *Phys. Rev. Lett.*, 30:1329–1332, Jun 1973.

[83] Charles Kittel. *Introduction to Solid State Physics*. John Wiley & Sons, 6th edition, 1986.

[84] V. V. Volobuev, A. N. Stetsenko, and J. van Lierop. Film thickness dependence of the enhanced EuS interface ordering temperature in EuS/Co thin films. *Journal of Applied Physics*, 103(7):07C905, 2008.

[85] P. Poulopoulos, M. Angelakeris, E. Th. Papaioannou, N. K. Flevaris, D. Niarchos, M. Nyvlt, V. Prosser, S. Visnovsky, Ch. Mueller, P. Fumagalli, F. Wilhelm, and A. Rogalev. Structural, magnetic, and spectroscopic magneto-optical properties aspects of Pt-Co multilayers with intentionally alloyed layers. *Journal of Applied Physics*, 94(12):7662–7669, 2003.

[86] L. Vitos, A.V. Ruban, H.L. Skriver, and J. Kollár. The surface energy of metals. *Surface Science*, 411(1-2):186 – 202, 1998.

[87] P. Poulopoulos, R. Krishnan, and N.K. Flevaris. Antiferromagnetic-like coupling evidence in a Pd-Ni multilayer with inverted hysteresis features. *Journal of Magnetism and Magnetic Materials*, 163(1-2):27 – 31, 1996.

[88] N. Nishizawa and H. Munekata. Efficient spin injection through a crystalline AlOx tunnel barrier prepared by the oxidation of an ultra-thin Al epitaxial layer on GaAs. *Journal of Applied Physics*, 114(3):033507, 2013.

[89] N. Nishizawa, K. Nishibayashi, and H. Munekata. A spin light emitting diode incorporating ability of electrical helicity switching. *Applied Physics Letters*, 104(11):111102, 2014.

[90] Peter Y. Yu and Manuel Cardona. *Fundamentals of Semiconductors: Physics and Materials Properties*. Springer Verlag, 2010.

[91] M. I. Dyakonov and V. I. Perel. *Theory of Optical Spin Orientation ofElectrons and Nuclei in Semiconductors*, chapter 2, pages 11–71. Elsevier Science Publishers, 1984.

[92] A.M. Vasilev, F. Daiminger, J. Straka, A. Forchel, V.P. Kochereshko, G.L. Sandler, and I.N. Uraltsev. Optical orientation of holes and electrons in strained layer InGaAs/GaAs quantum wells. *Superlattices and Microstructures*, 13(1):97 – 100, 1993.

[93] B. D. Oskotskij, A. V. Subashiev, and Y. A. Mamaev. Polarized photoemission spectra of the strained semiconductor layers. *Phys. Low-Dimens. Semicond. Struct.*, 1(2):77–87, 1997.

[94] Supriyo Datta and Biswajit Das. Electronic analog of the electro-optic modulator. *Applied Physics Letters*, 56(7):665–667, 1990.

[95] W. Y. Lee, S. Gardelis, B. C. Choi, Y. B. Xu, C. G. Smith, C. H. W. Barnes, D. A. Ritchie, E. H. Linfield, and J. A. C. Bland. Magnetization reversal and magnetoresistance in a lateral spin-injection device. *Journal of Applied Physics*, 85(9):6682–6685, 1999.

[96] P. R. Hammar, B. R. Bennett, M. J. Yang, and Mark Johnson. Observation of Spin Injection at a Ferromagnet Semiconductor Interface. *Phys. Rev. Lett.*, 83:203–206, Jul 1999.

[97] G. Schmidt, D. Ferrand, L. W. Molenkamp, A. T. Filip, and B. J. van Wees. Fundamental obstacle for electrical spin injection from a ferromagnetic metal into a diffusive semiconductor. *Phys. Rev. B*, 62:R4790–R4793, Aug 2000.

[98] M. Oestreich, J. Hübner, D. Hägele, P. J. Klar, W. Heimbrodt, W. W. Rühle, D. E. Ashenford, and B. Lunn. Spin injection into semiconductors. *Applied Physics Letters*, 74(9):1251–1253, 1999.

[99] Y. Ohno, D. K. Young, B. Beschoten, F. Matsukura, H. Ohno, and D. D. Awschalom. Electrical spin injection in a ferromagnetic semiconductor heterostructure. *Nature*, 402:790–792, 1999.

[100] R. Fiederling, M. Keim, G. Reuscher, W. Ossau, G. Schmidt, A. Waag, and L. W. Molenkamp. Injection and detection of a spin-polarized current in a light-emitting diode. *Nature*, 402:787–790, 1999.

[101] B. T. Jonker, Y. D. Park, B. R. Bennett, H. D. Cheong, G. Kioseoglou, and A. Petrou. Robust electrical spin injection into a semiconductor heterostructure. *Phys. Rev. B*, 62:8180–8183, Sep 2000.

[102] E. I. Rashba. Theory of electrical spin injection: Tunnel contacts as a solution of the conductivity mismatch problem. *Physical Review B*, 62(24):267–270, 2000.

[103] A. Fert and H. Jaffres. Conditions for efficient spin injection from a ferromagnetic metal into a semiconductor. *Phys. Rev. B*, 64:184420, Oct 2001.

[104] J. D. Albrecht and D. L. Smith. Electron spin injection at a Schottky contact. *Phys. Rev. B*, 66:113303, Sep 2002.

[105] C. H. Li, G. Kioseoglou, O. M. J. van t Erve, A. T. Hanbicki, B. T. Jonker, R. Mallory, M. Yasar, and A. Petrou. Spin injection across (110) interfaces: Fe/GaAs(110) spin-light-emitting diodes. *Applied Physics Letters*, 85(9):1544–1546, 2004.

[106] O. M. J. van t Erve, G. Kioseoglou, A. T. Hanbicki, C. H. Li, B. T. Jonker, R. Mallory, M. Yasar, and A. Petrou. Comparison of Fe Schottky and Fe Al_2O_3 tunnel barrier contacts for electrical spin injection into GaAs. *Applied Physics Letters*, 84(21):4334–4336, 2004.

[107] V. F. Motsnyi, P. Van Dorpe, W. Van Roy, E. Goovaerts, V. I. Safarov, G. Borghs, and J. De Boeck. Optical investigation of electrical spin injection into semiconductors. *Phys. Rev. B*, 68:245319, Dec 2003.

[108] R. Benabderrahmane, M. Kanoun, N. Bruyant, C. Baraduc, A. Bsiesy, and H. Achard. Al_2O_3 tunnel barrier as a good candidate for spin injection into silicon. *Solid-State Electronics*, 54(8):741 – 744, 2010.

[109] X. Jiang, R. Wang, R. M. Shelby, R. M. Macfarlane, S. R. Bank, J. S. Harris, and S. S. P. Parkin. Highly Spin-Polarized Room-Temperature Tunnel Injector for Semiconductor Spintronics using MgO(100). *Phys. Rev. Lett.*, 94:056601, Feb 2005.

[110] Tomoyuki Sasaki, Tohru Oikawa, Toshio Suzuki, Masashi Shiraishi, Yoshishige Suzuki, and Katsumichi Tagami. Electrical Spin Injection into Silicon Using MgO Tunnel Barrier. *Applied Physics Express*, 2(5):053003, 2009.

[111] R. Fiederling, P. Grabs, W. Ossau, G. Schmidt, and L. W. Molenkamp. Detection of electrical spin injection by light-emitting diodes in top- and side-emission configurations. *Applied Physics Letters*, 82(13):2160–2162, 2003.

[112] O. M. J. van t Erve, G. Kioseoglou, A. T. Hanbicki, C. H. Li, and B. T. Jonker. Remanent electrical spin injection from Fe into AlGaAs/GaAs light emitting diodes. *Applied Physics Letters*, 89(7):072505, 2006.

[113] Ahmad Bsiesy. Spin injection into semiconductors: towards a semiconductor-based spintronic device. *Comptes Rendus Physique*, 6(9):1022 – 1026, 2005. SpintronicssSpintronique.

[114] M Holub and P Bhattacharya. Spin-polarized light-emitting diodes and lasers. *Journal of Physics D: Applied Physics*, 40(11):R179, 2007.

[115] John G. Simmons. Generalized Formula for the Electric Tunnel Effect between Similar Electrodes Separated by a Thin Insulating Film. *Journal of Applied Physics*, 34(6):1793–1803, 1963.

[116] K. Knorr, M. Pristovsek, U. Resch-Esser, N. Esser, M. Zorn, and W. Richter. In situ surface passivation of III-V semiconductors in MOVPE by amorphous As and P layers. *Journal of Crystal Growth*, 170(1):230 – 236, 1997.

[117] S. Farhad Masoudi and Zhaleh Ebrahiminejad. Effects of interface structure on spin filter tunnel junctions. *Surface Science*, 630:85 – 88, 2014.

[118] Joël Griesmar. Growth characterization of EuS on InAs and InP. Master's thesis, Freie Universität Berlin, 2015.

[119] A.G Milnes and A.Y Polyakov. Indium arsenide: a semiconductor for high speed and electro-optical devices. *Materials Science and Engineering: B*, 18(3):237 – 259, 1993.

[120] Karolina Szamota-Leandersson. *Electronic structure of clean and adsorbate-covered InAs surfaces*. PhD thesis, KTH, 2010.

[121] P. Streubel, R. Hesse, L. Makhova, J. Schindelka, and R. Denecke. A Practicable Method for Thickness Estimation of Ultrathin Layers from XPS Data with UNIFIT 2011. Technical report, Wilhelm-Ostwald-Institut für Physikalische und Theoretische Chemie, Universität Leipzig, 2011.

[122] W. S. Yang, F. Jona, and P. M. Marcus. Atomic structure of Si(001) 2x1. *Phys. Rev. B*, 28:2049–2059, Aug 1983.

[123] S. Heun, J. Falta, and M. Henzler. The initial stages of epitaxial growth of silicon on Si(100) 2x1. *Surface Science*, 243:132–140, February 1991.

[124] A. Goschew, J. Griesmar, and P. Fumagalli. Epitaxial growth of EuS on InAs(100) and InP(100). *Thin Solid Films*, 625:106 – 110, 2017.

[125] A. Goschew, M. Scott, and P. Fumagalli. Verification of antiferromagnetic exchange coupling at room temperature using polar magneto-optic Kerr effect in thin EuS/Co multilayers with perpendicular magnetic anisotropy. *Applied Physics Letters*, 109(6):062401, 2016.

[126] P. Poulopoulos, A. Goschew, V. Kapaklis, M. Wolff, A. Delimitis, F. Wilhelm, A. Rogalev, S. D. Pappas, A. Straub, and P. Fumagalli. Induced spin-polarization of EuS at room temperature in Ni/EuS multilayers. *Applied Physics Letters*, 104(11):112411, 2014.

Appendix

Publications and Conferences

Publications

A. Goschew, J. Griesmar, and P. Fumagalli. Epitaxial growth of EuS on InAs(100) and InP(100). *Thin Solid Films*, 625:106 – 110, 2017

A. Goschew, M. Scott, and P. Fumagalli. Verification of antiferromagnetic exchange coupling at room temperature using polar magneto-optic Kerr effect in thin EuS/Co multilayers with perpendicular magnetic anisotropy. *Applied Physics Letters*, 109(6):062401, 2016

P. Poulopoulos, A. Goschew, V. Kapaklis, M. Wolff, A. Delimitis, F. Wilhelm, A. Rogalev, S. D. Pappas, A. Straub, and P. Fumagalli. Induced spin-polarization of EuS at room temperature in Ni/EuS multilayers. *Applied Physics Letters*, 104(11):112411, 2014

S.D. Pappas, P. Poulopoulos, B. Lewitz, A. Straub, A. Goschew, V. Kapaklis, F. Wilhelm, A. Rogalev, and P. Fumagalli. Direct evidence for significant spin-polarization of EuS in Co/EuS multilayers at room temperature. *Scientific Reports*, 2013

Conferences

A. Goschew and P. Fumagalli. *Antiferromagnetic Exchange–Coupling in EuS multilayers at Low and at Room Temperature investigated by XMCD and polar MOKE*, 5th International Conference from Nanoparticles and Nanomaterials to Nanodevices and Nanosystems, Porto Heli, Greece (2016), talk

A. Goschew, P. Poulopoulos, V. Kapaklis, F. Wilhelm, A. Rogalev and P. Fumagalli. *Room temperature spin-polarization of EuS by thin ferromagnetic multilayers*, Intermag, Beijing, China (2015), talk

A. Goschew, P. Poulopoulos, V. Kapaklis, F. Wilhelm, A. Rogalev and P. Fumagalli. *Curie temperature enhancement of EuS by thin ferromagnetic metal multilayers - a possible material for spintronics*, E.S.R.F. User Microsymposium, Grenoble, France (2015), talk

Zusammenfassung

Das Forschungsgebiet der Spintronik wird in der aktuellen Wissenschaft eingehend untersucht. Das Ziel der Spintronik ist dabei unter anderem die Erzeugung von spinpolarisierten elektrischen Strömen und deren erfolgreiche Injektion in Halbleiter.
Verschiedene Materialien werden aktuell bezüglich ihrer Nutzbarkeit für Spininjektion untersucht, unter anderem magnetische Halbleiter. Das Material Europiumsulfid (EuS) ist ein solcher magnetischer Halbleiter, welcher unterhalb seines T_C von 16.5 K ein hohes magnetisches Moment von 7 μ_B aufweist.
In dieser Arbeit wird EuS in EuS/Co und EuS/Ni Multischichten untersucht. Dabei wird das Wachstum der Multischichten mittels Röntgenbeugung (XRR) und Transmissionselektronenmikroskopie (TEM) untersucht. Die magnetischen Eigenschaften werden mittels zirkularem Röntgendichroismus (XMCD) und polarem magnetooptischen Kerr Effekt (pMOKE) untersucht.
Die XMCD Messungen zeigen eine antiferromagnetische Kopplung zwischen EuS und Co (Ni) bei 5 K sowie bei Raumtemperatur. Diese antiferromagnetische Kopplung wird auf eine magnetische Ordnung innerhalb des EuS zurückgeführt. Dies entspricht einer starken T_C Erhöhung von EuS und wird auf einen Polarisationseffekt durch Co und Ni in den Multischichten erklärt. Der Polarisationseffekt ist dabei stärker in den Multischichten mit Co. Allerdings weisen diese auch die Präsenz von trivalentem Eu auf, welches aufgrund seines Paramagnetismus unerwünscht ist. Multischichten von EuS/Ni zeigen eine deutliche Reduktion von trivalentem Eu, was auf das bessere Wachstum zwischen EuS und Ni zurückgeführt wird.
Die antiferromagnetische Kopplung kann ebenfalls durch pMOKE Messungen bei Raumtemperatur nachgewiesen werden.
Wachstumsstudien von EuS auf den Substraten InP und InAs werden mittels Auger Elektronenspektroskopie (AES), niederenergetischer Elektronenbeugung (LEED) und TEM durchgeführt. EuS wächst epitaktisch auf beiden Substraten, wobei die Schichten auf InAs eine höhere Qualität aufweisen.
Erste Spininjektionsmessungen des Systems EuS/Co auf Spin–LEDs zeigen eine erfolgreiche Spininjektion bei 8 K, wobei das emittierte Licht einen Polarisationsgrad von ca. 5% aufweist. Diese Messungen stellen die ersten ihrer Art dar und zeigen die prinzipielle Eignung des System EuS/Co zur Spininjektion.

Abstract

The field of spintronics is in the focus of current research. One of the aims of spintronics is the generation of spin–polarised currents and their successful injection into semiconductors.
Different materials are currently investigated regarding their feasibility for spintronics, among them ferromagnetic semiconductors. Europium sulfide (EuS) is such a ferromagnetic semiconductor with a large magnetic moment of 7 μ_B below its T_C of 16.5 K.
EuS is investigated in EuS/Co and EuS/Ni multilayers in this thesis. The multilayer growth is studied by x–ray–reflectivity (XRR) and transmission electron microscopy (TEM). The magnetic properties are investigated using x–ray magnetic circular dichroism (XMCD) and polar magneto–optical Kerr effect (pMOKE).
XMCD measurements show an antiferromagnetic coupling between EuS and Co (Ni) at 5 K and at room temperature. The antiferromagnetic coupling is attributed to ferromagnetic ordering within the EuS layers. This corresponds to a large T_C enhancement of EuS and is attributed to a polarisation effect of Co and Ni in the multilayers. The polarisation effect is stronger in EuS/Co multilayers. However, trivalent Eu is also found in EuS/Co multilayers, which is unwanted due to its paramagnetism. EuS/Ni multilayers show a largely decreased amount of trivalent Eu, which is attributed to better growth between EuS and Ni.
The antiferromagnetic coupling is also resolved by pMOKE at room temperature.
The growth of EuS on InP and InAs is studie by Auger electron spectroscopy (AES), low energy electron diffraction (LEED) and TEM. EuS grows epitaxially on both substrates. Layers grown on InAs show a higher quality.
First spin–injection measurements of the EuS/Co system on a spin–LED show successful spin–injection. At 8 K a degree of circular polarisation of about 5% is achieved. These measurements are the first of their kind and show the feasibility of spin–injection from the system EuS/Co.

Danksagung

An dieser Stelle möchte ich mich bei all den Menschen bedanken, die mich im Verlauf meines Lebens und insbesondere während der letzten vier Jahre unterstützt haben.

Zunächst möchte ich mich bei *Prof. Dr. Paul Fumagalli* bedanken. Er hat mir nicht nur die Möglichkeit gegeben, meine Arbeit in seiner Arbeitsgruppe zu schreiben, sondern war auch jederzeit bereit, mir mit Rat und Tat zur Seite zu stehen, wenn Probleme oder Fragen aufkamen.

Ich bedanke mich weiterhin bei *Prof. Dr. Wolfgang Kuch* für die Bereitschaft zur Übernahme des Zweitgutachtens.

Ich möchte mich bei allen aktuellen und ehemaligen Gruppenmitgliedern bedanken, die ich kennenlernen durfte und durch die eine stets angenehme Arbeitsatmosphäre in der Gruppe war. Zu nennen sind hier insbesondere *Björn Lewitz, Min Song, Dr. Mohamed Haggui, Joël Griesmar, Michael Scott und Arne Grotenrath.*

Hans Badow möchte ich für die kleineren und größeren Reparaturen an der MBE und der Balzers danken. *Marion Badow* möchte ich für ihre stete Hilfsbereitschaft und ihre freundliche Art danken.

Vielen Dank an *Prof. Dr. Panagiotis Poulopoulos*, den ich lange Zeit nicht gesehen habe und der trotzdem jederzeit hilfsbereit war und verschiedene Fragen beantworten konnte.

Ein großer Dank gebührt selbstverständlich meinen beiden Eltern, die mich stets bei all meinen Bemühungen unterstützt haben und immer für mich da waren.

Am Ende möchte ich zwei sehr wichtige Menschen erwähnen, die stets an meiner Seite waren: *Patrick Andrä* und meine Freundin *Lina*. Danke Patrick für all die witzigen Diskussionen während unserer gemeinsamen Zeit in der Gruppe und unsere Freundschaft, die mir viel bedeutet.
Danke Lina dafür, dass es dich gibt und du mein Leben unvorstellbar bereicherst.

Curriculum Vitae

The Curriculum Vitae is omitted in the online version, due to data privacy.

Selbständigkeitserklärung

Hiermit versichere ich, dass die vorliegende Dissertation mit dem Titel „Magneto–optical investigations of EuS/Co and EuS/Ni multilayers for spintronic applications“ selbständig und ohne unerlaubte Hilfe angefertigt wurde. Beim Verfassen der Arbeit wurden keine anderen als die im Text aufgeführten Hilfsmittel verwendet. Ein Promotionsverfahren an einer anderen Hochschule oder an einem anderen Fachbereich zu einem früheren Zeitpunkt wurde nicht beantragt.

Alexander Goschew, Berlin, 21.06.2017